VASCULAR STENT ANALYSIS

by

TRÉ RAYMOND WELCH

Presented to the Faculty of the Graduate School of

The University of Texas at Arlington in Partial Fulfillment

of the Requirements

for the Degree of

MASTER OF SCIENCE IN BIOMEDICAL ENGINEERING

THE UNIVERSITY OF TEXAS AT ARLINGTON

August 2005

ACKNOWLEDGEMENTS

I would like to thank Dr. Charles Chuong for his guidance and patience working with me on the stent analysis project. I am also grateful for being given the opportunity to work on an interesting project with vascular stents. This project has been a wonderful experience incorporating the various design phases in the engineering process.

I would also like to thank my committee Dr. Robert Eberhart and Dr. Panos Shiakolas for their suggestions and recommendations for the data interpretation of the testing and simulation results with ANSYS. Also, I thank Dr. Eberhart's research group for providing the stents and equipment needed for the verification testing.

I appreciate the work and efforts of Jacob Abraham for his aid in capturing pictures for the verification testing. Finally, I would like to thank my parents, sister and friends for their support and encouragement in pursuing this degree.

August 1, 2005

ABSTRACT

VASCULAR STENT ANALYSIS

Publication No. _____

Tré Raymond Welch, MS (BME)

The University of Texas at Arlington, 2005

Supervising Professor: CJ Chuong

It is important for cardiologist to understand the stresses and strains the stent experiences during deployment.

We created a 3-D model of the coiled stent which is exported into ANSYS creating the finite element model. The stent material is Poly-L-Lactic Acid (PLLA) fiber with a Young's modulus of 7043(MPa) and a Poisson's ratio of 0.35. A nonlinear material analysis simulates the material behavior through plastic deformation during expansion from 1(atm) to 14(atm).

The von Mises stresses, principal stresses, and principal strains are analyzed to determine the yielding of the PLLA fiber. Also, the effect of different material properties including Young's modulus, yield stress, yield strain is examined for the baseline case and three additional cases with Young's modulus of 4701, 3189, and

2266(MPa). The axial displacement values are increased to see any effect on the maximum shear stresses.

Finally, verification testing is performed to compare the experimental results to the simulation results.

TABLE OF CONTENTS

LIST OF ILLUSTRATIONS

LIST OF TABLES

CHAPTER 1

INTRODUCTION

1.1 Background

Stents have many applications in the medical device industry, being used as renal stents, stent grafts, carotid stents, and high pressure balloon expandable stents. Vascular stents have been used to restore arterial blood flow in patients suffering from atherosclerosis for the past 20 years.

Atherosclerosis is a build up of plaque in the coronary arteries resulting in a thickening and hardening of the arteries. The accumulation of plaque in the arteries occurs over the lifetime of an individual. This accumulation is usually due to the health state of the individual. Fox (2003) discusses cigarette smoke, high blood pressure, elevated cholesterol and triglycerides attribute to the loss of blood flow to tissue by damaging the arterial walls and result in plaque burden impeding blood flow as shown in Fig. 1.1.

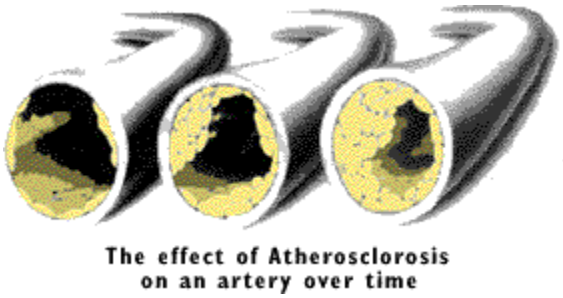

Fig. 1.1 Plaque Accumulation in the Artery
(Source: http:// www.thehealthpages.com/)

Plaque can partially or totally block blood flow through the artery causing hemorrhaging and thrombus on the plaque surface. Restoring blood flow to the coronary arteries is performed by angioplasty, coronary artery bypass surgery, or vascular stent deployment.

A vascular stent is a surgical device placed inside a blocked artery causing the artery to open and restore blood flow. These devices are usually cylindrical most commonly composed of stainless steel (Ratner, Hoffman, Schoen, Lemons, 2004). The stent is placed over a deflated balloon on the tip of a catheter. The catheter is a thin tube introduced through the femoral artery at the groin and pushed to the lesion site. By inflating the balloon up to 10-14(atm), the stent expands and opens the artery for blood flow. After the balloon deflates, the stent remains in its expanded shape in the blocked area as shown in Fig 1.2.

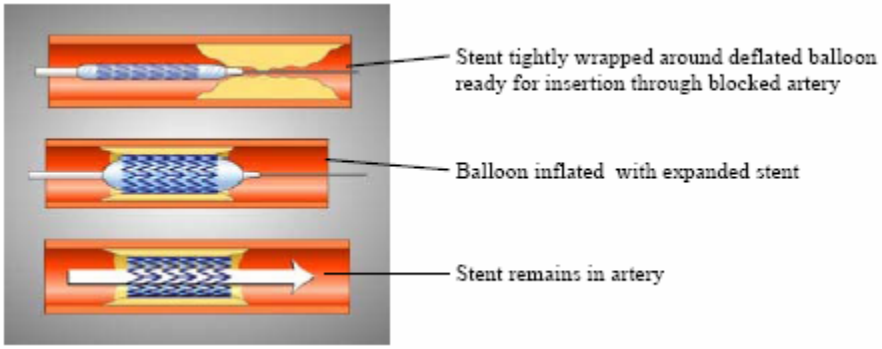

Fig. 1.2 Expansion steps for stent deployment (Source: Warkentim, 2005)

Stents are usually of a metal material in cylindrical shape. Grooves are cut into the metal to allow the stent to expand and take the cylindrical shape of the balloon. After deflation, the stent interacts with the arterial vessel and elastic recoil occurs with the stent and artery due to the overstretching of the balloon (Bennett et al., 2001). The

contact of the struts with the arterial vessel can lead to arterial wall injury. Sullivan (2002) discusses the struts fracturing the internal elastic lamina resulting in deep arterial wall injury. The arterial wall injury leads to remodeling of the vascular wall, restenosis, cell proliferation, and intense inflammation which can lead to a sudden rupture to the "vulnerable" lesions causing acute coronary syndromes (Tuzcu and Schoenhagen, 2003).

The mechanical stress applied to the stent from the balloon forces the arterial wall into an open position by increasing the stresses in the material of the stent to surpass its yield strength and deform into the plastic region. After deflation of the balloon, different properties of the stent are calculated including distal radial recoil, central radial recoil, longitudinal recoil, foreshortening and dogboning (Migliavacca et al., 2005). These properties describe the structural performance of the stent in the axial direction and the radial direction. They aid in the understanding of the stent's expansion and lengthening in the deployment process.

Finite element analysis is a cost effective way to analyze models without the expense of testing the stents for different design parameters. It has been used to evaluate the stress, strain, deformation, boundary conditions and loading conditions of the stent.

1.2 Literature Review

1.2.1 Human Artery Cross-Section

The human artery is composed of three basic sizes: small, medium, and large. The medium and large arteries are composed of a tunica interna, tunica media, and tunica externa. The tunica interna interacts with the blood flow. This layer is composed of endothelium and elastic fibers whereas the tunica media contains largely smooth muscle cells as shown in Fig 1.3. When fats and cholesterol deposit in the internal layer of the artery, the diameter of the artery closes as shown in Fig. 1.4. This build up of plaque and fats is known as atherosclerosis.

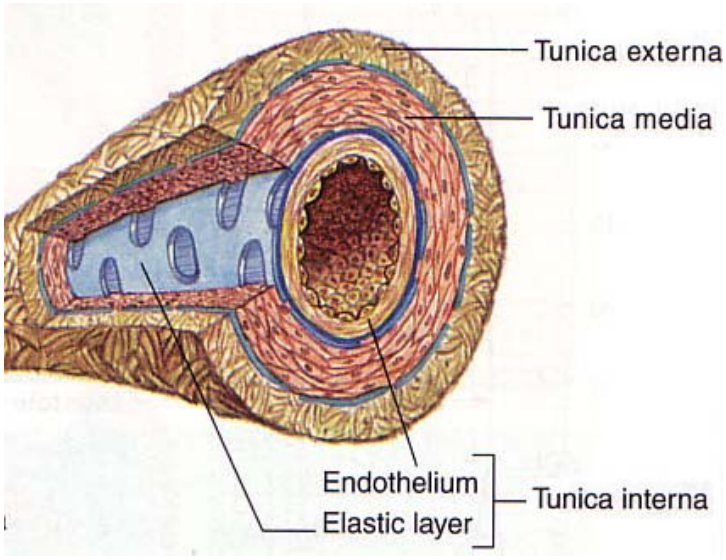

Fig. 1.3 Artery Layers (Source: Human Physiology, 7th Edition)

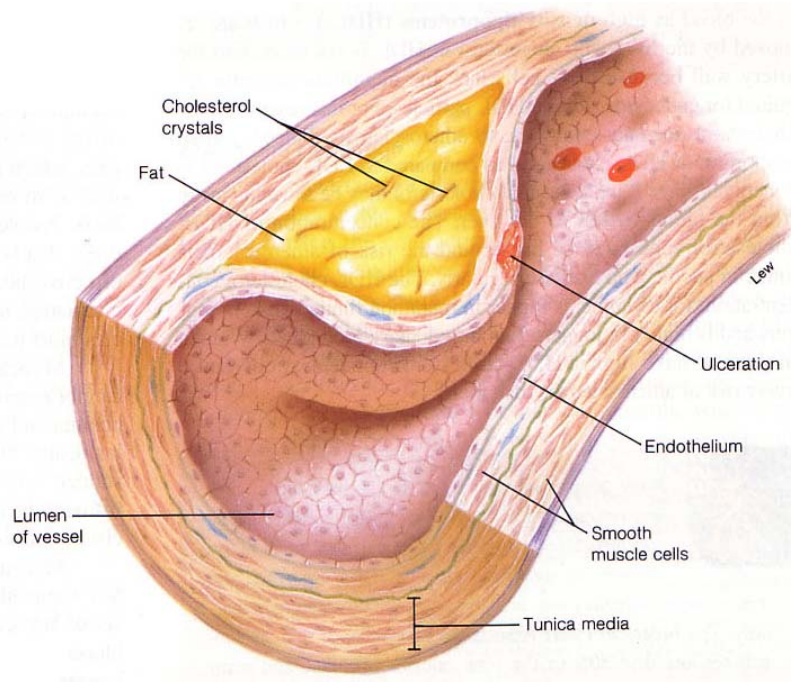

Fig. 1.4 Atherosclerosis (Source: Human Physiology, 7th Edition)

1.2.2 Balloon Expandable Stent Designs

The slotted design and the coil design are the most commonly used stents as shown in Fig. 1.5. Historically, the coil stent design shows higher restenosis rates than the slotted tube designs (Osterle et al., 1998).

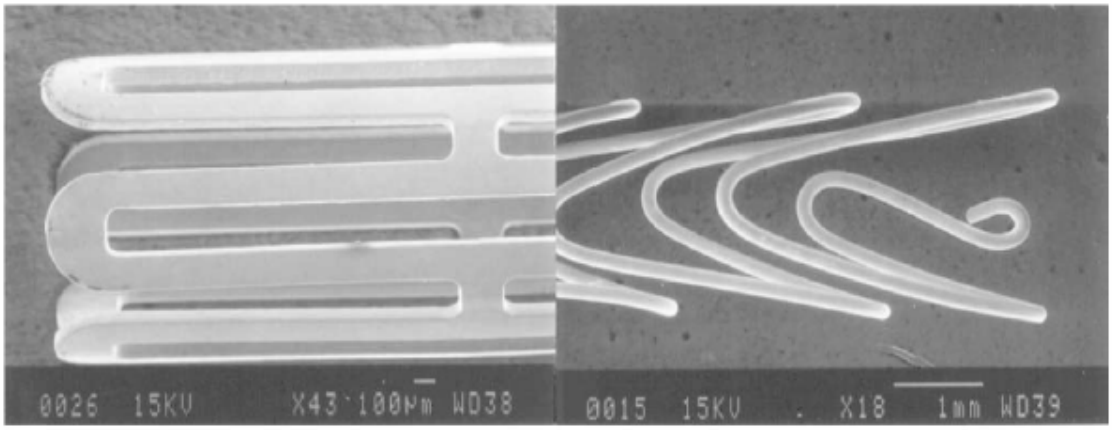

Fig. 1.5 Scanning Electron Micrograph of Palmaz-SchatzTM Stent and Freedom® Coil Stent (Source: Etave et al., 2001)

Both stent designs have advantages and disadvantages. The advantages of the coil stent are the flexibility of the stent to be maneuvered to the location in the blocked artery and to provide access to covered side-branches in arteries and dilation (Osterle et al., 1998). The disadvantage is the stress support for the stent to the arterial wall to maintain it open for blood flow. The advantage of the slotted design is the high strength and greater surface coverage to maintain the arterial wall open after deployment. The disadvantage is the less flexibility of the stent in the artery to be maneuvered into bifurcated arteries.

1.2.3 Histology of Restenosis

Implanting stents into patients leads to complex tissue interactions. Ratner (2004) discusses the deployment of the stent causing damage to the endothelial lining and stretching of the vessel wall leading to restenosis. This stimulates the accumulation and adherence of platelets and leukocytes. The stent initially is covered by a platelet fibrin coating and then eventually covered by an endothelium-lined neointima. This

causes the wires of the stent to be embedded in a layer of smooth muscle cells in a collagen matrix. The thickening of this tissue layer causes the release of growth factors, chemotactic factors, and inflammatory mediators from platelets and other inflammatory cells. This results in the increased smooth muscle cell migration and proliferation and an increase in the extracellular matrix molecules causing the narrowing of the lumen and leading to restenosis. Other contributing factors to restenosis include the post-stent plaque burden being the immediate effect of intervention on the vessel wall (Bennett et al., 2001). The neointimal accumulation correlates the extent of initial injury from the stenting process. This causes in-stent restenosis to be a problem with 20-30% of patients requiring repeated procedures. Tuzcu et al. (2003) also discusses the plaque burden associated with positive remodeling and a sudden rupture to "vulnerable" lesions causing acute coronary syndromes. This aids in the destabilization of atherosclerotic lesions and initiates plaque rupture and thrombosis. Therefore, the interaction of the stent deployment leads to complicated tissue remodeling resulting in restenosis.

1.2.4 Finite Element Analysis of Stents

High pressure stent deployment was introduced in 1993 by Antonio Colombo. Knowledge of the stent behavior has been determined by lab experimental testing. The slotted stent design and the coil stent design have been used for deployment. The slotted designs have better surface coverage whereas the radial support for the artery and the coil design provides a high degree of flexibility but not structural strength in the radial direction (Etave et al., 2001).

The most commonly used stent is the high pressure balloon stent. The high pressure balloon stent causes the stent to plastically deform and press against the arterial wall as shown in Fig. 1.6.

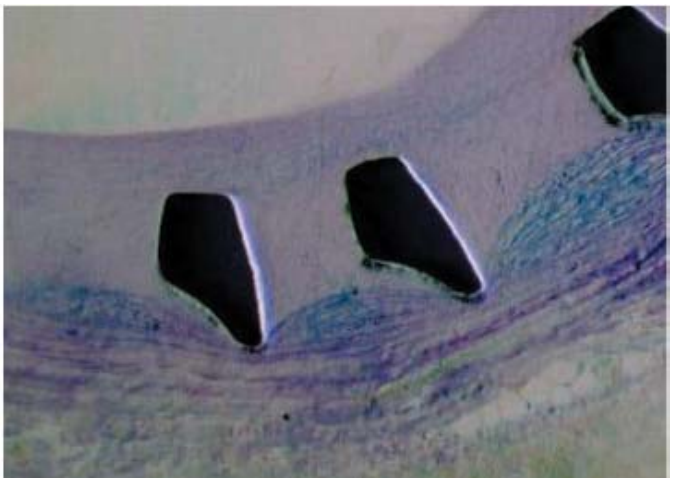

Fig. 1.6 Clemson Stent struts pressing against the arterial wall
(Source: Sullivan et al., 2002)

Sullivan et al. (2002) studied the effects of the stent struts on the arterial wall. These struts on the stent damage the internal elastic lamina, deep arterial wall, and results in cell proliferation and restenosis. Understanding the stress and deformation behavior of stents during deployment and after deployment can assist in the design of the stent. Computer aided design (CAD) is used to create stent models for finite element analysis (FEA), which analyzes the stress and strain behavior of the design, including the interactions of contacting bodies.

Etave et al. (2001) compares the slotted tube design to the coil design using Abaqus FEA software. The material for both of the stents is 316L stainless steel. The stent deployment is modeled in three different methods. The first method is the stent expansion performed by increasing the displacement of the radial nodes of the stent.

The second method is the stent compression performed by decreasing the displacement of the radial nodes of the stent. The third method is the conformability being modeled with the stent on two supports and a negative radial force applied opposite of the supports. Their results show the coil stent requires less pressure to deploy the stent than the slotted stent. The thickness of the tubular stent affects the mechanical properties by requiring higher pressure to expand the stent. On the other hand, the coil stents were shown to have higher internal elastic recoil, more flexibility, smaller external compressive pressure, less metal coverage area, and a larger foreshortening range.

The tube slotted stent design has been the subject to many FEA studies. The study of stent tube designs with u-shaped struts has been analyzed by Migliavacca et al. (2005). This stent was made of stainless steel, 316. A 3-D model was made of the undeformed shape of the stent. An increasing pressure load up to 1.2 MPa is applied to the stent surface to cause the expansion of the stent. The results show the plastic deformation of the stent causes the expanded struts to maintain the shape of the stent and large von Mises stresses at the center of the u-shaped struts. The balloon model does present some discrepancies in the experimental and computational tests. The central radial recoil measured before and after loading at 0.5 (MPa) is 1.1% for the experimental test and the FEM simulation calculated the central radial recoil to be 1.2%. The balloon does have an impact in comparing the numerical data to the experimental test.

The balloon is used to inflate the stent and to cause it to plastically deform. Etave et al. (2001) discusses the pressure required to deform the balloon is the

difference between the internal pressure and the external pressure of the balloon. With a stent mounted onto the balloon, the external pressure is not equal to zero and the amount of pressure required to expand the stent is the sum of the nominal balloon inflation pressure (NBP) and the stent deployment pressure (SDP). Also, a compensatory elastic recoil pressure (CERP) is incorporated to the required pressure to expand the stent to counteract the intrinsic elastic recoil that occurs after deflation. The interaction of the balloon can be used in contact analysis.

The enhancement of FEA permits the modeling of contact between the balloon and the stent. Contact involves the interaction of two bodies: target and contact. The target is usually the body with a larger Young's modulus and the contact is the softer material body. After these bodies collide, the tangential and normal stress values are calculated at their interface as the loading applied to the target increases. This type of simulation could be used to determine the contact between the balloon and the stent. Wang et al. (2004) describes the expansion behavior of the stent using contact elements to interact with a balloon. For the FEM they assumed symmetry and model a 120° section of the balloon and 1/6 of the stent model. The stent material is stainless steel, 316 with an internal pressure of 1.0(MPa) applied to the inner surface of the balloon. The balloon is assumed to behave as a simple isotropic cylindrical shell and friction is ignored between the balloon and the stent. The contact elements between the surface of the balloon and the stent analysis use large displacement and apply stress stiffness using an arc-length method to solve the static analysis. Their results show the increase in the

strut width of the end rings with reduction of the overall length of the balloon can reduce the stent's foreshortening and can control the dogboning during expansion.

The geometry of the stent design can also be analyzed. Chua, MacDonald, Hashmi (2004) analyzed the effects of varying slotted tube stent struts with FEA. Five configurations of stents are considered with different widths of the struts in each configuration. The stent material is stainless steel 304 with the balloon material being polyurethane. Symmetry for the model was considered and 1/8 of the model was used for the simulation. The pressure loads were applied to the inner surface of the balloon. The results show an increase in the number of slots increases the expansion of the stent with the elastic recoil stopped at 1(MPa) to plastic deformation of the stent. The range of shrinkage from elastic recoil was 16.6%-19.7% with the foreshortening increased with increased strut width. The stresses localize in the corner of the struts with a residual stress of 450(MPa). In conclusion, the strut length does not have a major effect on the stress distribution and foreshortening but a major effect on elastic recoil.

Stents have also been investigated for their interaction with arterial walls using FEA. Lally, Dolan, Pendergast (2005) investigates the stresses being imposed on the interior wall of the coronary artery. A wire mesh stent design is compared to a slotted tube stent's interactions with the arterial vessel. The material is stainless steel 316 for both stents. A deformable-deformable contact described the contact between the stent and the arterial vessel. Appropriate boundary conditions were applied for radial expansion of the arterial vessel. The stent was modeled in its expanded state and the arterial wall is expanded beyond the stent's diameter. After inflation, the pressure was

reduced in the arterial vessel causing it to collapse onto the stent. Longitudinal tethering was simulated applying longitudinal stretch to the artery. The analysis concluded the wire stent has more flexibility, conformability to the arterial vessel and lower stress values than the tubular stent design.

Walke, Liang, Yang, Qi (2005) also used numerical simulation to determine the expansion of a vascular stent with the consideration of the arterial vessel interaction. A 3-D model is created of a GENESIS^{TM} stent and arterial vessel. The stent material is stainless steel 316 and an incremental load of 0.1(MPa) up to 0.5(MPa) was applied to the inner surface of the stent. Experimental testing was used to determine the diameter expansion of the stent. The results from the simulation have a high correlation between the experimental results and the simulation for the diameter expansion of the stent. The experimental data and the numerical simulation showed an increase in the pressure above 0.3(MPa) did not cause an increase in the diameter of the stent. The simulation concluded the stress values did not exceed 10(MPa) and the strain values are high in the bending regions of the stent. This analysis was useful in determining the stent stress distributions and optimizing the geometry of the stent design.

The increasing use of FEA and improvements in CAD and FEA software enables a better understanding and simulation of the stress and strain behavior of stents during expansion.

1.2.5 Objectives for Stent Analysis

The objective of this work is to develop a finite element model and simulate the expansion of the stent. This simulation allows the analysis of the deformation of the

stent by the balloon and the identification of the plastic deformation regions surpassing the von Mises yielding criteria. Finally, the effects of Young's Modulus on maximum shear stress and the effect of axial displacement on maximum shear stress are analyzed.

CHAPTER 2

METHODS AND MATERIALS

2.1 Overview

Stent deployment uses a high pressure balloon to inflate the stent. This high pressure causes plastic deformation of the material which permits the stent to remain in an open position. Understanding the manufacturing assembly of the stent is vital in creating the 3 dimensional stent models. This information is taken from Dr. Shih Horng Su's dissertation (Su, 2000). Also, verification testing of the stent is needed to ensure the accuracy of the FEA simulation.

2.2 3-D Model

2.2.1 SolidWorks 2004

SolidWorks 2004 is 3-D geometric modeling software. This software permits accurate creation of a 3-D component with given appropriate dimensions. The balloon and stent are created into 3-D models in SolidWorks 2004. These models are exports as parasolid files to ANSYS for creation of the FEM.

2.2.2 Stent Model Dimensions

The coil design is similar to a spring shape but with internal coils inside the spring shape. Also, this stent incorporates reinforcement rods bonded to the outside of the stent. This type of design should enhance the rigidity and maintain the flexibility of

the stent. The design parameters are the stent has a length of 15(mm) and 12 coils. Within one coil are three internal coils as shown in Fig. 2.1.

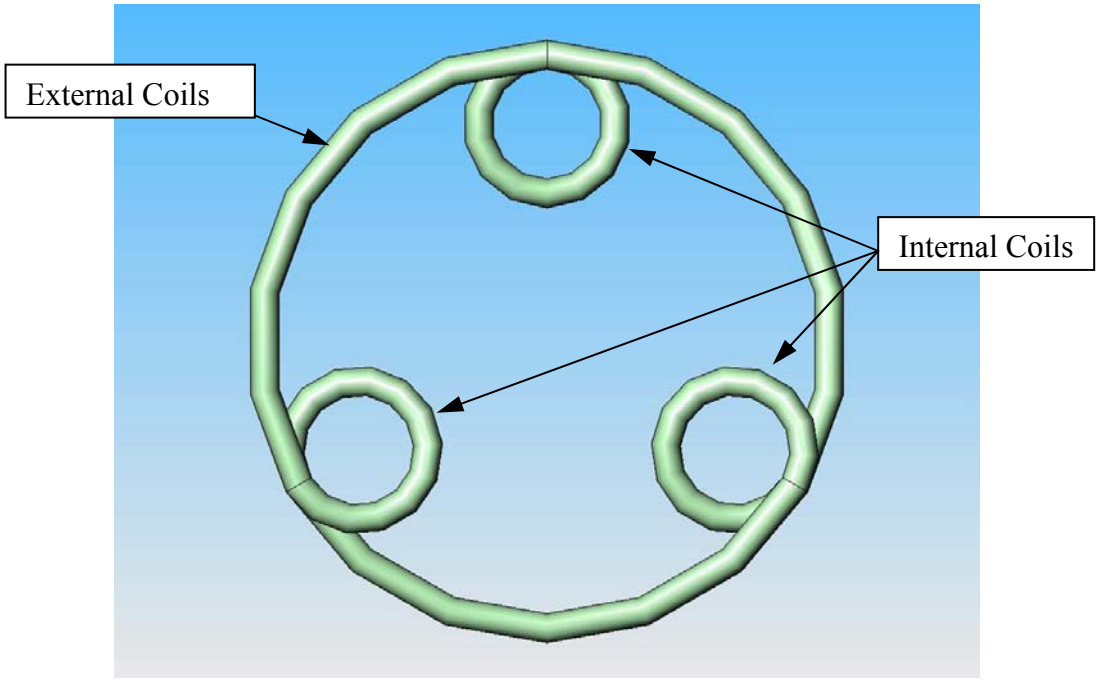

Fig. 2.1 Internal and External Coils of the Stent

An assembly of a fixture is created to accurately locate the internal coil diameters. A base plate is made first to dimensions of 4(mm) x 4(mm) x 5(mm). Then rods of dimensions Ø0.26(mm) with a length of 15(mm) and one rod of Ø0.62(mm) with a length of 15(mm) are created. The base plate assembly with three rods defining the distance for the internal coils is shown in Fig. 2.2.

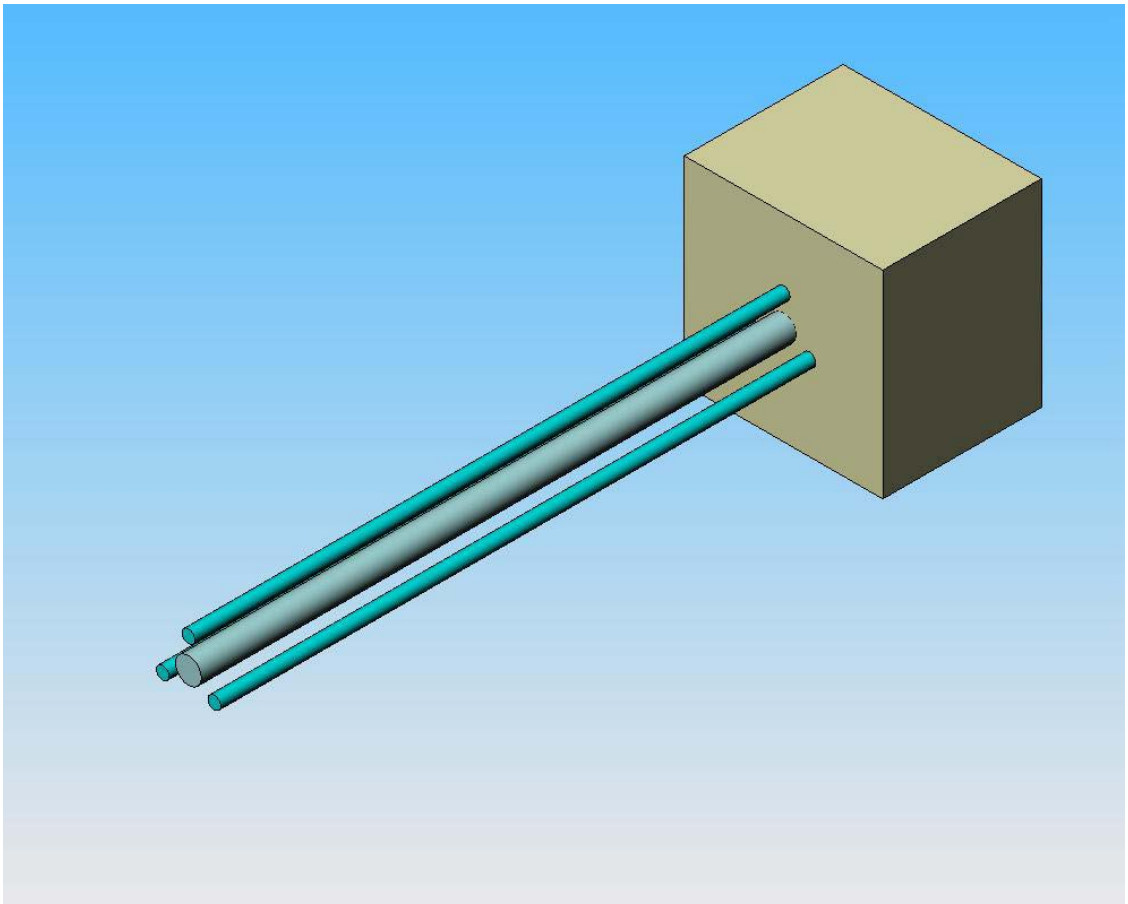

Fig. 2.2 Base Plate Assembly Isometric View

The internal coils are 120° from each other on a 0.75(mm) radius. The coils of the stent are created using helical sweeps. These are divided into the outer coils and the internal coils. The outer coils are based on a Ø1.96(mm) and a pitch of 0.62(mm) with 0.33 revolutions. The fiber diameter is 0.10(mm). The internal coils are based on a Ø0.47(mm) and a pitch of 0.20(mm) with 1.00 revolutions. These features are created to complete 360° forming one loop of the stent. The dimensions in millimeters are specified in Fig. 2.3 and a detailed drawing is presented in the appendices.

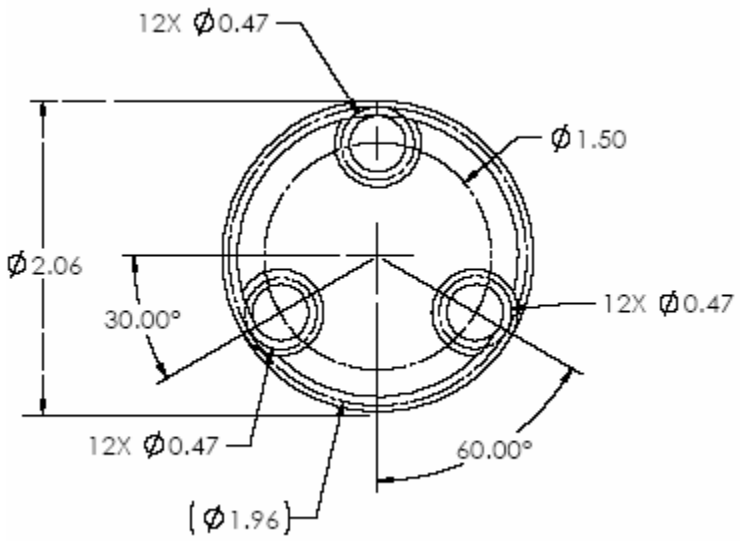

Fig. 2.3 Internal and External Coil Specifications

This loop is patterned along the axis until they complete the length of the 15(mm) requirement for the stent as shown in Fig. 2.4.

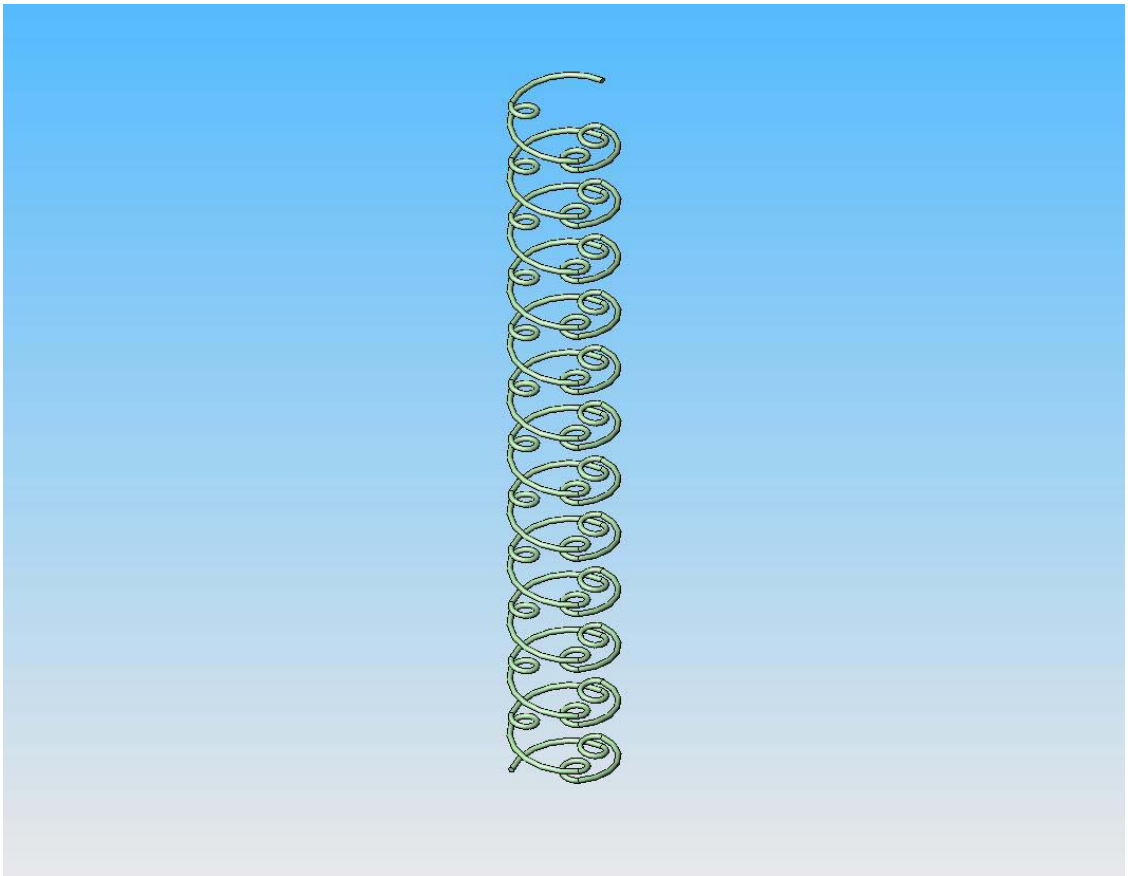

Fig. 2.4 Coil Stent Design

2.2.3 Reinforcement Fibers and their Dimensions

The axial reinforcement fibers are modeled as straight rods with a Ø0.10(mm) and a length of 15.00(mm). The 3 fiber reinforcement rods are aligned to the stent at 120° angles apart between the internal coils and the ends are fixed to the base of the stent. These fibers are assembled to the stent as shown in Fig. 2.5.

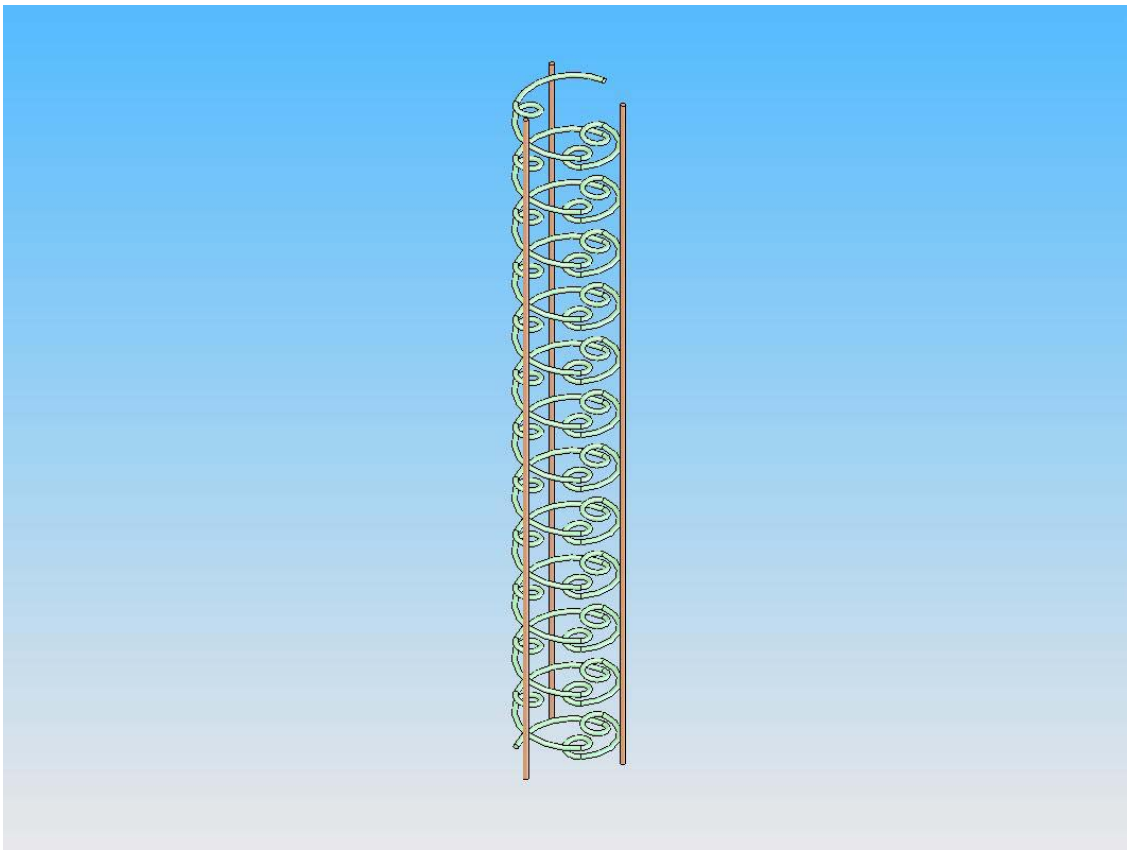

Fig. 2.5 Reinforcement fibers attached to Coil Stent

2.2.4 Stent 120° Section

The stent model has a 120° section cut from its base. Fig. 2.6 shows this section of the model. This is the portion of the stent that is used for the FEM.

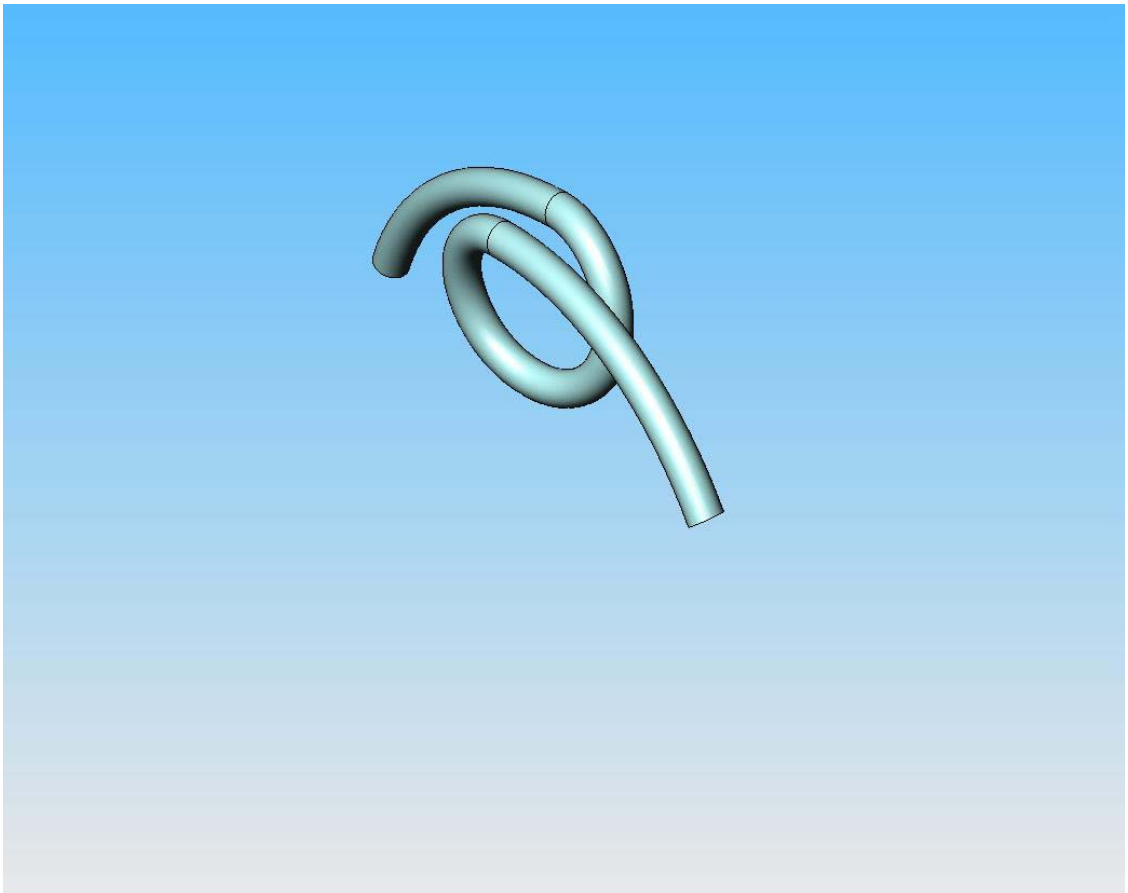

Fig. 2.6 120° Section of Stent

The 120° section of the stent is used with boundary conditions applied to the ends of the fiber as shown in Fig. 2.7.

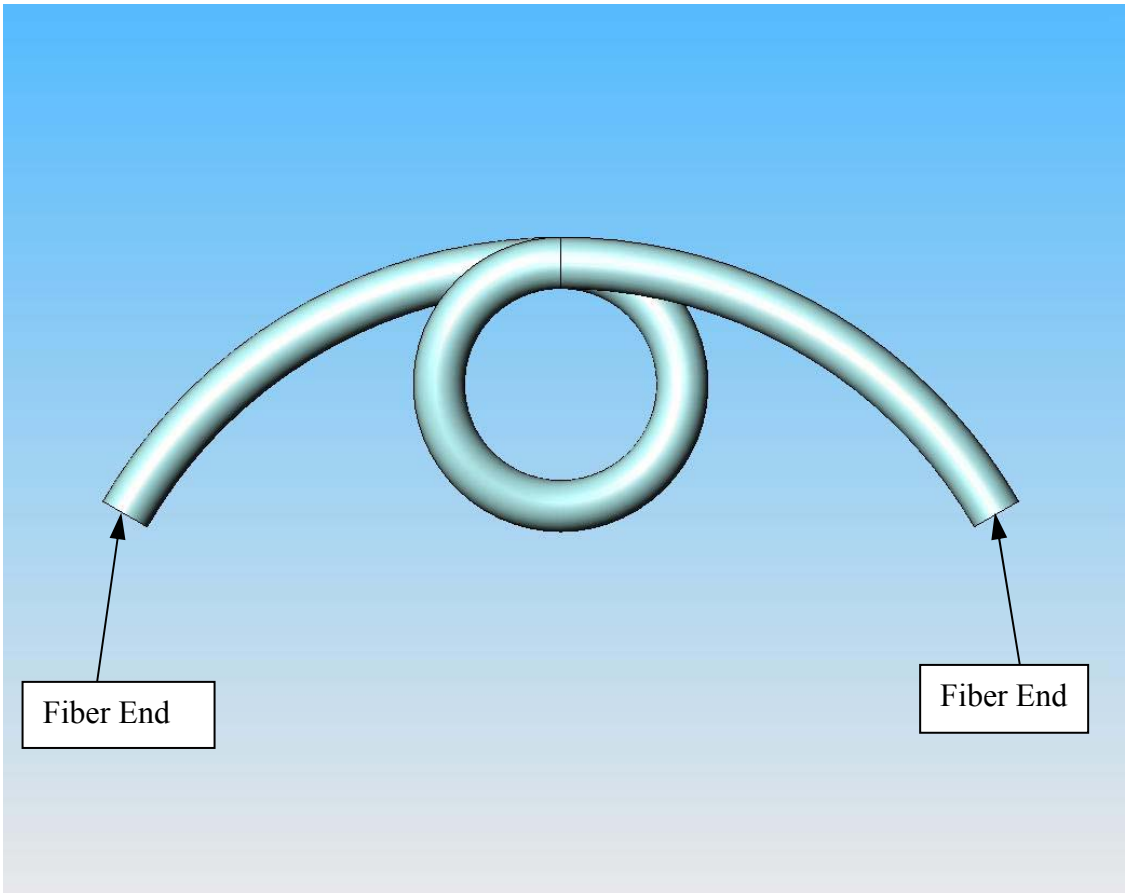

Fig. 2.7 120° Section Showing ends for Boundary Conditions

A 120° section is used because of higher spatial resolution and fewer elements and faster runtime for the analysis. Similar boundary conditions are applied to each end of the fiber. The 120° section of the assembly model is exported as a parasolid file. This file format keeps the dimension of the parts and position of the assembly in units of meters.

2.3 Finite Element Model and Simulation

2.3.1 Importing Parasolids into ANSYS

The assembly model parasolid is directly imported into ANSYS 8.1 as a volume. Therefore, no Boolean operations need to be exercised to have the correct volume of the model. The volume is imported in units of cubic meters.

2.3.2 Meshing

Meshing the model creates the elements to represent the volume of the stent. First, the stent volume is assigned brick elements 20 node Solid 95. This is a second order interpolation function providing large deflection and strain analysis supporting nonlinear material plasticity, creep, and stress stiffening. A mapped mesh is used to generate the mesh of the stent as shown in Fig. 2.8. A mapped mesh can be used for a 3 or 4 sided closed region. This mesh is user defined for the stent by dividing the lines along the length of the stent into 72 segments and the diameter of the stent into 12 segments. This permits finer meshing in the coil regions if required. The number of elements used for the model is 1656 with 8146 nodes.

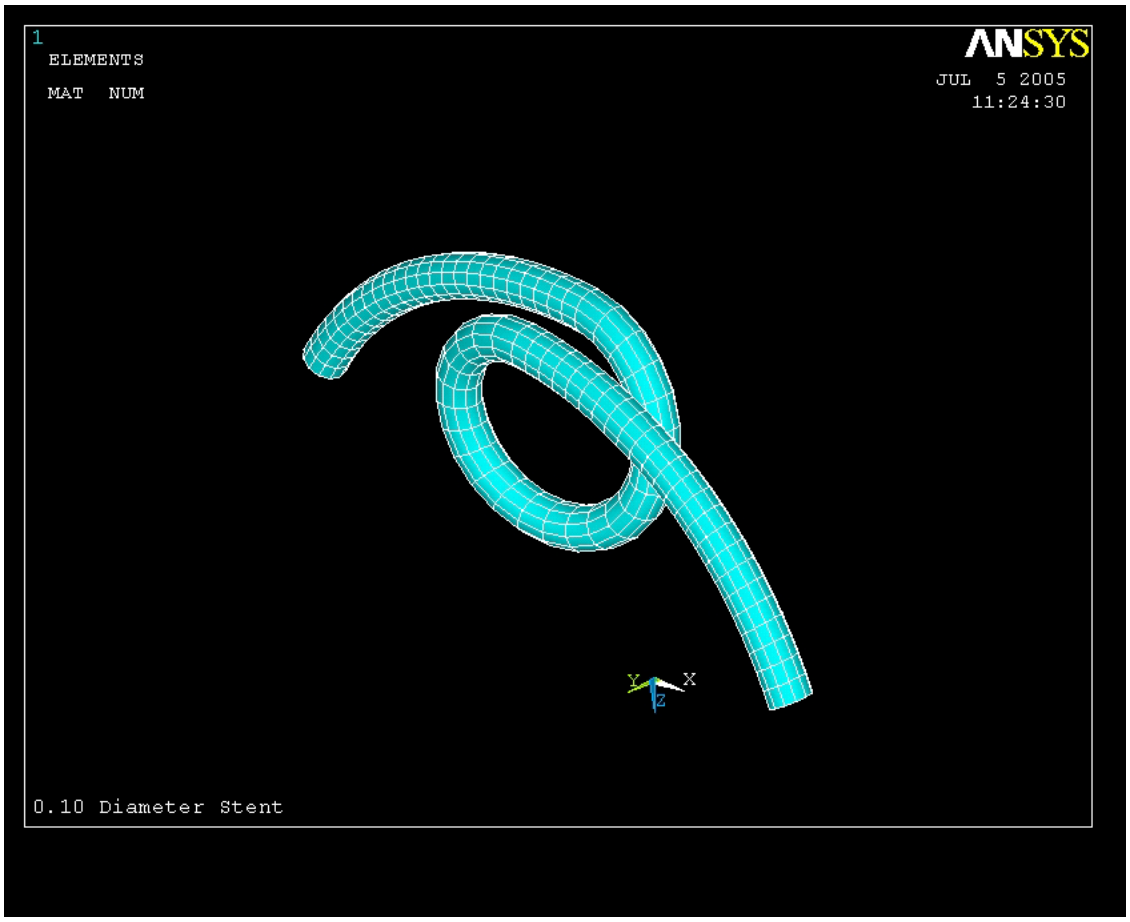

Fig. 2.8 Finite Element Model of Stent

2.3.3 Material Properties

The material assigned to the stent volume is Poly-L-Lactic Acid (PLLA) with a Young's modulus of 7043(MPa), and a Poisson's ratio of 0.35. This is the baseline case to study for the simulation. The von Mises stresses, principal stresses and strains, and the stents deformation are analyzed in the simulation. The PLLA material is simulated by using nonlinear plastic material properties for the multilinear setting in ANSYS. For the baseline case stress-strain data was used from Dr. Shih Horng Su's dissertation (Su, 2000). To examine the sensitivity of the PLLA fiber stent to changes in material stress-

strain data, we carried out three additional simulation cases with different stress-strain data from Dr. Shih Horng Su's dissertation (Su, 2000). Stress-strain data for all four cases are plotted in Fig. 2.9 in true (Cauchy) stress and true (logarithm) strain. Note that Cauchy stress, σ_t, and logarithm strain, ε_t, are related to engineering stress, σ_e, and engineering strain, ε_e, through equation (1) and (2). Cauchy stress and logarithm strain will be referred to as stress, strain from this point.

(1) $\sigma_t = \sigma_e * (1 + \varepsilon_e)$

(2) $\varepsilon_t = ln(1 - \varepsilon_e)$

Stress-strain data for all four cases are given in Table 2.1 (Case 1), Table 2.2 (Case 2), Table 2.3 (Case 3) and Table 2.4 (Case 4).

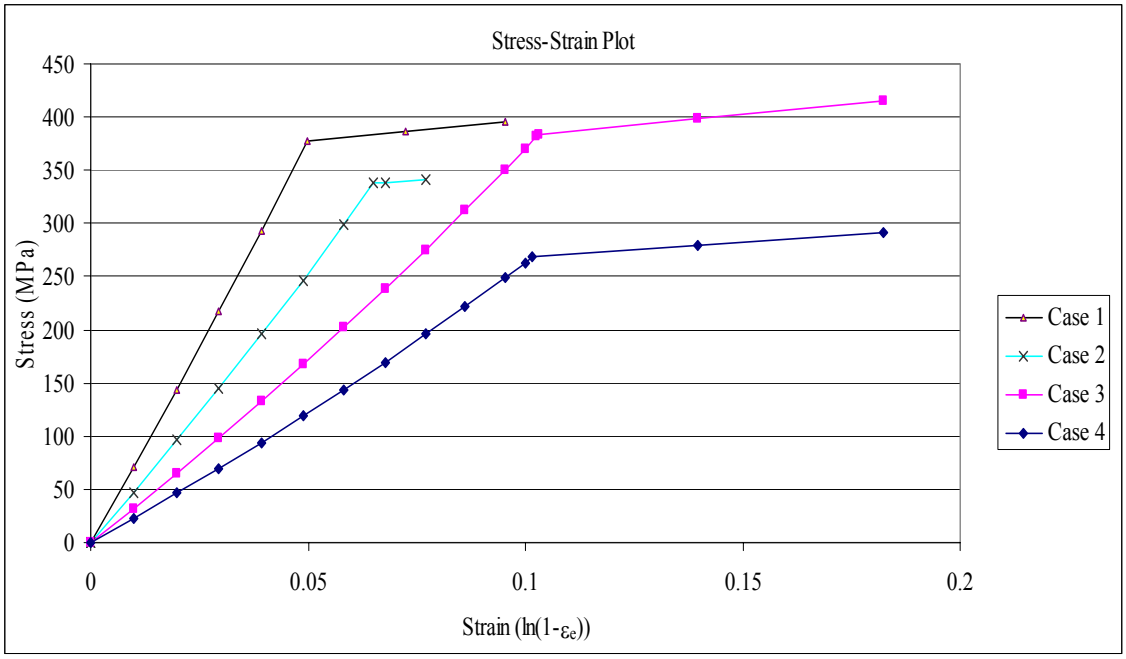

Fig. 2.9 Stress-Strain Plot for Different PLLA Fibers

Table 2.1 Baseline Case 1: Young's Modulus of 7043(MPa)

Strain ($\ln(1-\varepsilon_e)$)	Stress (MPa)
0.010	7.113E+01
0.020	1.437E+02
0.030	2.176E+02
0.039	2.930E+02
0.050	3.775E+02
0.068	3.843E+02
0.095	3.951E+02

Table 2.2 Case 2: Young's Modulus of 4701(MPa)

Strain($\ln(1-\varepsilon_e)$)	Stress (MPa)
0.010	4.748E+01
0.020	9.590E+01
0.030	1.453E+02
0.039	1.956E+02
0.049	2.468E+02
0.058	2.990E+02
0.065	3.377E+02
0.068	3.385E+02
0.077	3.417E+02

Table 2.3 Case 3: Young's Modulus of 3189(MPa)

Strain ($\ln(1-\varepsilon_e)$)	Stress (MPa)
0.010	3.221E+01
0.020	6.506E+01
0.030	9.854E+01
0.049	1.674E+02
0.068	2.389E+02
0.086	3.128E+02
0.100	3.700E+02
0.103	3.835E+02
0.140	3.979E+02
0.182	4.152E+02

Table 2.4 Case 4: Young's Modulus of 2266(MPa)

Strain ($\ln(1-\varepsilon_e)$)	Stress (MPa)
0.010	2.289E+01
0.020	4.623E+01
0.030	7.002E+01
0.049	1.190E+02
0.068	1.697E+02
0.086	2.223E+02
0.100	2.629E+02
0.102	2.684E+02
0.140	2.788E+02
0.182	2.910E+02

2.3.3 Boundary Conditions

Assumptions must be made for the boundary conditions of a math model to be constrained. The appropriate boundary conditions are determined from verification testing, see section 2.4.

2.3.3.1 Axial Displacement Boundary Condition

The axial displacement is 0.69(mm) for total displacement for each internal coil from 1 atmosphere (atm) to 14(atm). The 0.69(mm) axial displacement number is calculated from Table 3.3 by subtracting the stent radius at 0(atm) from 14(atm). The fiber has 7 coils in length with three small coils in each large coil. The axial displacement 0.68(mm) is divided by 7 and then by 3 to determine the displacement value of 0.032(mm) to apply as the boundary conditions of the FEM for a 120 degree model.

2.3.3.2 Radial Displacement Boundary Condition

To simulate the radial expansion of the fiber, the coordinate system for the ends of the fiber is rotated to have the y-direction facing the global y-direction and the x-

direction pointing in the radial expansion direction. The radial displacement values are applied to the x-direction on the fiber ends and the axial displacement is applied to the nodes on the positive y-direction on the ends of the fiber for the right side and to the nodes on the negative direction on the ends of the fiber for the left side. The z-direction and rotation for each axis is set to zero. This causes the model's motion to expand radially and the longitudinally along the coil's axis. The radial displacement is assumed to be equal at every applied load step. This radial displacement is determined by taking the overall change in diameter and dividing it by the pressure range. A value of 0.049(mm) based on the measurement from the verification testing (section 2.4) was applied as the radial displacement. Fig. 2.10 illustrates the fiber ends constrained.

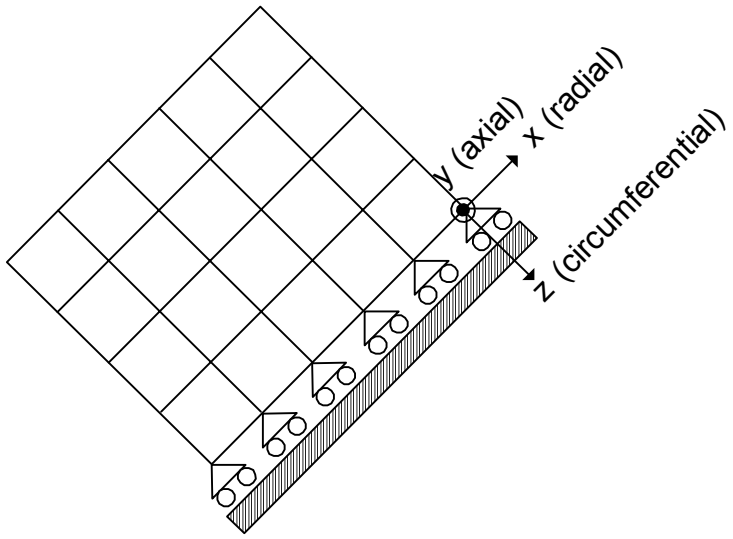

Fig. 2.10 Fiber End Boundary Condition

2.3.4 Numerical Solution Setup

This analysis uses the load steps range from 1(atm) to 14(atm) with each load step incrementing by one atmosphere. The pressure loads are applied in the unit of Pascals to 8 elements at the base of the coil as shown in Fig. 2.11 and Fig. 2.12. This causes the resulting loading pressure to be applied in the direction perpendicular to the element surface which is the appropriate direction for the balloon expansion to make contact with the stent. Thirty load sub steps are applied as the minimum number of sub steps and fifty sub steps are the maximum applied sub steps to the analysis. This ensures the force values can converge for the model. This is a static nonlinear analysis with large displacements.

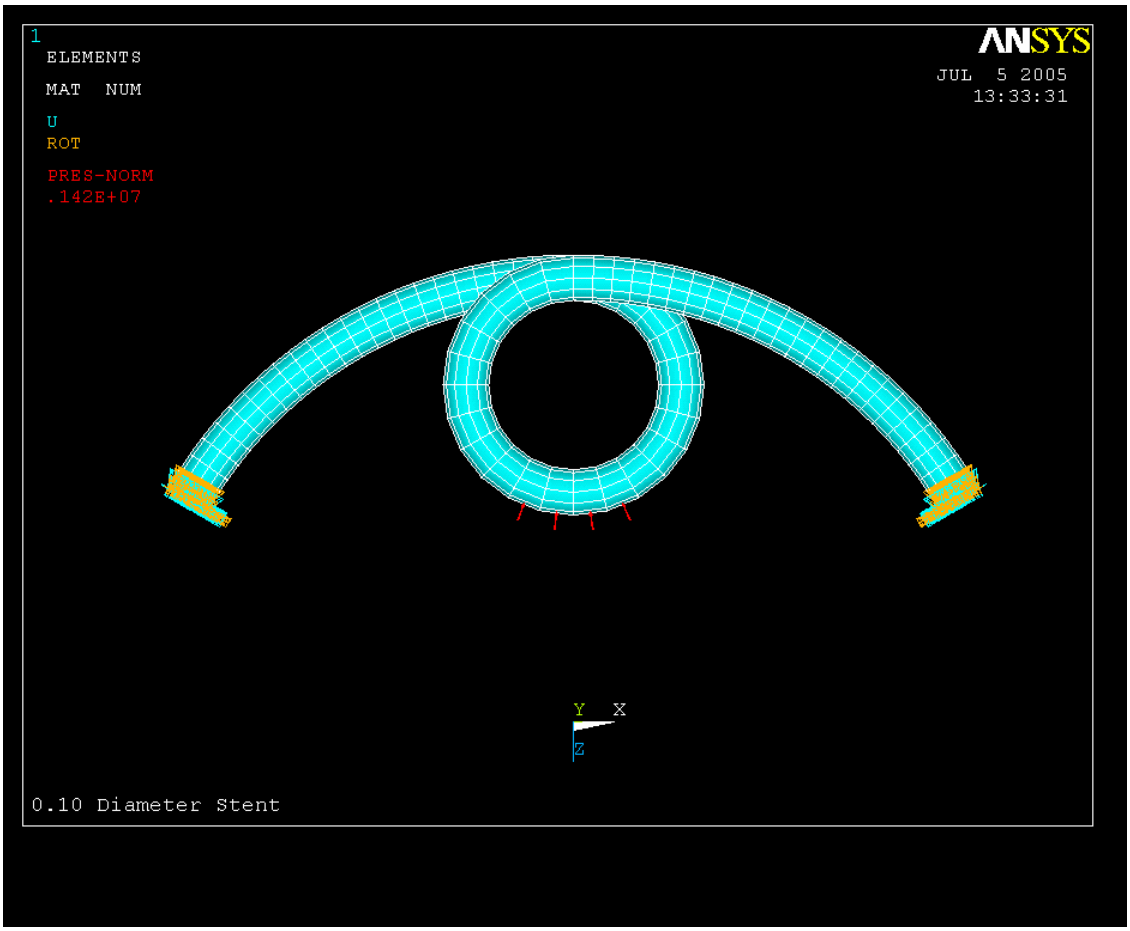

Fig. 2.11 Pressure Load applied to FEM Front View

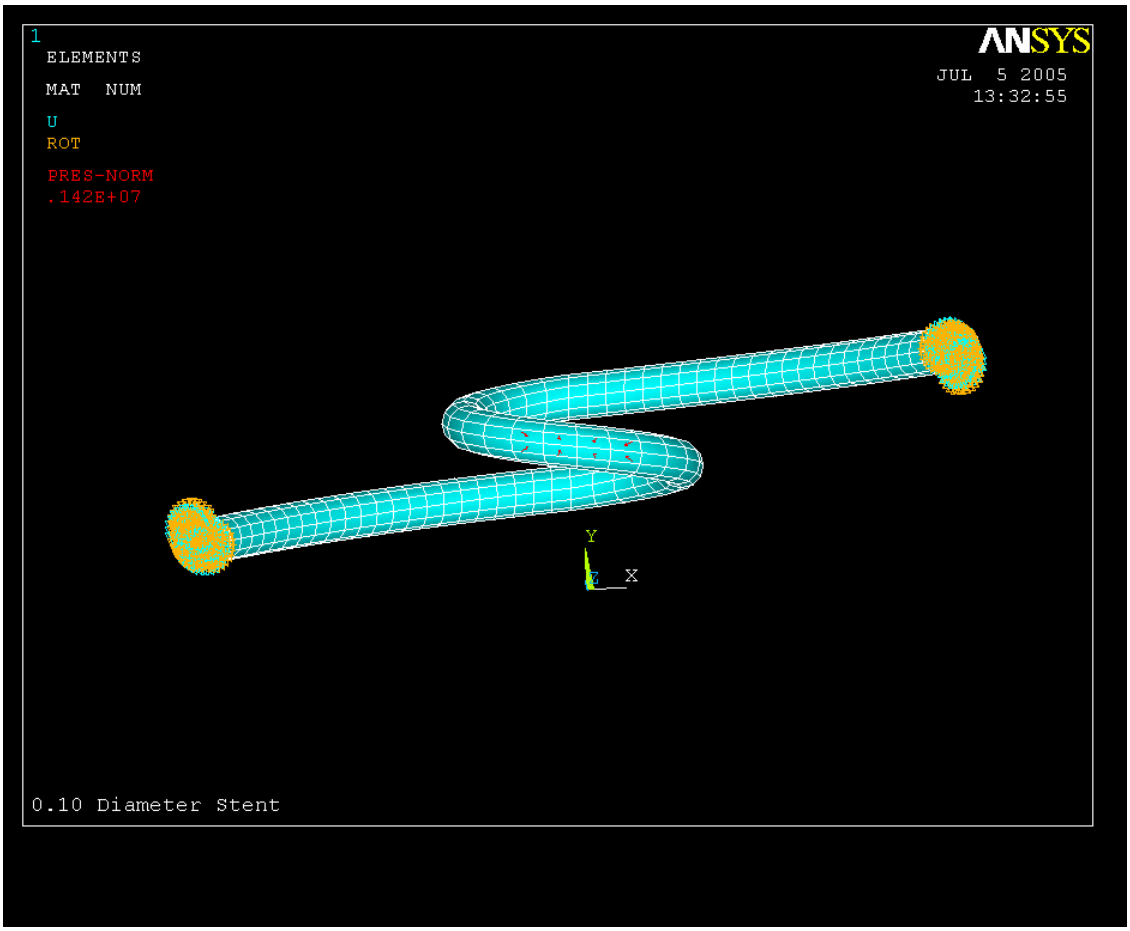

Fig. 2.12 Pressure Load applied to FEM Bottom View

2.4 Verification Data

2.4.1 Testing Materials

A 2.5 mm catheter (Boston Scientific), a syringe pump (Encore), a plastic tube with a three way valve, a digital camera (Cannon Powershot A80) with 3X magnification lens, photography stand, a video camera (Sony Handycam DCR-TRV130) and a PLLA coil stent supplied by Dr. Eberhart's research lab of UT Southwestern are used for the experiment. The syringe tube and catheter are secured to a base to keep the parts from moving the stent. First, examination of the balloon

expanding without the stent is performed. The digital camera is mounted on the photography stand to be facing the top of the stent and another digital camera is facing perpendicular to the stent. The video camera is position 3 feet away on a tripod stand and zoomed to maximum capacity as shown in Fig. 2.13.

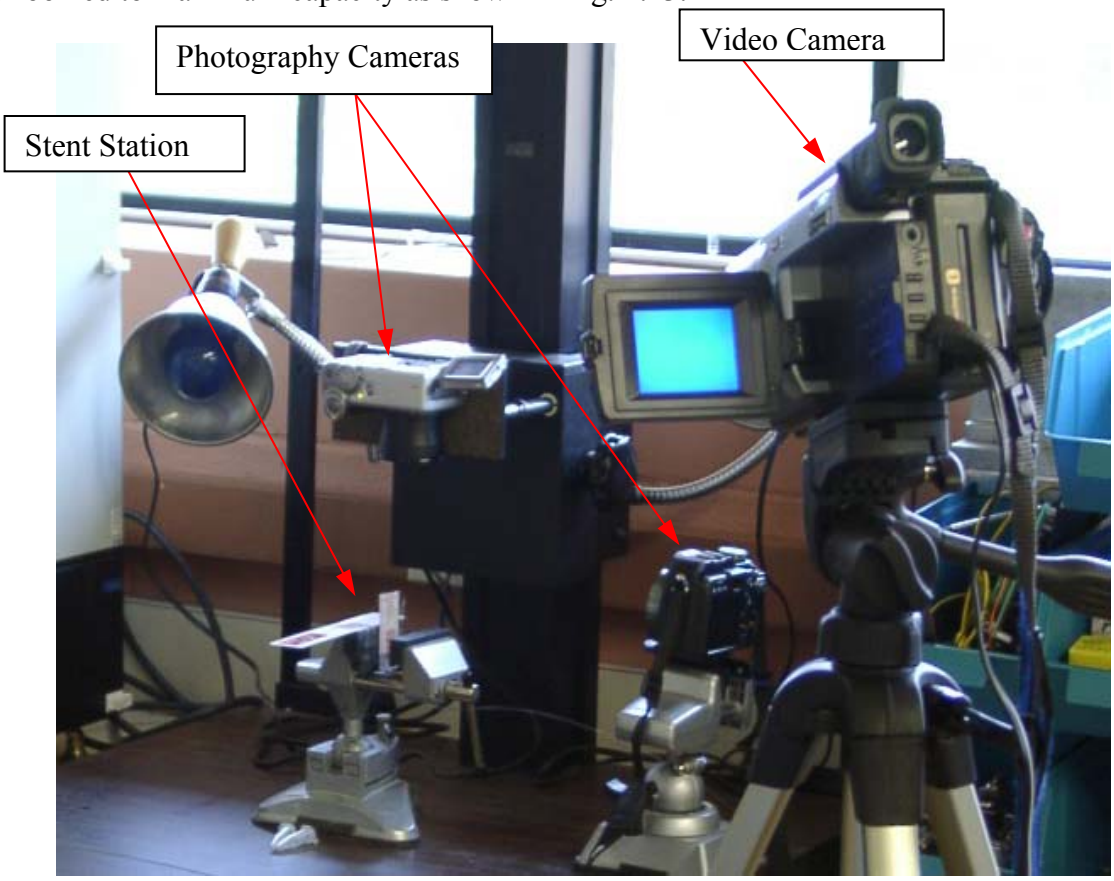

Fig. 2.13 Verification Test Setup

2.4.2 Testing Procedure

The syringe pump is filled with water and attached to the catheter with pressure increments of 1 atmosphere (atm) being applied up to 14(atm). To ensure full equilibrium of the balloon at each pressure level, a constant pressure is maintained for a minimum of 60 seconds before increasing to the next pressure level. Photos of the

balloon were taken at each pressure level for post-experiment analysis. A photo of the balloon at 7(atm) is as shown in Fig.2.14. The balloon was deflated after reaching 14(atm).

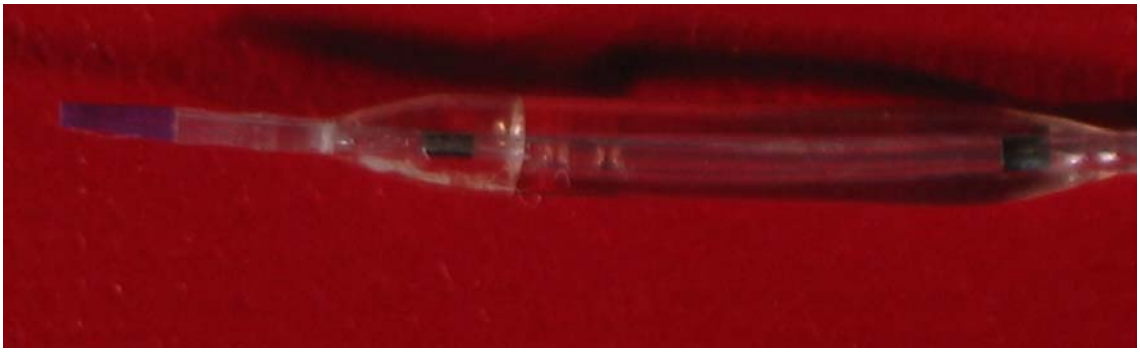

Fig. 2.14 Balloon Expansion at 7(atm)

2.4.3 Stent Testing Procedure

Next, the stent is mounted on the end of the catheter fitting over the balloon as shown in Fig. 2.15. Pressure increments of 1(atm) were applied up to 14(atm) with a minimum of 60 second intervals. Photos were taken at the end of each pressure increment. After reaching 14(atm), the balloon was deflated.

Fig. 2.15 Balloon with Stent before Expansion

2.5 Image Processing of the Photos for Deformation Measurements

The photos taken of the balloon and stent were enhanced using Photoshop 9.0. The enhancement adjusts the contrast of the image as shown in Fig. 2.16. The image is analyzed using Image J software from the National Institute of Health website. This software permits the calibration of the pixel size to the scale on the picture of 1(mm). The diameter was measured for stent 001, stent 002 and stent 003, and the balloon without a stent. The diameter measurements were taken on three coils at the center of the stent.

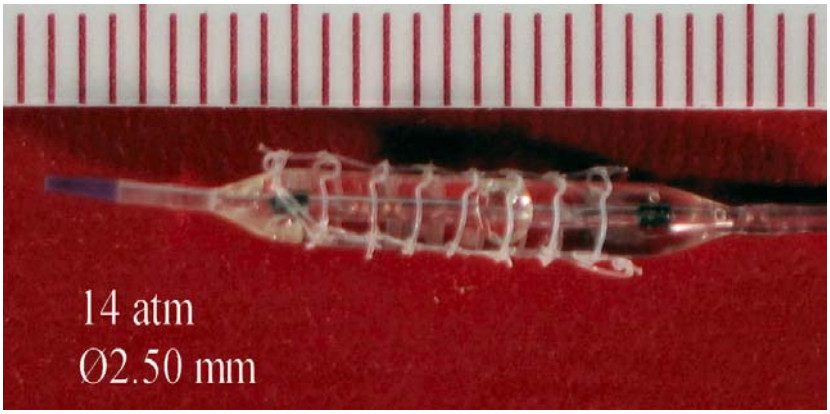

Fig. 2.16 Enhanced Stent 001 Photo at 14(atm)

2.6 Axial Displacement Analysis

The four Young's Moduli are analyzed with a Poisson's ratio of 0.4999 and increasing axial displacements. The increasing axial displacement ranges by a factor of 1x, 2x, and 3x. The 1x means one times the axial displacement value taken from the boundary conditions. The maximum shear stress is analyzed on the inside and outside surface of the model to determine if the maximum shear stress causes changes due to the increasing axial displacement.

CHAPTER 3

RESULTS

In this experiment, verification testing was performed to determine the balloon diameter and the stent deployment diameter during inflation. This data was compiled and used to establish the boundary conditions for the simulation.

3.1 Verification Data

3.1.1 Data of Balloon Expansion

The balloon was first tested to determine the diameter during inflation from 0(atm) to 14(atm) without a stent attached to the balloon. The balloon is originally in a flattened position. This is due to the shrinking of the balloon around the guide wire inside the balloon during deflation not being uniform. This can explain the large diameter of the balloon at 0(atm). The test was performed on one test trial. The results are shown in Table 3.1.

Table 3.1 Balloon without Stent Expansion Data

Trail #1	
Pressure (atm)	Diameter (mm)
0	1.78
1	1.82
2	1.85
3	1.88
4	1.92
5	1.95
6	1.97
7	2.05
8	2.08

Table 3.1- *Continued*

9	2.16
10	2.25
11	2.30
12	2.40
13	2.41
14	2.50

3.1.2 Data of Stent Expansion Deployed by increasing Balloon Pressure

The stent is expanded from 0(atm) to 14(atm). Photos presented in Fig. 3.1 – Fig. 3.15 show the deformation of both the stent and the balloon during deployment.

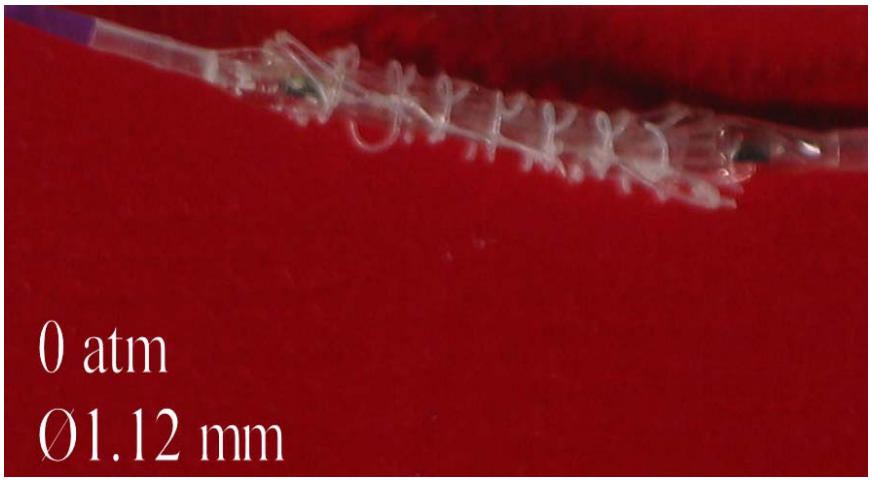

Fig. 3.1 Balloon with Stent Expansion at 0(atm)

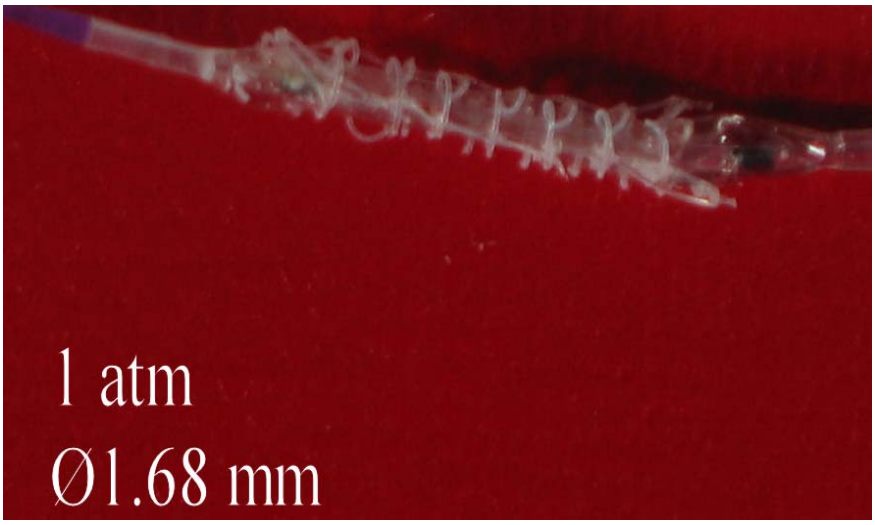

Fig. 3.2 Balloon with Stent Expansion at 1(atm)

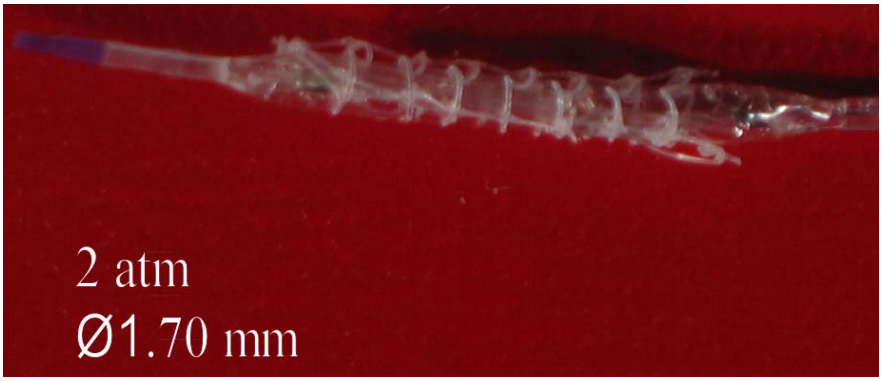

Fig. 3.3 Balloon with Stent Expansion at 2(atm)

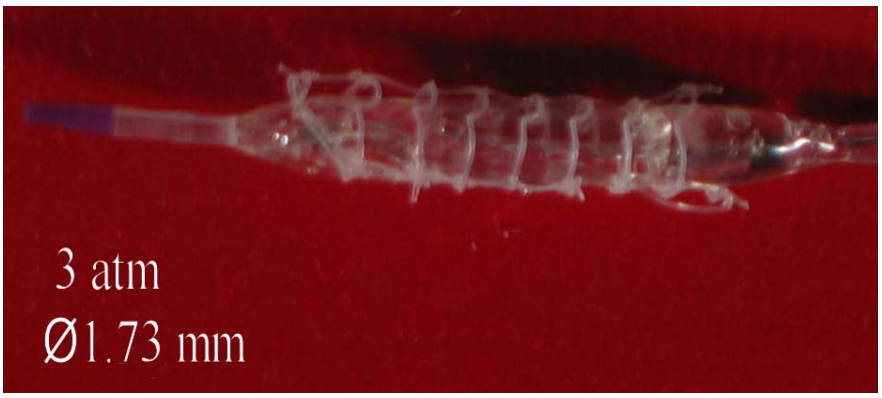

Fig. 3.4 Balloon with Stent Expansion at 3(atm)

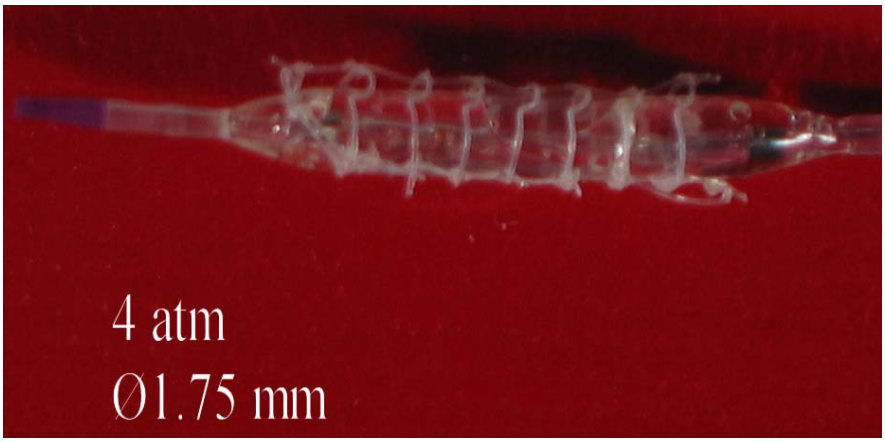

Fig. 3.5 Balloon with Stent Expansion at 4(atm)

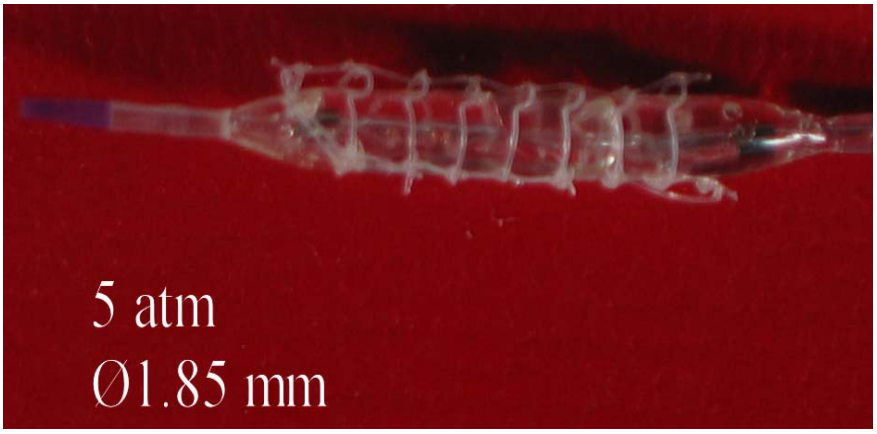

Fig. 3.6 Balloon with Stent Expansion at 5(atm)

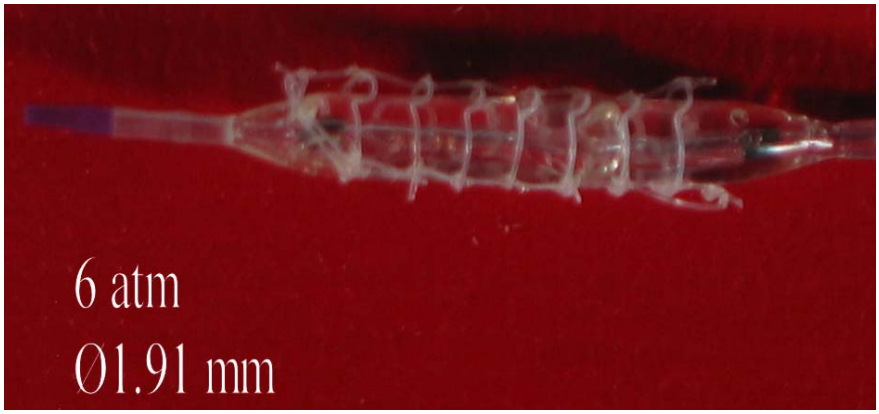

Fig. 3.7 Balloon with Stent Expansion at 6(atm)

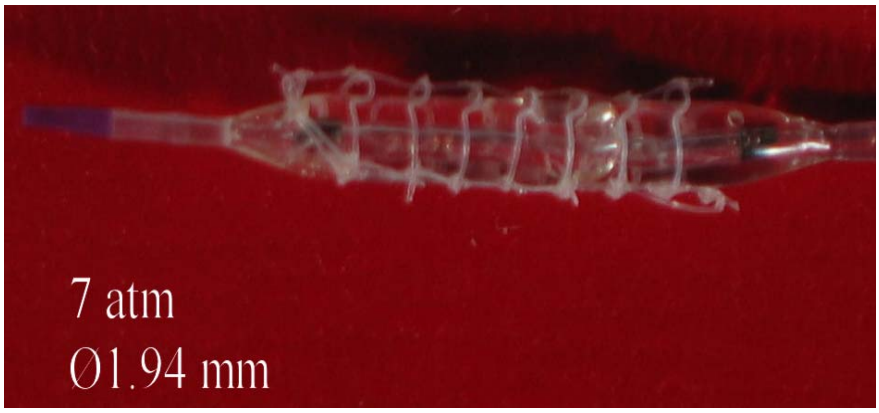

Fig. 3.8 Balloon with Stent Expansion at 7(atm)

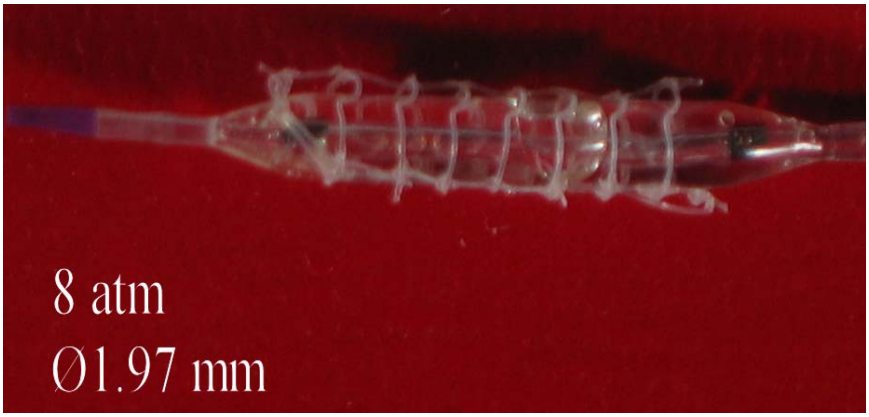

Fig. 3.9 Balloon with Stent Expansion at 8(atm)

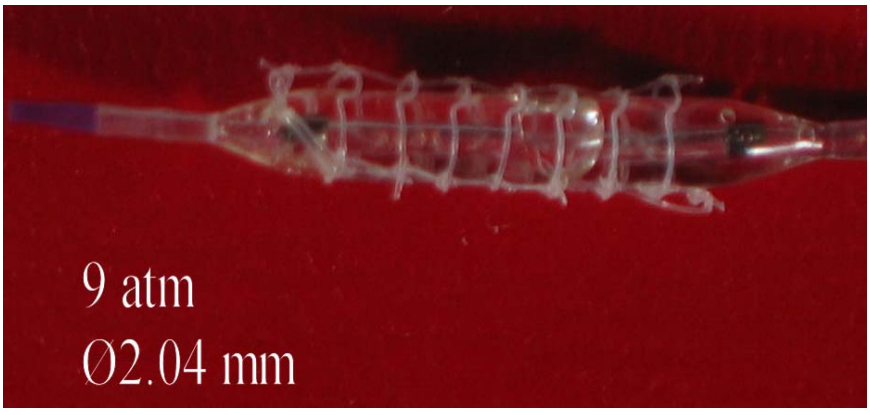

Fig. 3.10 Balloon with Stent Expansion at 9(atm)

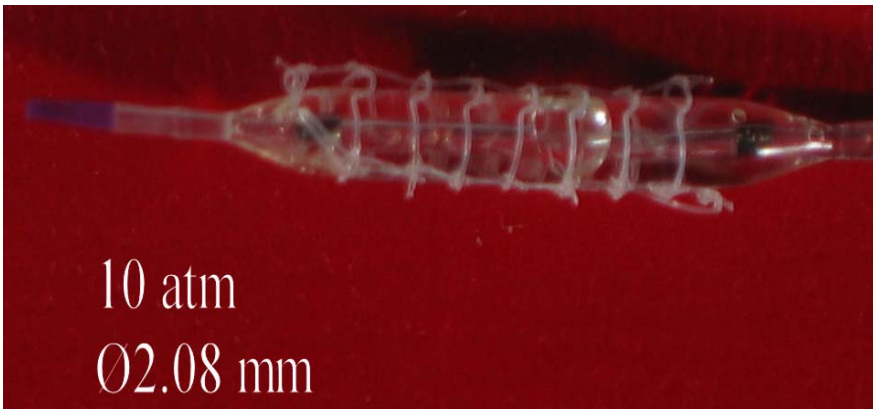

Fig. 3.11 Balloon with Stent Expansion at 10(atm)

Fig. 3.12 Balloon with Stent Expansion at 11(atm)

Fig. 3.13 Balloon with Stent Expansion at 12(atm)

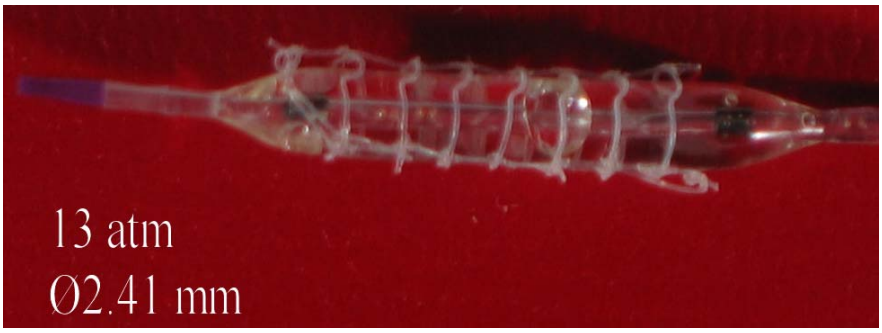

Fig. 3.14 Balloon with Stent Expansion at 13(atm)

Fig. 3.15 Balloon with Stent Expansion at 14(atm)

The stent deployment is performed on 3 different stents: Stent 001, Stent 002, and Stent 003. The diameter is recorded at each pressure reading incrementing by 1(atm). This data is shown in Table 3.2.

Table 3.2 Stent Expansion Data

Pressure (atm)	Stent 001 Diameter (mm)	Stent 002 Diameter (mm)	Stent 003 Diameter (mm)
0	1.12	1.46	1.72
1	1.68	1.55	1.80
2	1.70	1.62	1.81
3	1.73	1.70	1.84
4	1.75	1.74	1.86
5	1.85	1.76	1.91
6	1.91	1.88	1.93
7	1.94	1.95	1.95
8	1.97	2.06	2.00

Table 3.2 - *Continued*

9	2.04	2.11	2.14
10	2.08	2.19	2.19
11	2.29	2.20	2.24
12	2.40	2.24	2.28
13	2.41	2.33	2.33
14	2.50	2.37	2.38

A plot of the balloon without stent inflation and stent inflation data are presented in Fig. 3.16.

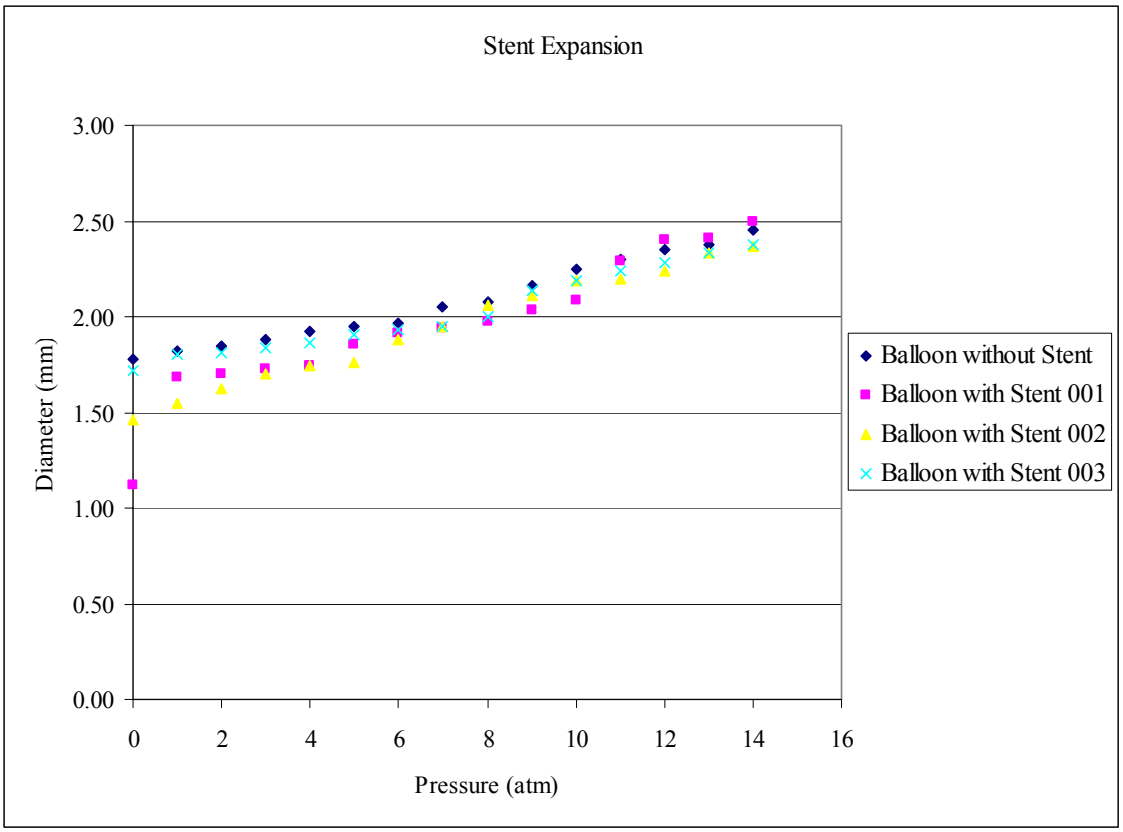

Fig. 3.16 Balloon without Stent and Balloon with Stent Expansion Plot for Stent 001, Stent 002 and Stent 003

3.1.3 Axial Elongation of the Stent under Balloon Pressure Increase

The stent shows some elongation in the axial direction, although much smaller compared to that in the radial direction. The percent elongation during inflation and the amount of axial lengthening were determined from the verification data. The axial displacement calculations are performed on Stent 001 as shown in Table 3.3.

Table 3.3 Stent 001 Axial Displacement and Percent Elongation

Inflation Pressure (atm)	Axial Length (mm)
0.00	8.65
14.00	9.33
Axial Displacement (mm)	0.68
Percent Elongation %	7.86%

3.2 Simulation Results

Understanding the effects of Young's modulus is critical in the further improvement and refinement for the development of the coil stent. It also helps identifying the stress behavior due to the stiffness of the stent through increasing radial and axial displacements during expansion. To facilitate and to illustrate the differences in stress, strain attributes along the fiber, a path is defined on the inside and the outside surface of the coil stent as shown in Fig. 3.17 and Fig. 3.18. The distance of the inside path is from 0(mm) to 3.22(mm) with an internal coil section is from 0.94(mm) to 2.28(mm). The distance of the outside path is from 0(mm) to 3.88(mm) with an internal coil section is from 1.04(mm) to 2.84(mm).

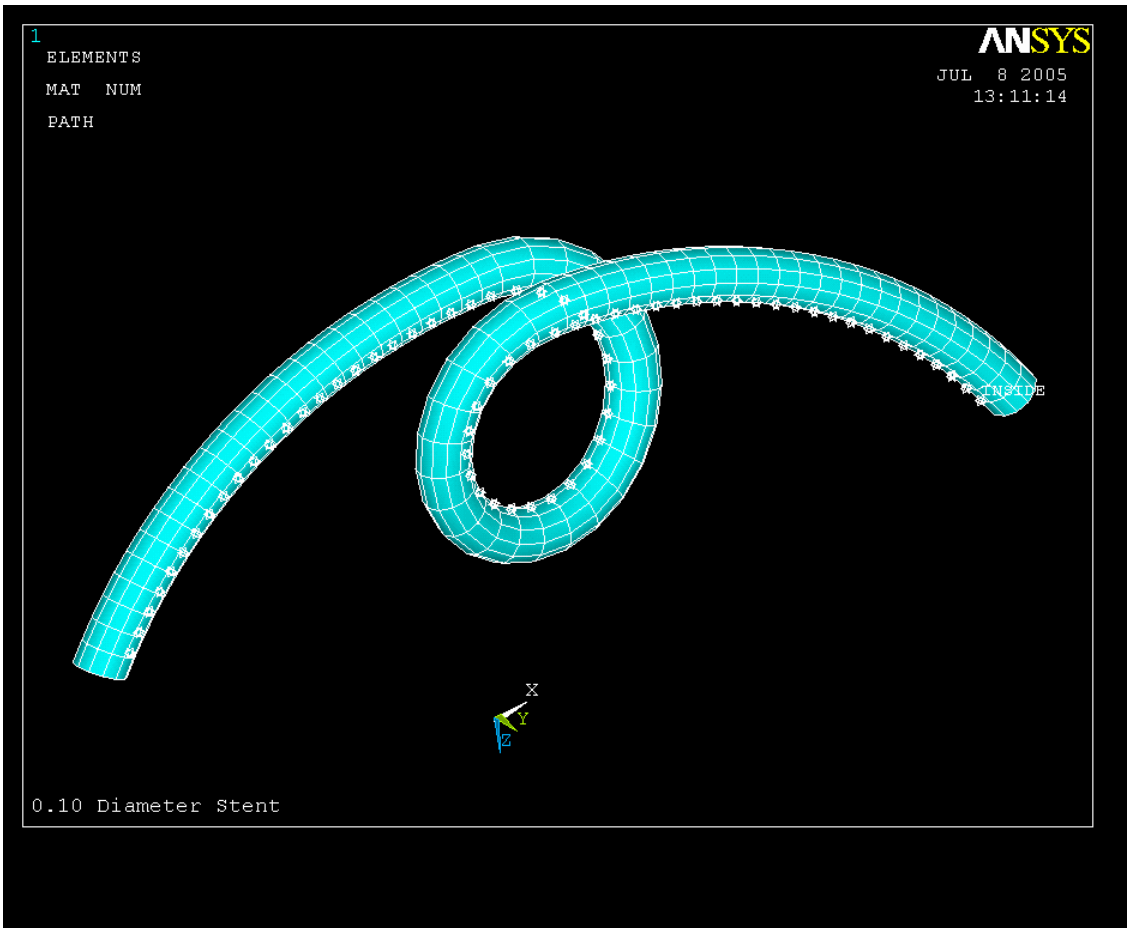

Fig. 3.17 Inside Surface Path

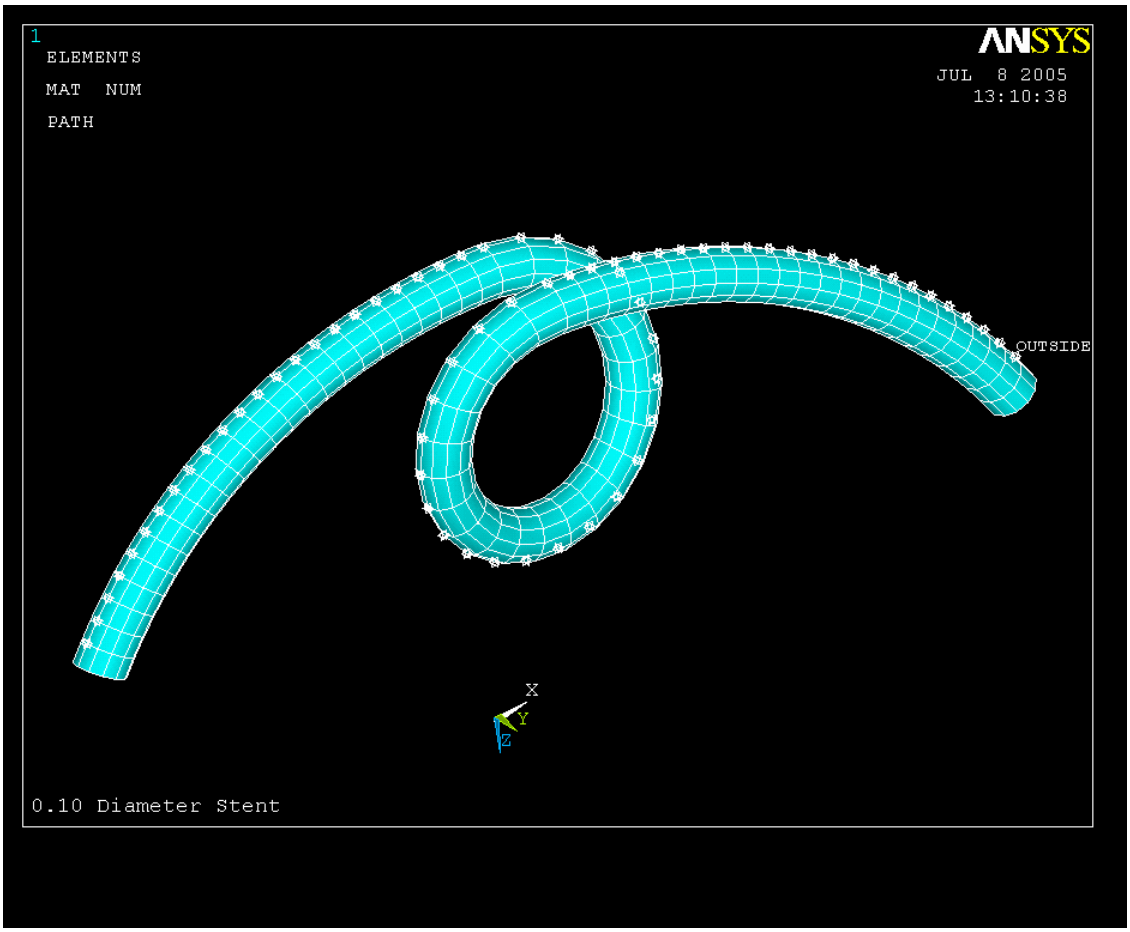

Fig. 3.18 Outside Surface Path

3.2.1 Principal Strain and Principal Stress Distributions along the Stent Fiber (Case 1)

The magnitude of the principal stress and principal strains on the surface are determined from these paths. E1 is the principal tensile strain and E3 is the principal compressive strain. S1 is the principal tensile stress and S3 is the principal compressive stress and Tmax is the maximum shear stress. The principal strains and principal stresses are shown in Fig. 3.19 – Fig. 3.22 for the inside surface and the outside surface at 1x the axial displacement values.

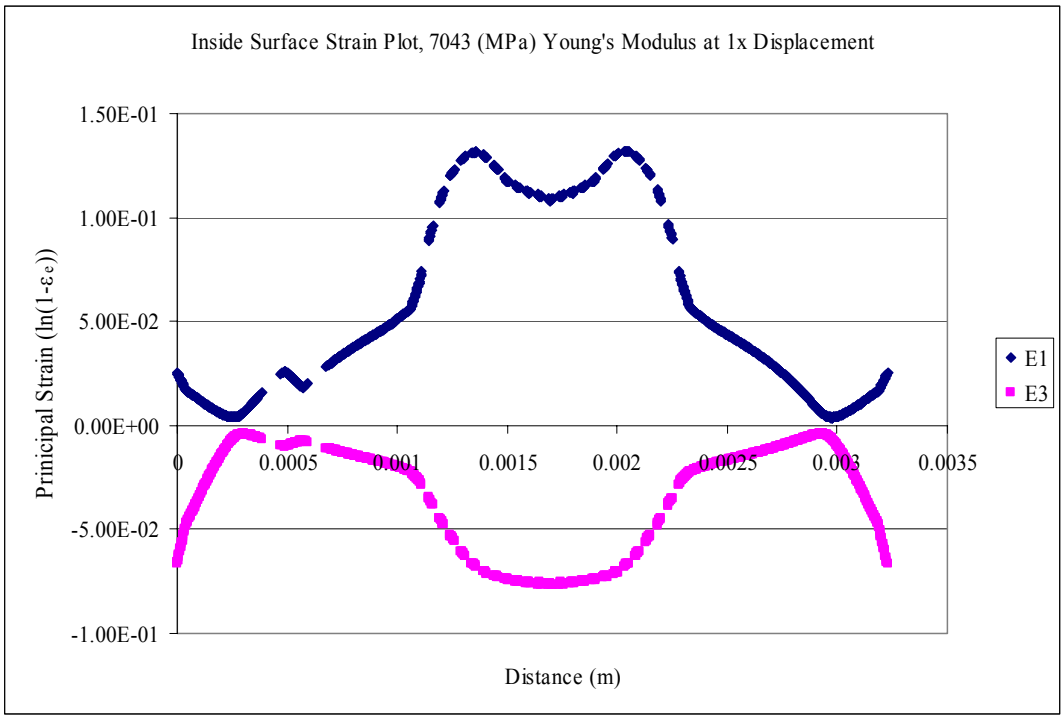

Fig. 3.19 Inside Surface Path Principal Strain E1, E3 for Case 1

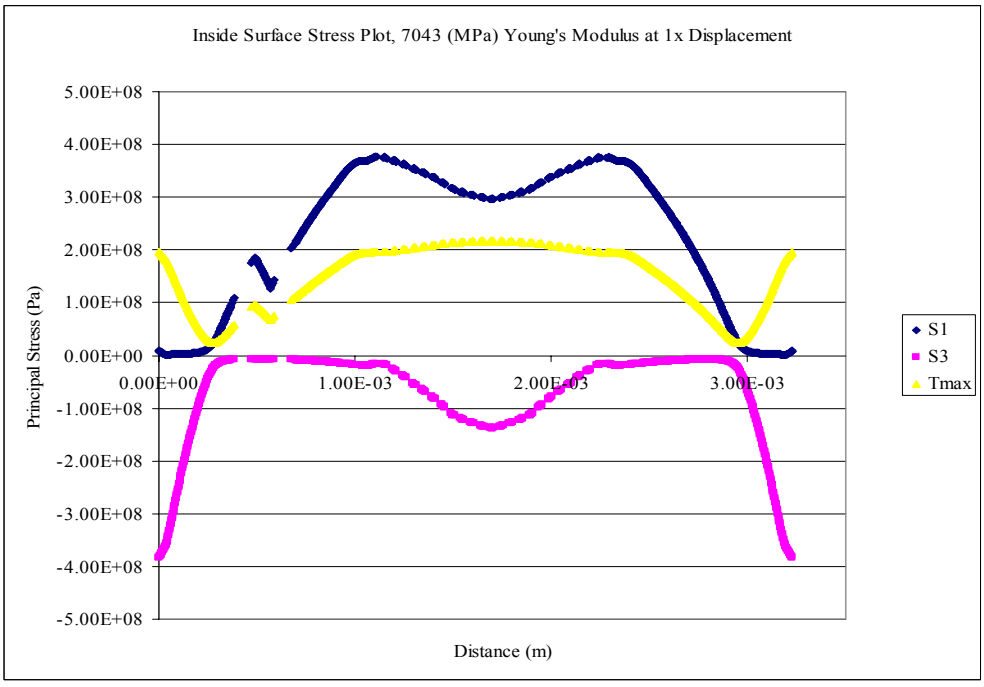

Fig. 3.20 Inside Surface Path Principal Stress S1, S3, and Tmax for Case 1

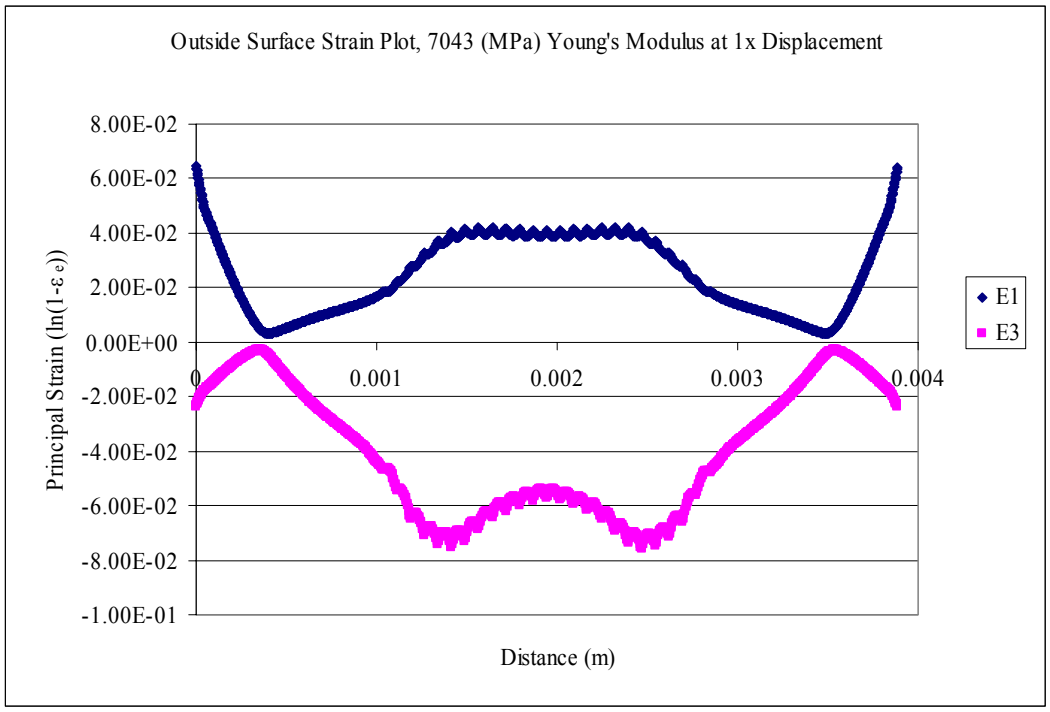

Fig. 3.21 Outside Surface Path Principal Strain E1, E3 for Case 1

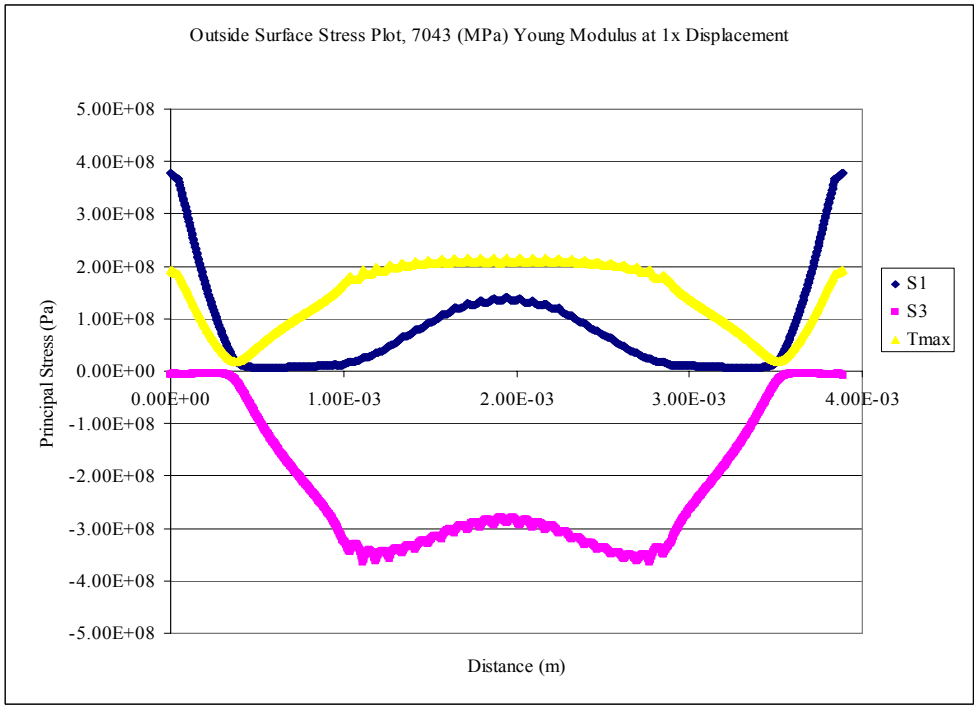

Fig. 3.22 Outside Surface Path Principal Stress S1, S3, and Tmax for Case 1

Vector plots for Case 1 of the principal stresses reveal the direction and change in principal stress component S1 and S3 along the fiber stent at 1 (atm) and 14 (atm) in Fig. 3.23 and Fig. 3.24.

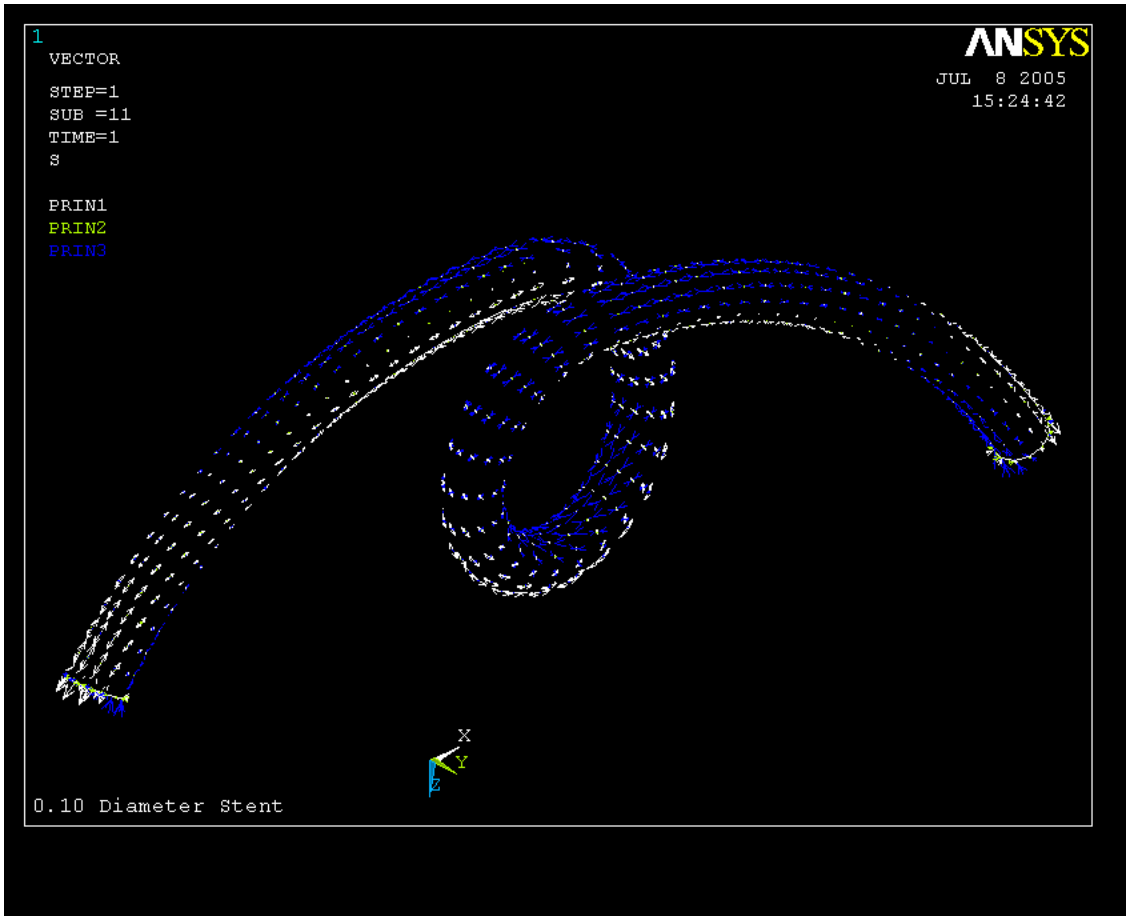

Fig. 3.23 Principal Stress Vector Plot in Deformed Position at 0.35 Poisson's Ratio, 1(atm)

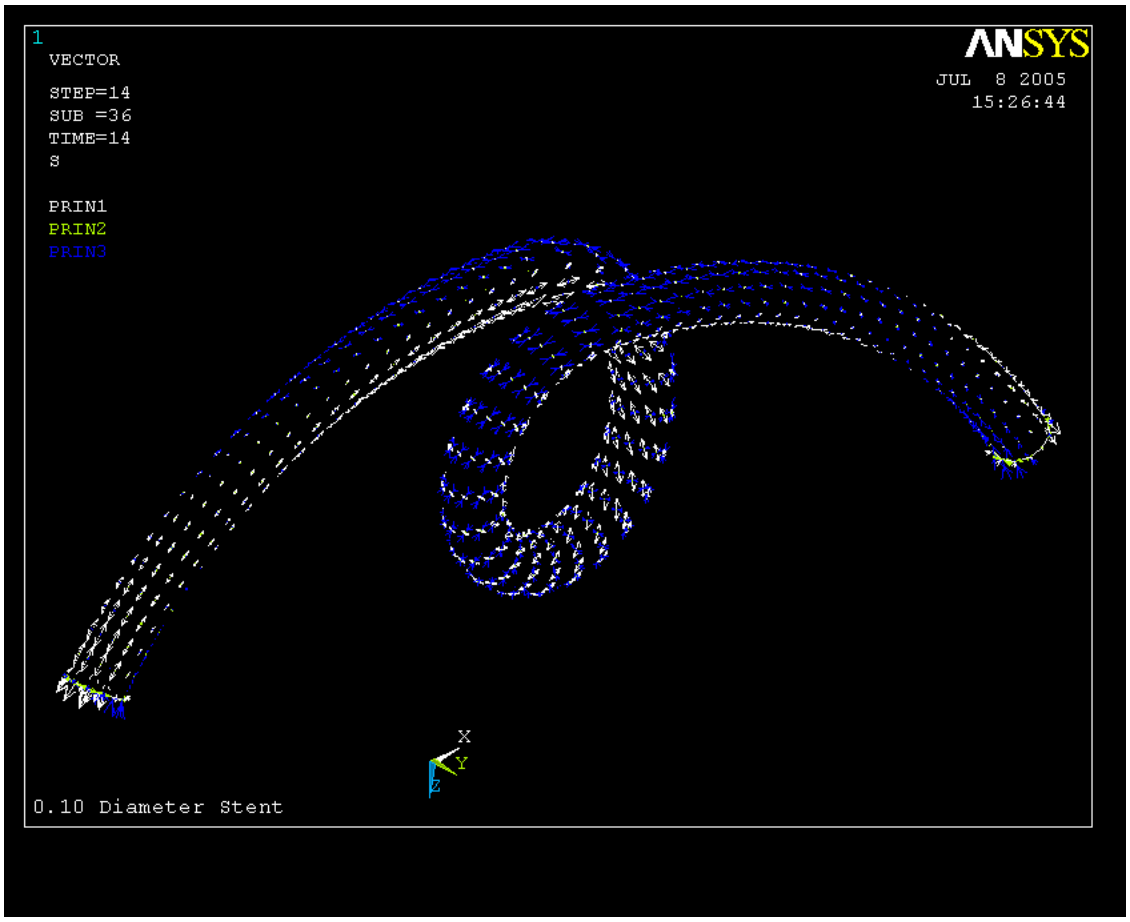

Fig. 3.24 Principal Stress Vector Plot in Undeformed Position at 0.35 Poisson's Ratio, 14(atm)

3.2.2 Effects of Young's Modulus

The different case studies are performed at a Poisson's ratio of 0.35. The principal strain and principal stress values are calculated and plotted on the inside and outside surfaces of the fiber as shown in Fig. 3.25 - Fig. 3.36.

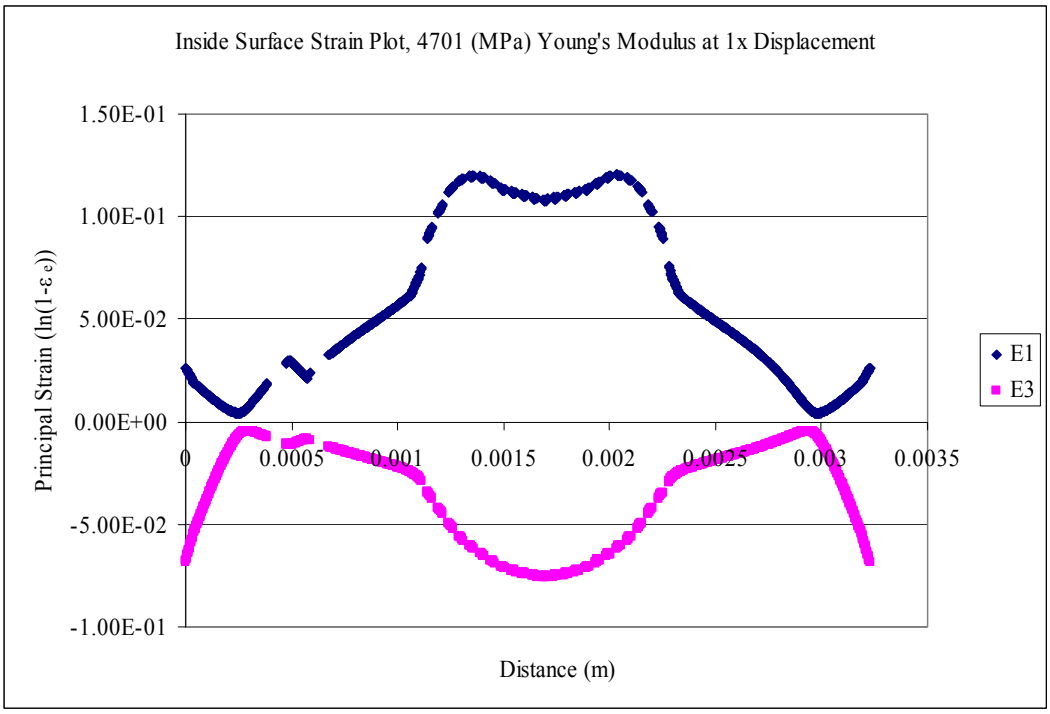

Fig. 3.25 Inside Surface Path Principal Strain E1, E3 for Case 2

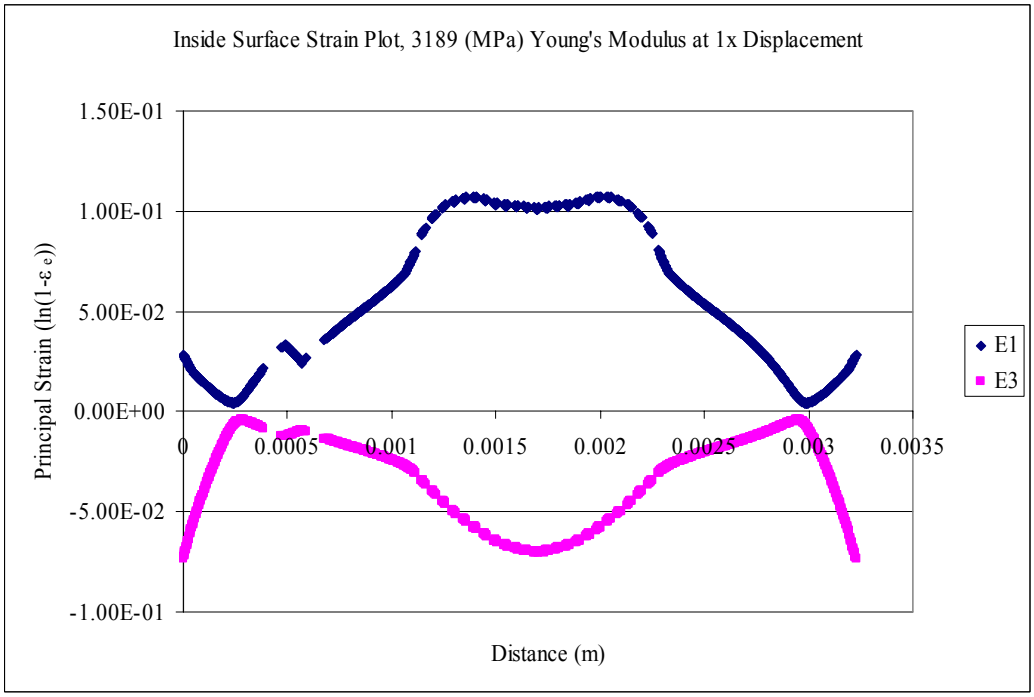

Fig. 3.26 Inside Surface Path Principal Strain E1, E3 for Case 3

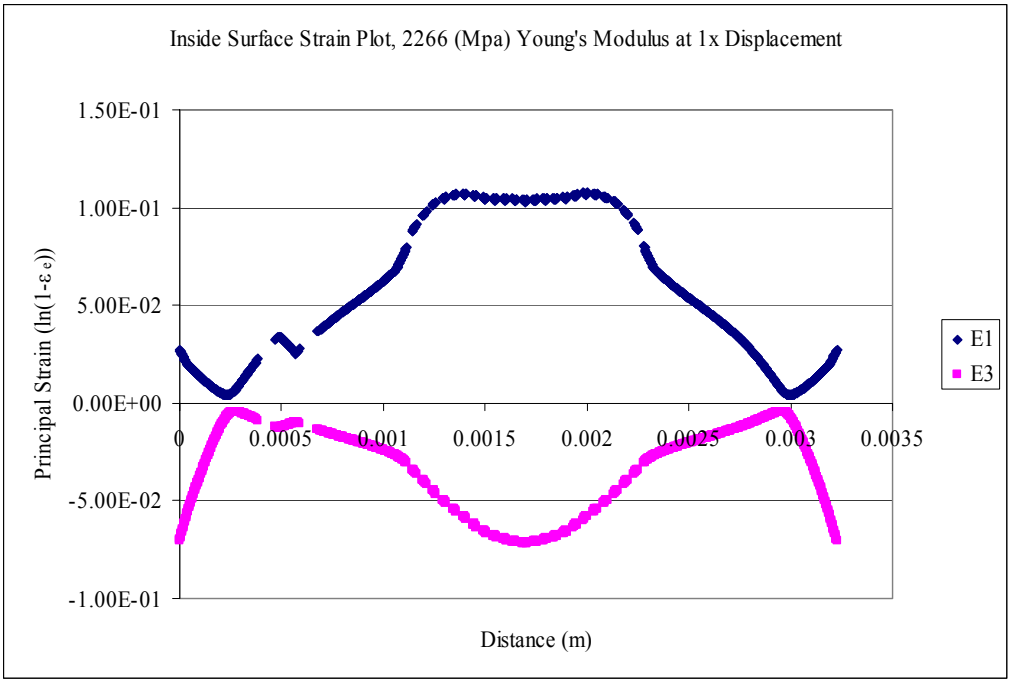

Fig. 3.27 Inside Surface Path Principal Strain E1, E3 for Case 4

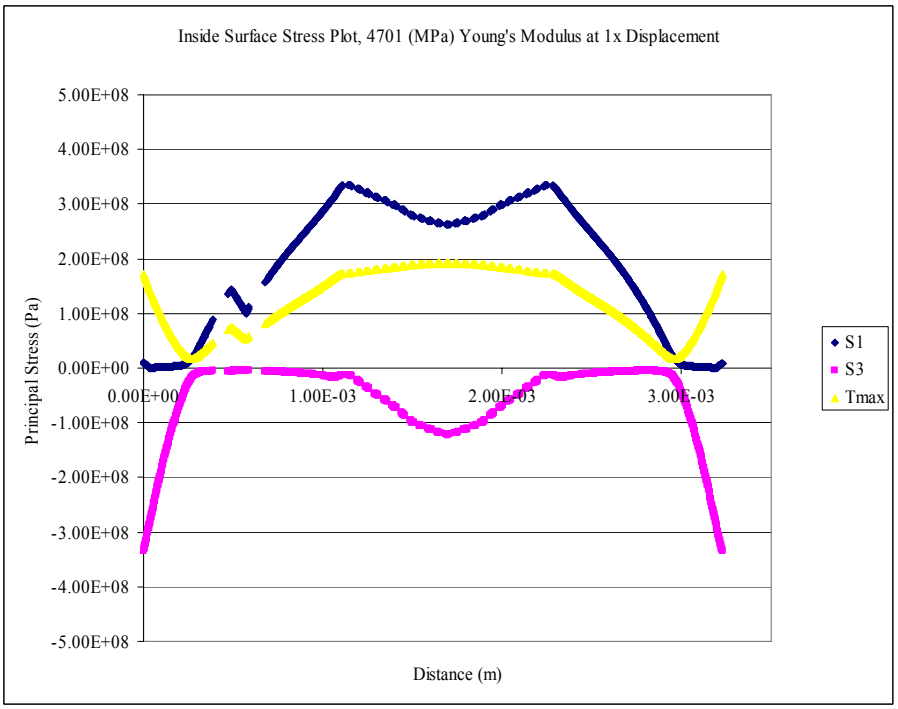

Fig. 3.28 Inside Surface Path Principal Stress S1, S3, and Tmax for Case 2

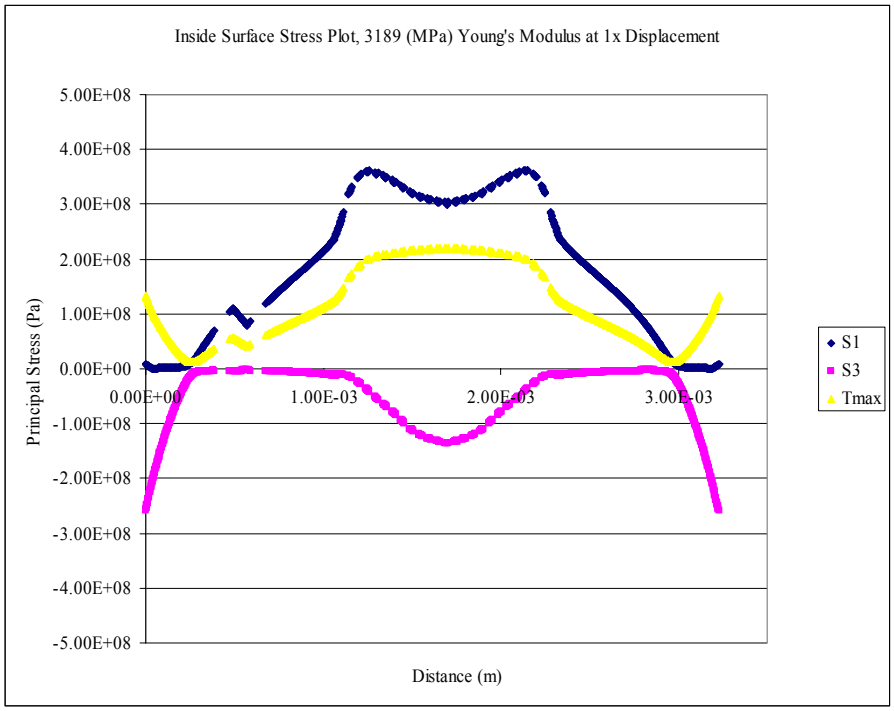

Fig. 3.29 Inside Surface Path Principal Stress S1, S3, and Tmax for Case 3

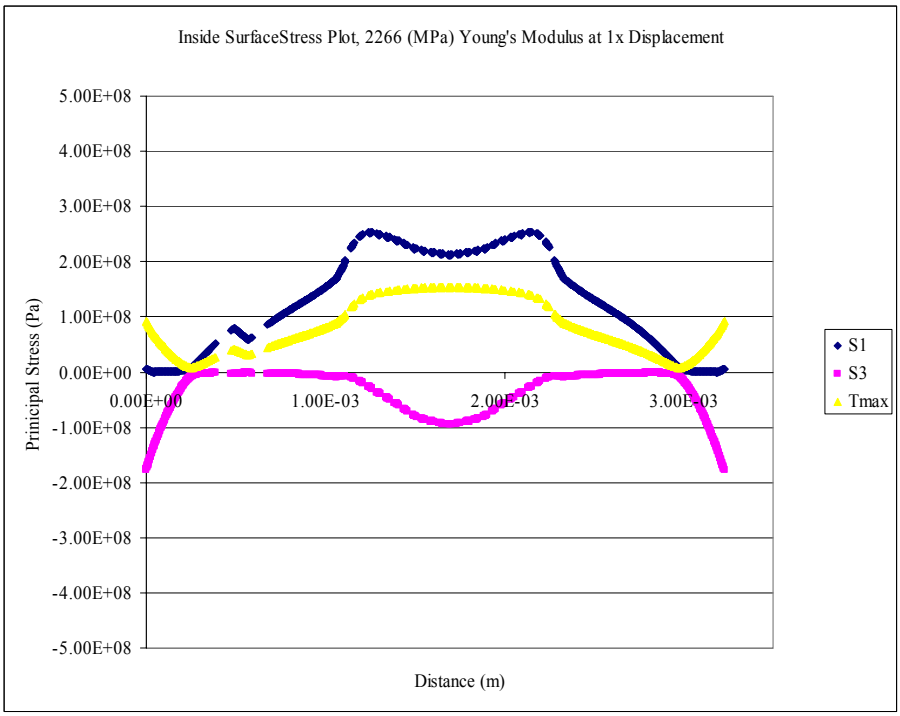

Fig. 3.30 Inside Surface Path Principal Stress S1, S3, and Tmax for Case 4

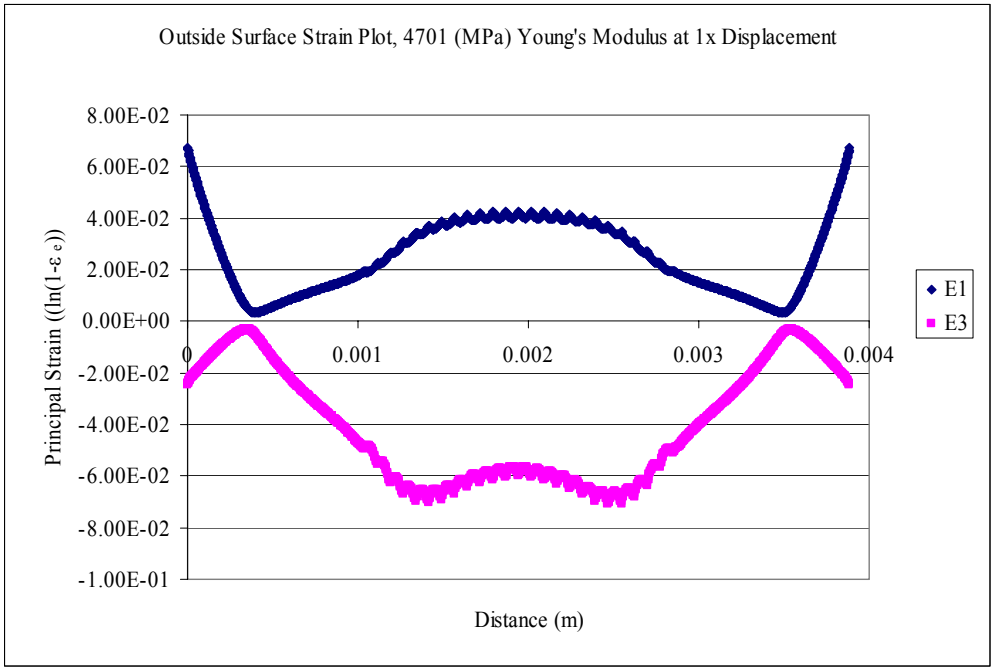

Fig. 3.31 Outside Surface Path Principal Strain E1, E3 for Case 2

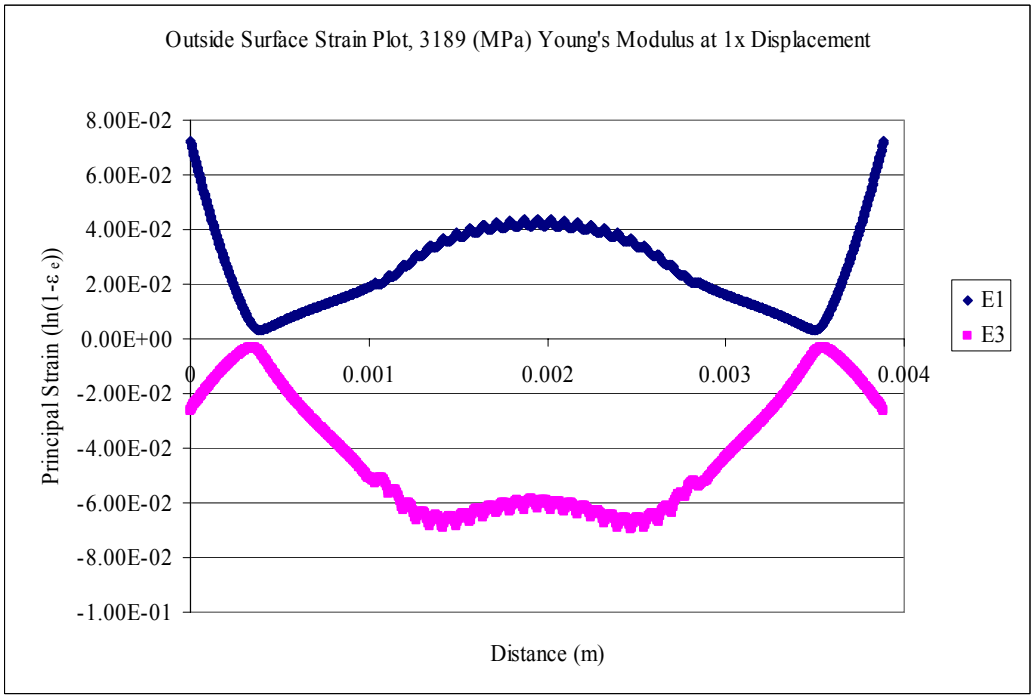

Fig. 3.32 Outside Surface Path Principal Strain E1, E3 for Case 3

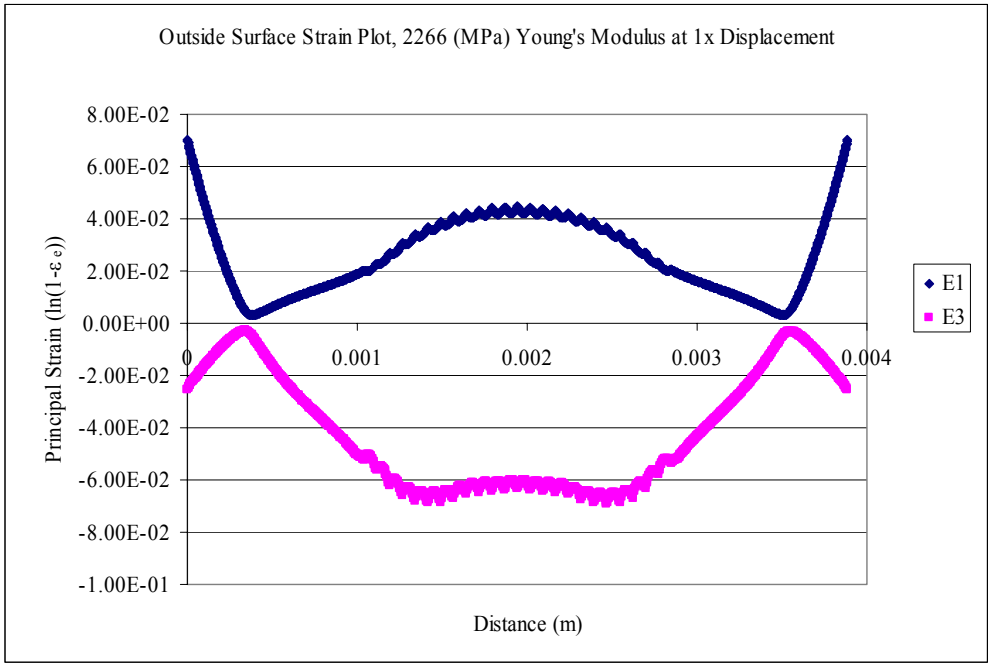

Fig. 3.33 Outside Surface Path Principal Strain E1, E3 for Case 4

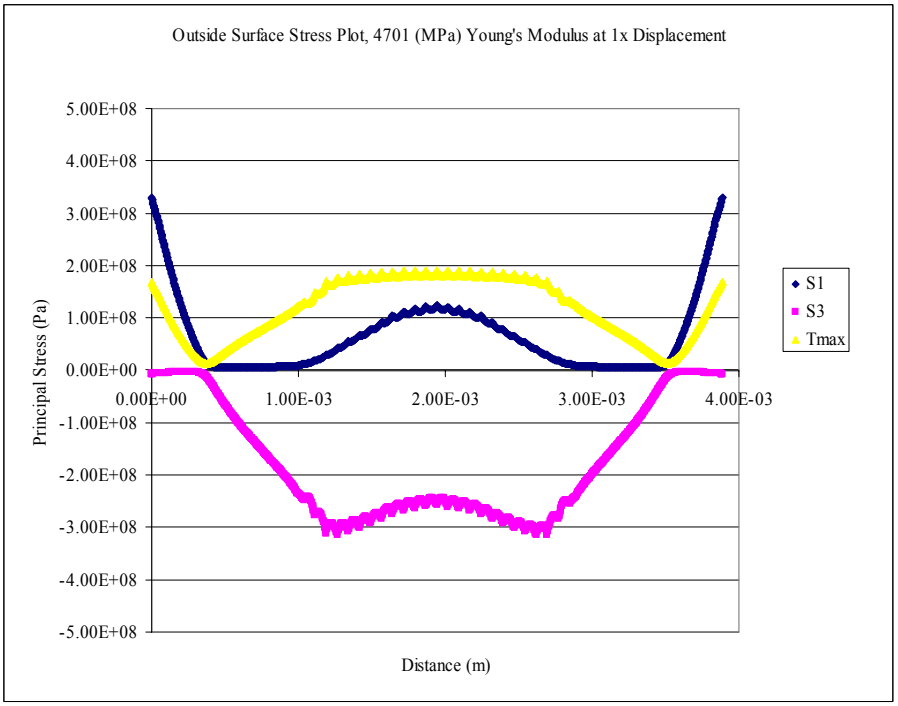

Fig. 3.34 Outside Surface Path Principal Stress S1, S3, and Tmax for Case 2

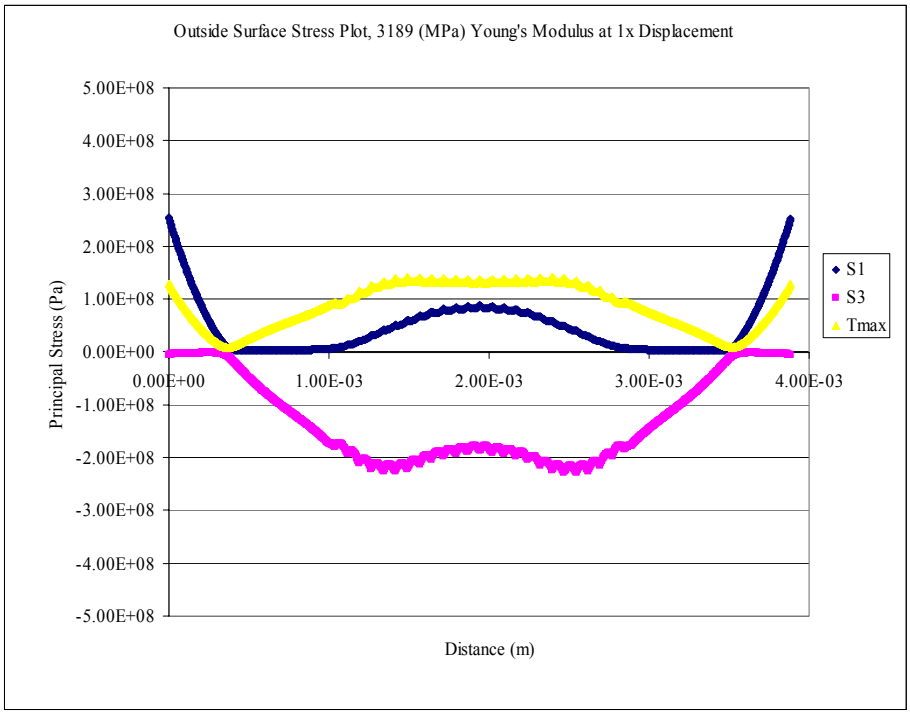

Fig. 3.35 Outside Surface Path Principal Stress S1, S3, and Tmax for Case 3

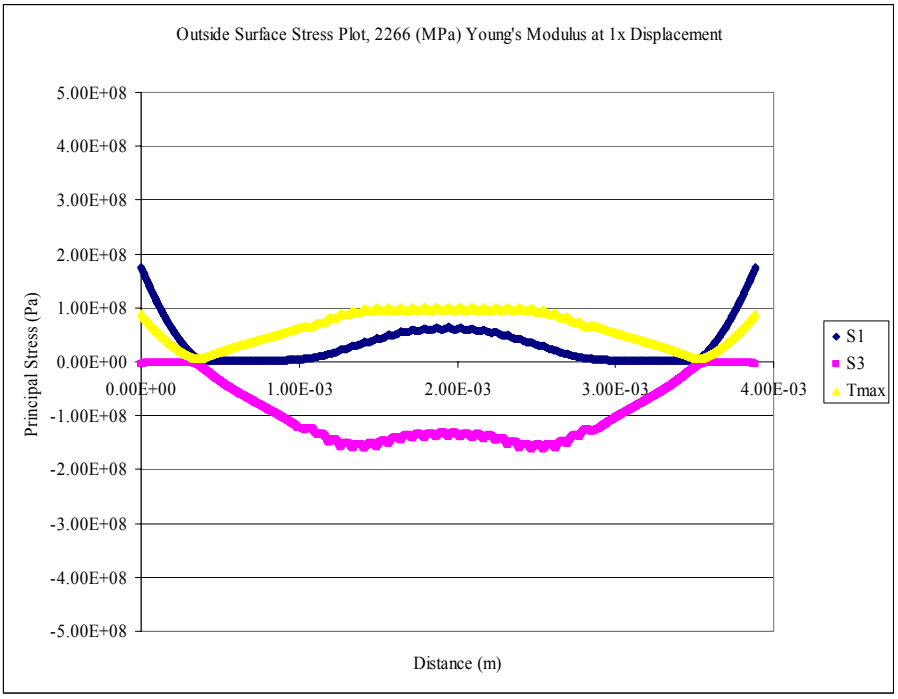

Fig. 3.36 Outside Surface Path Principal Stress S1, S3, and Tmax for Case 4

Fig. 3.37 illustrates the effect of Young's modulus on strain distributions at the inside surface along the fiber stent. Fig. 3.38 illustrates the same for the outside surface along the fiber stent.

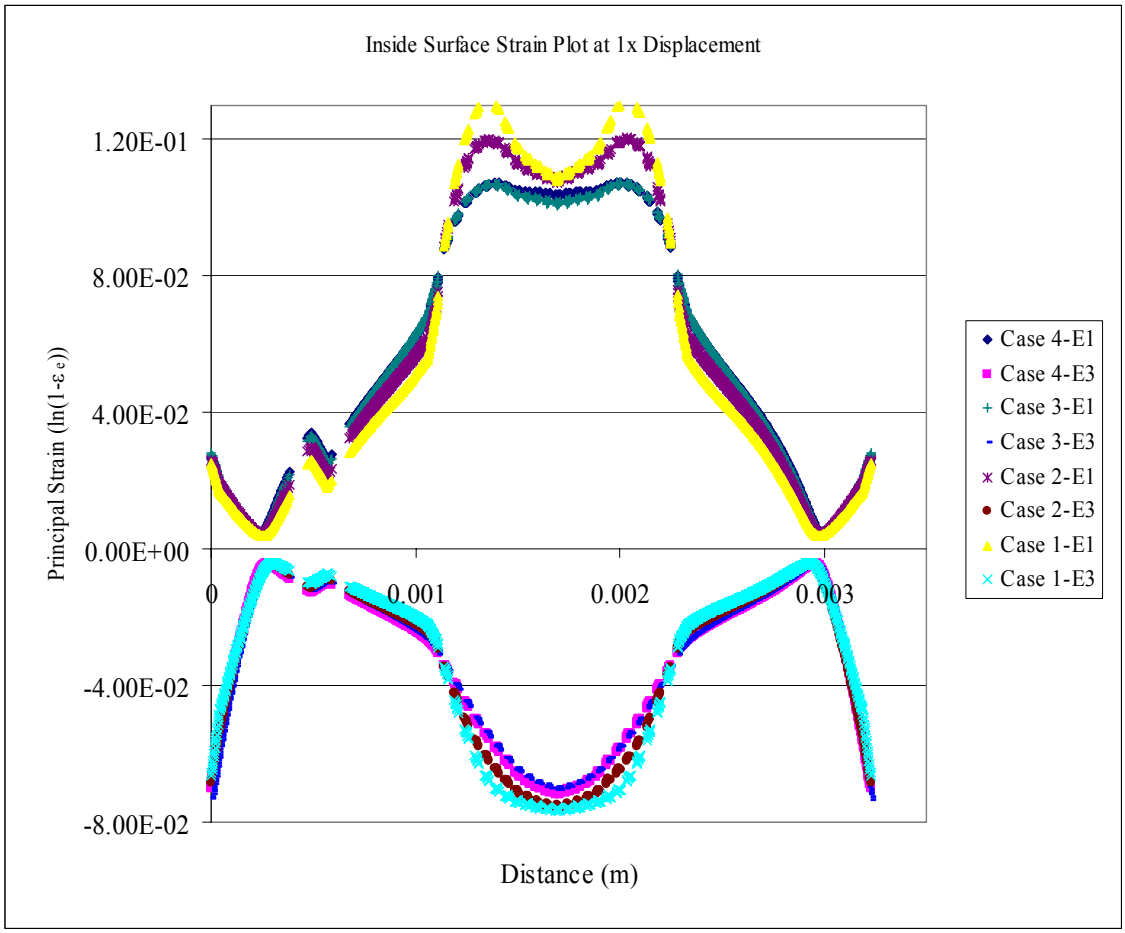

Fig. 3.37 Combined Young's Modulus Inside Surface Path Principal Strain E1, E3 Plot

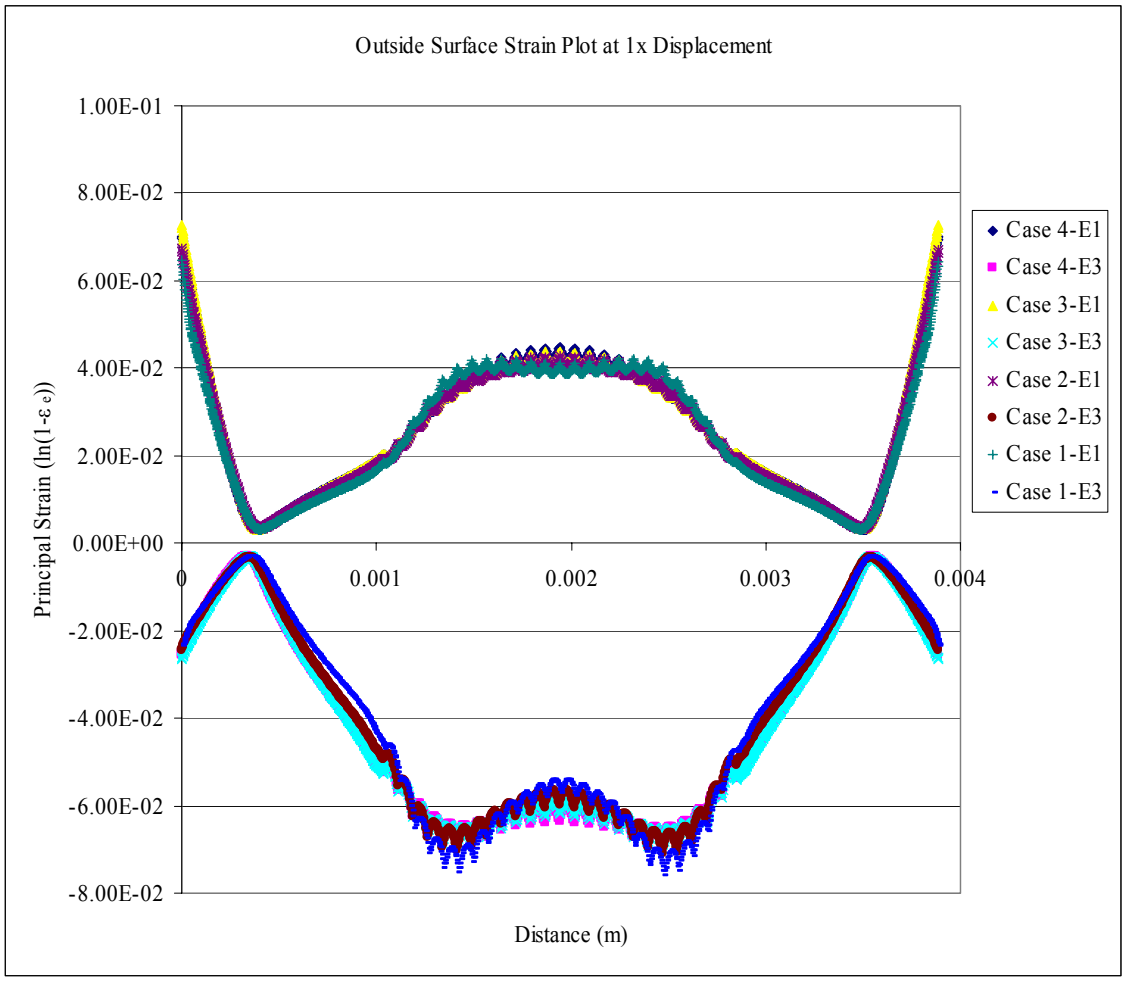

Fig. 3.38 Combined Young's Modulus Outside Surface Path Principal Strain E1, E3 Plot

3.2.3 Plastic Yielding of the Fiber for Case 1

3.2.3.1 Elastic Strain, Plastic Strain, Total Strain at 14(atm)

Plots of the fiber and cross sectional area of the fiber are captured to show the plastic strain yielding of the fiber in Fig. 3.39 and Fig. 3.42, and Fig. 3.40 shows the elastic regions of the fiber. Fig. 3.50 shows the total strain E1 distribution for the fiber.

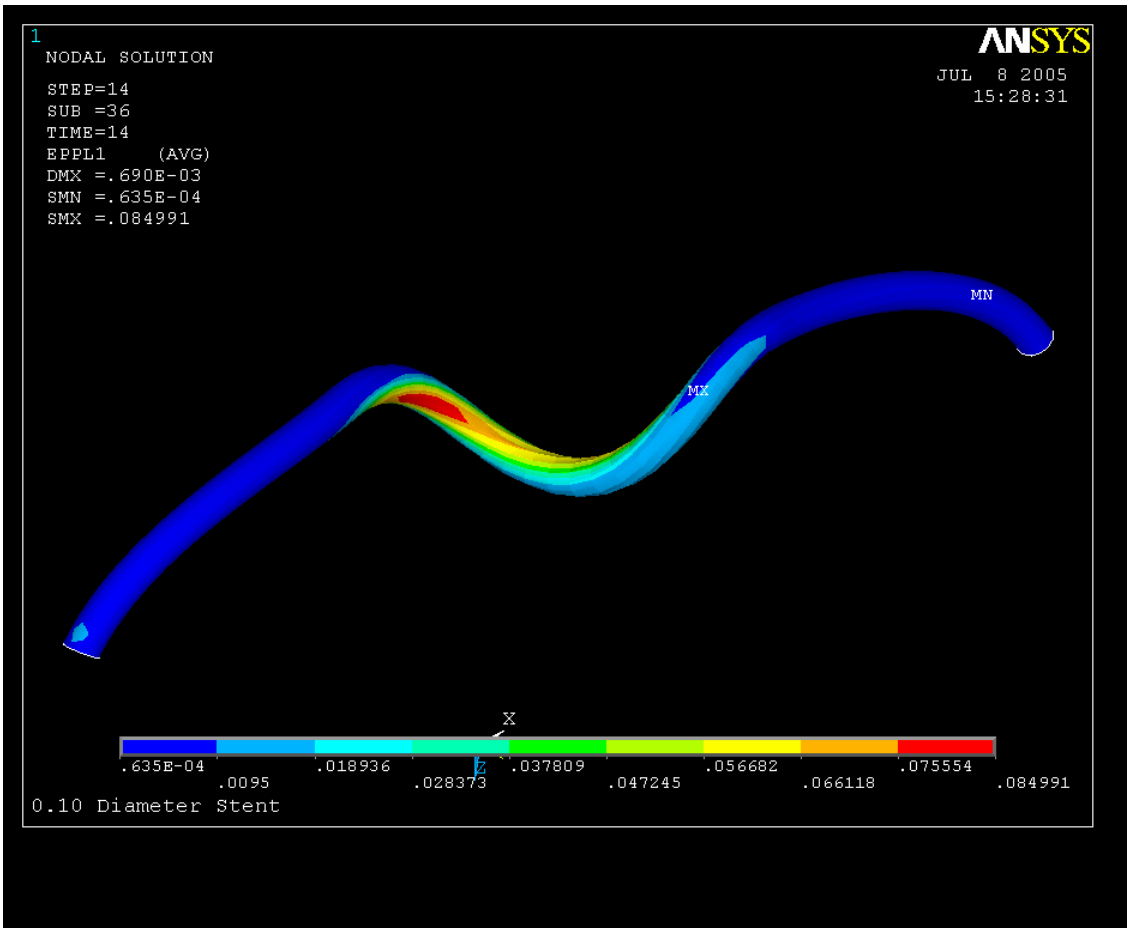

Fig. 3.39 Plastic Strain Contour Plot at 0.35 Poisson's Ratio, 14(atm)

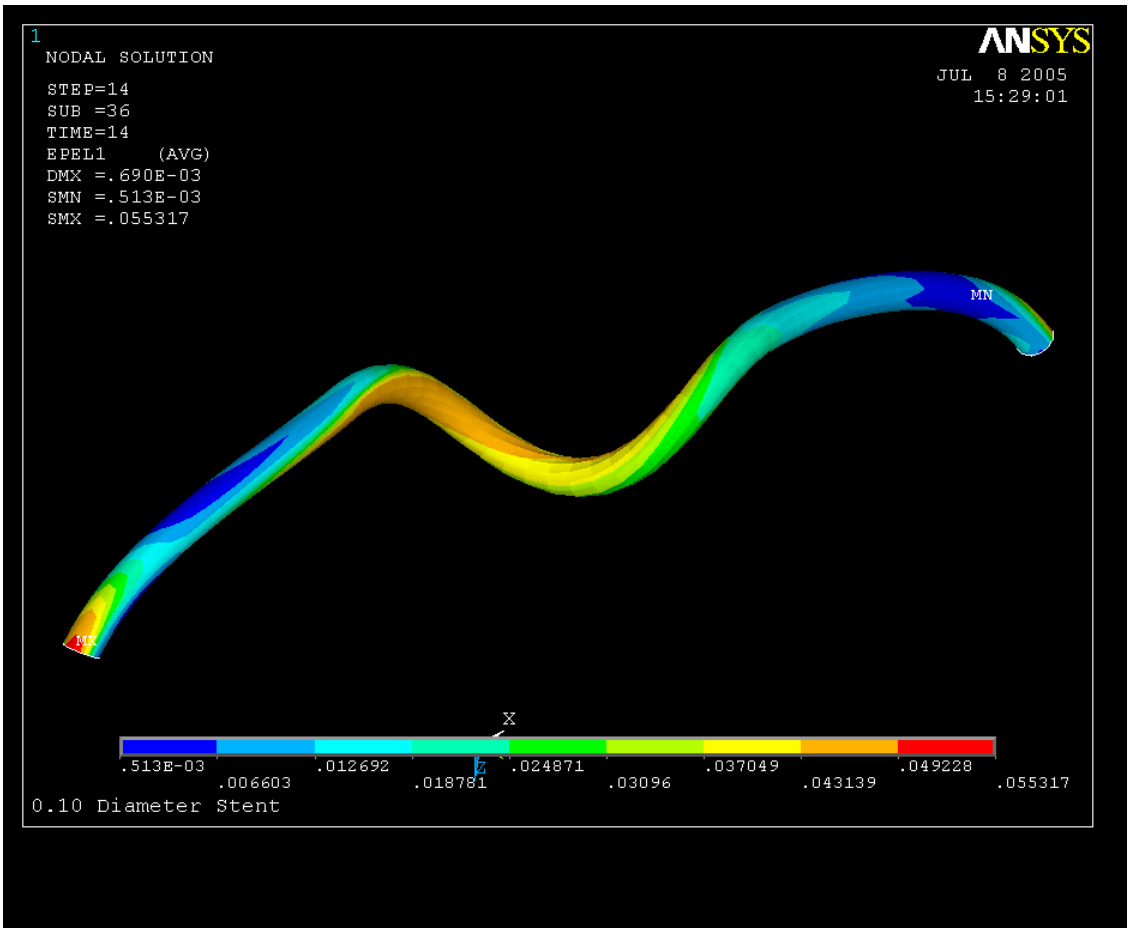

Fig. 3.40 Elastic Strain E1 Contour Plot at 0.35 Poisson's Ratio, 14(atm)

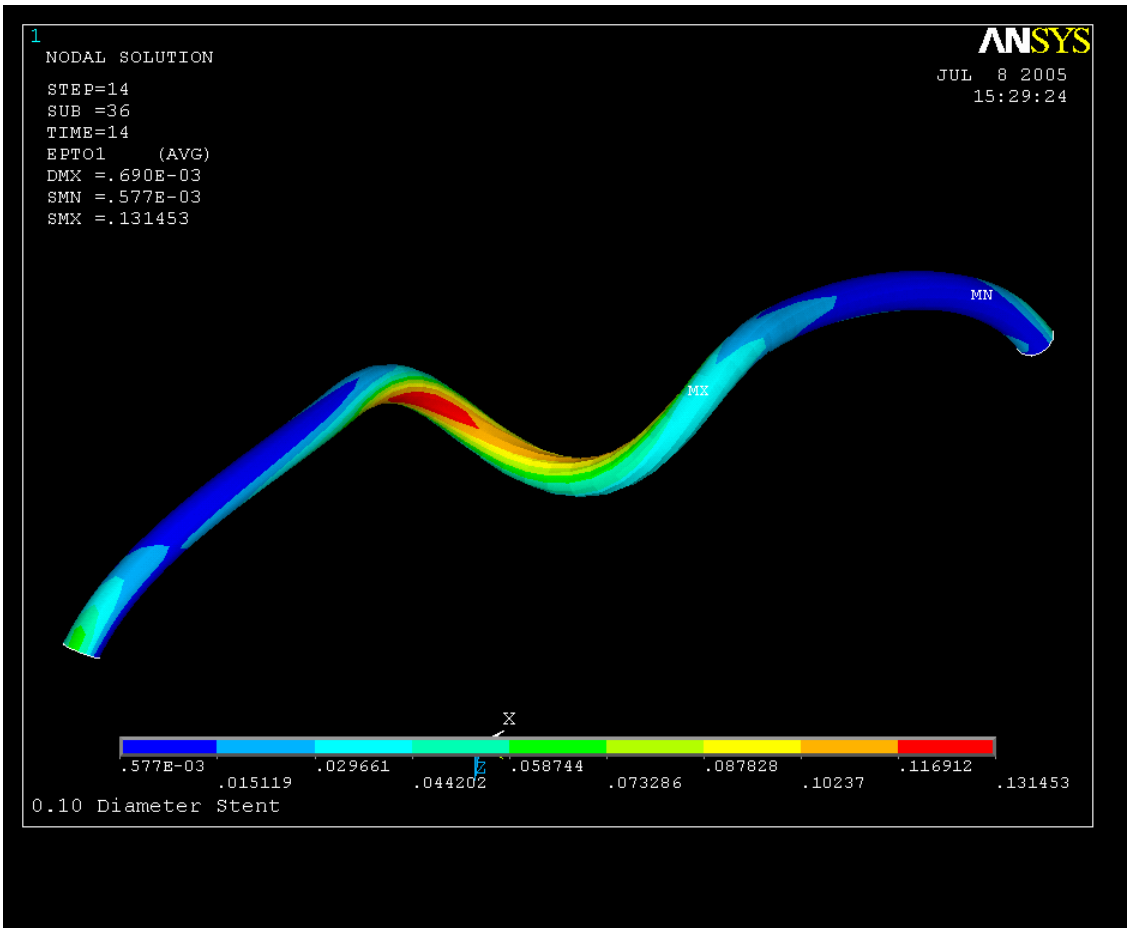

Fig. 3.41 Total Strain E1 Contour Plot at 0.35 Poisson's Ratio, 14(atm)

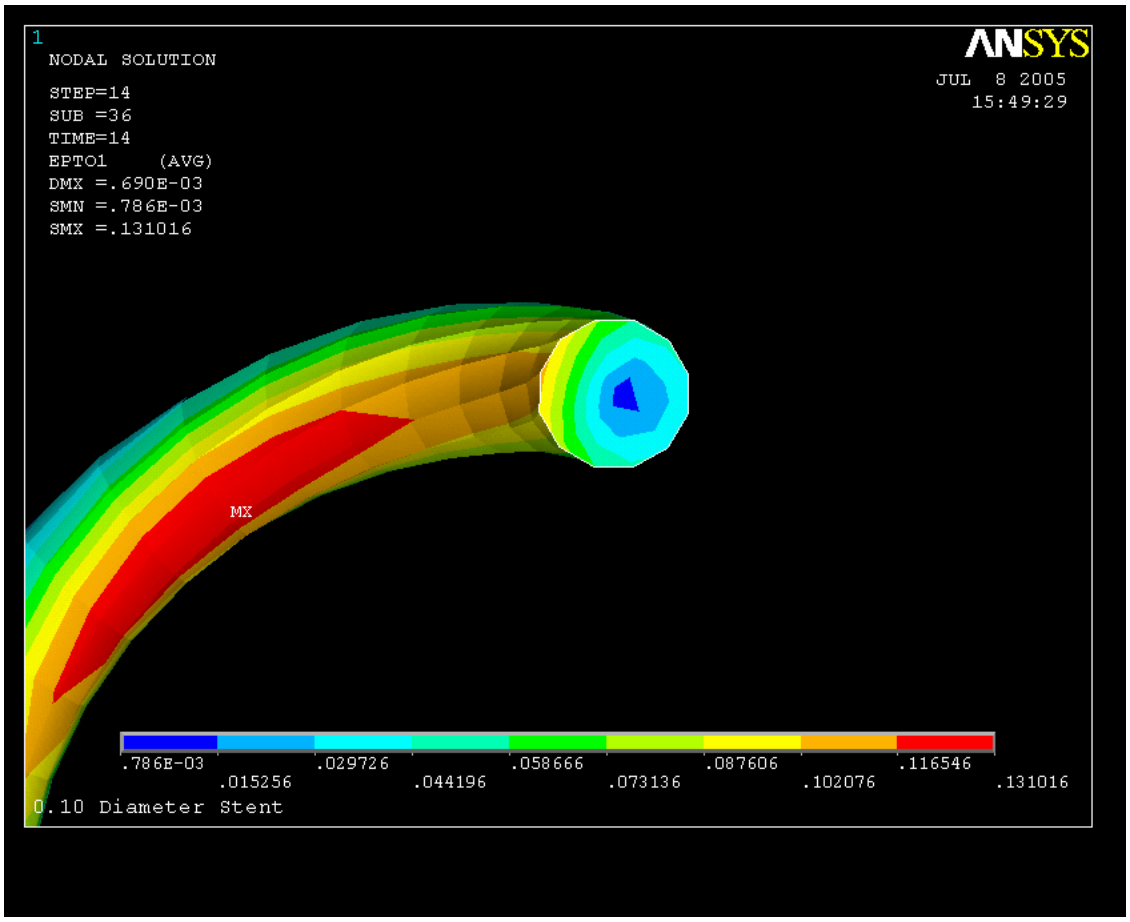

Fig. 3.42 Total Strain E1 Contour Plot at 0.35 Poisson's Ratio, 14(atm) of Cross Section PLLA Fiber

3.2.3.2 Yielding of the fiber based on von Mises Distortion Energy Criteria for Case 1

The von Mises Stresses are obtained from the simulation and shown in Fig. 3.43 at 1(atm), Fig. 3.44 at 7(atm), Fig. 3.45 at 14(atm). The von Mises Stresses of the cross sectional area of the small coil at its mid-section are shown at 1(atm), 7(atm), 10(atm) and 14(atm) in Fig. 3.46 – Fig. 3.49.

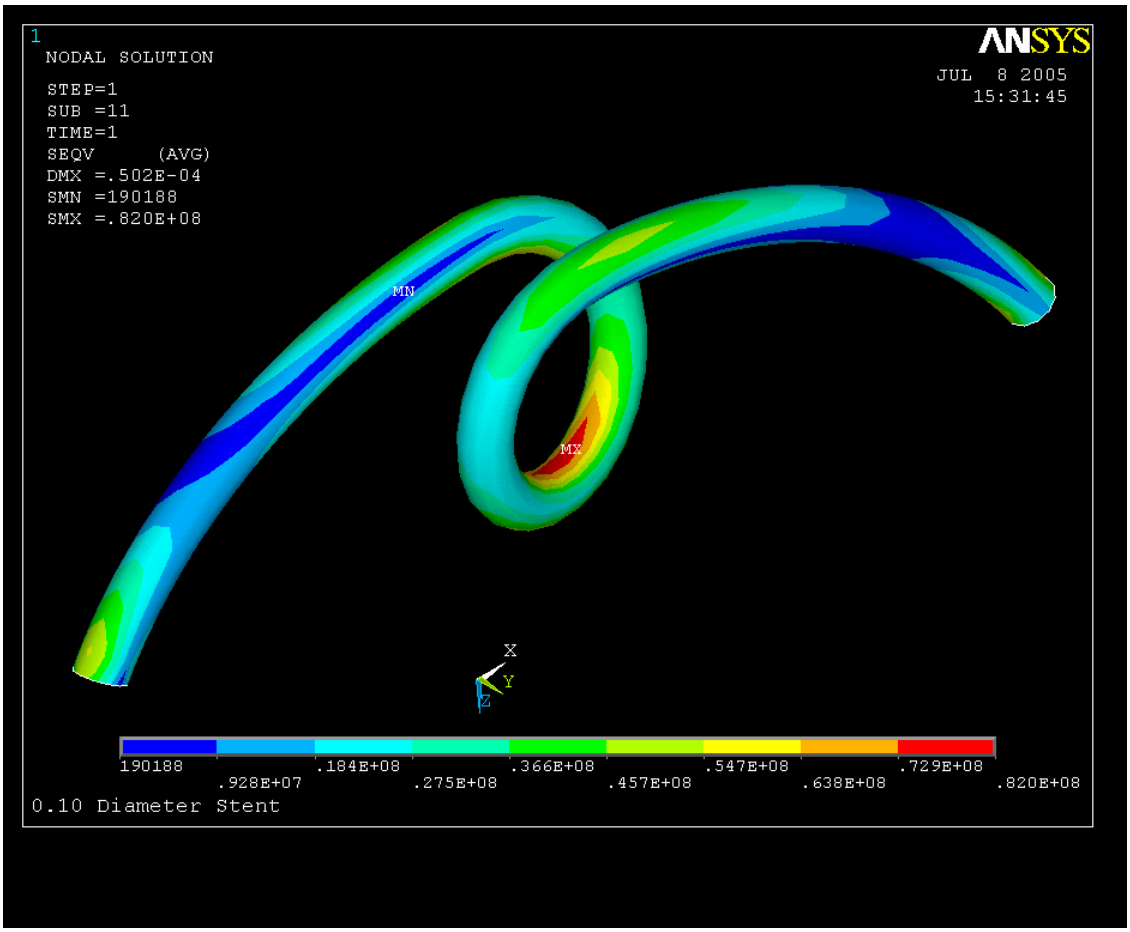

Fig. 3.43 Von Mises Stress Contour Plot at 0.35 Poisson's Ratio, 1(atm)

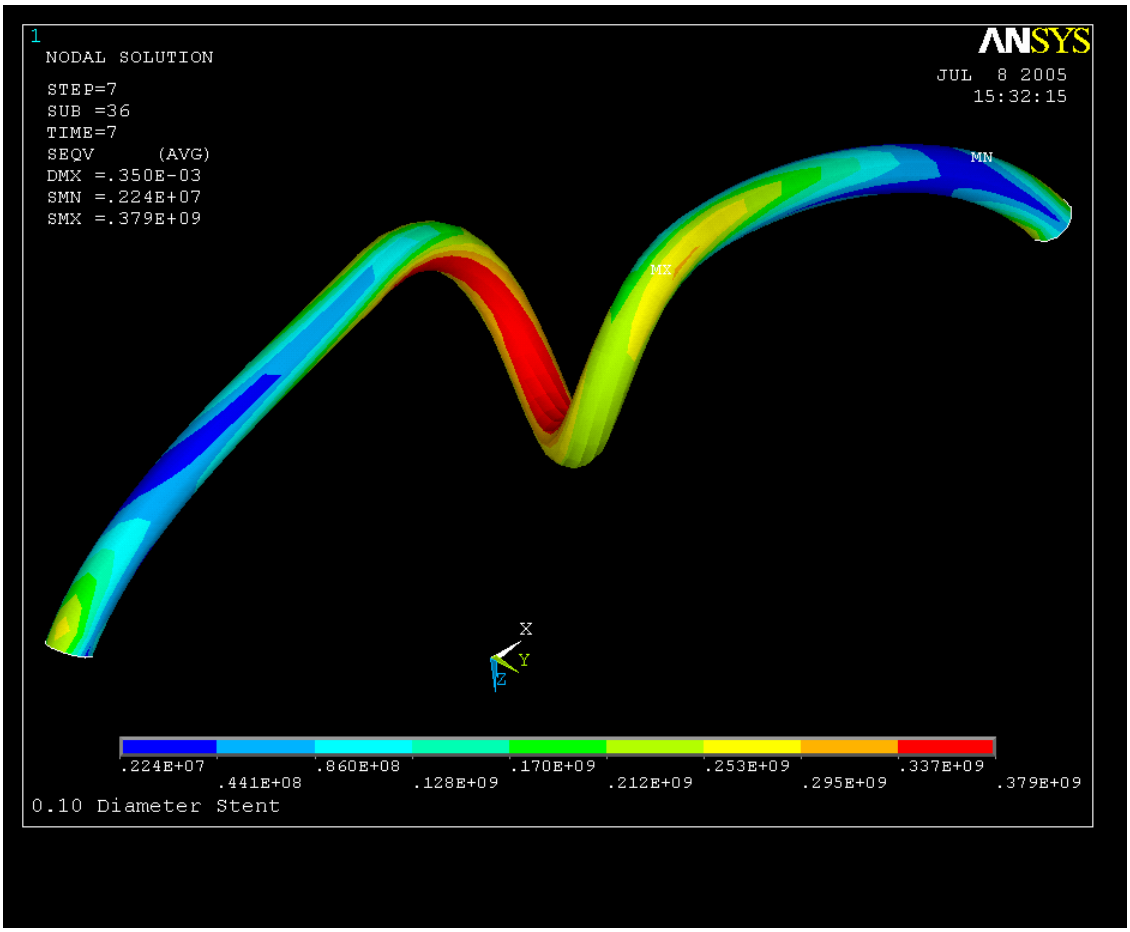

Fig. 3.44 Von Mises Stress Contour Plot at 0.35 Poisson's Ratio, 7(atm)

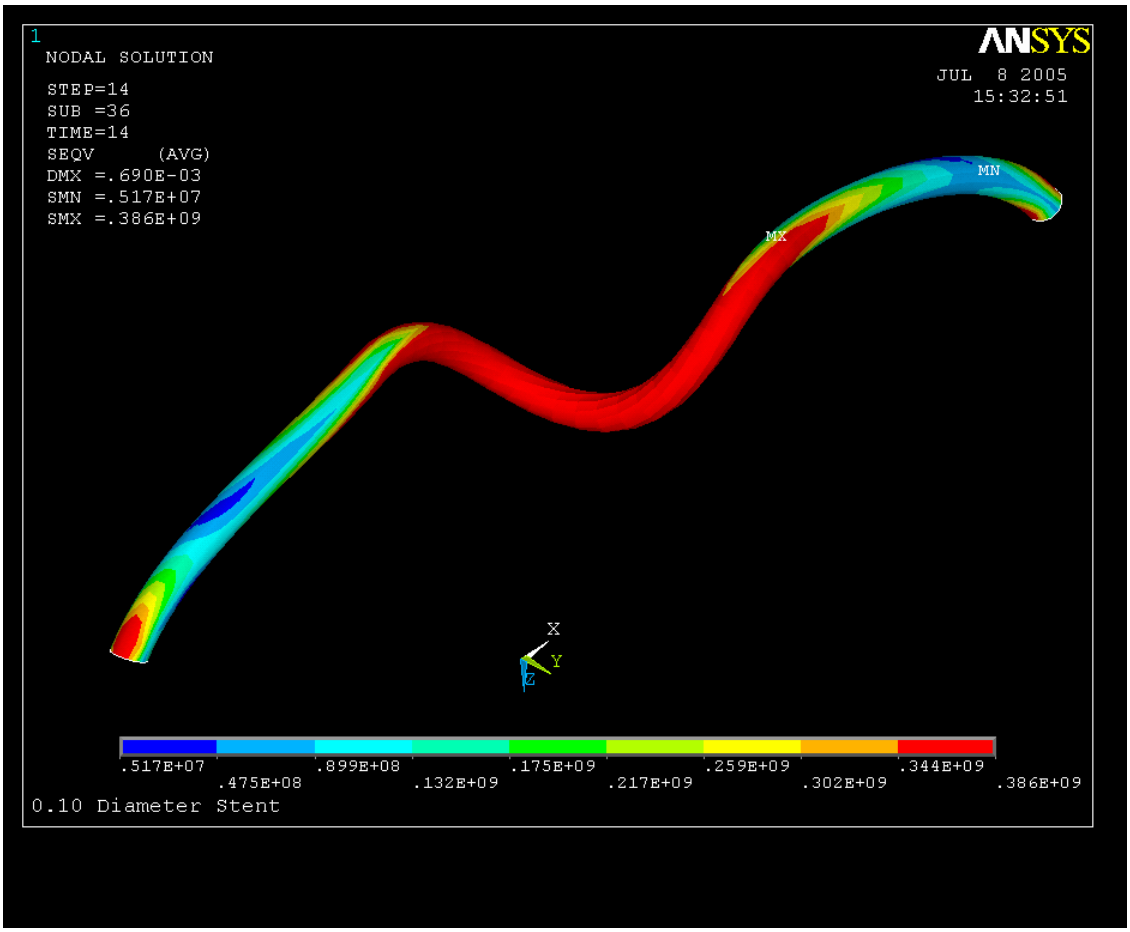

Fig. 3.45 Von Mises Stress Contour Plot at 0.35 Poisson's Ratio, 14(atm)

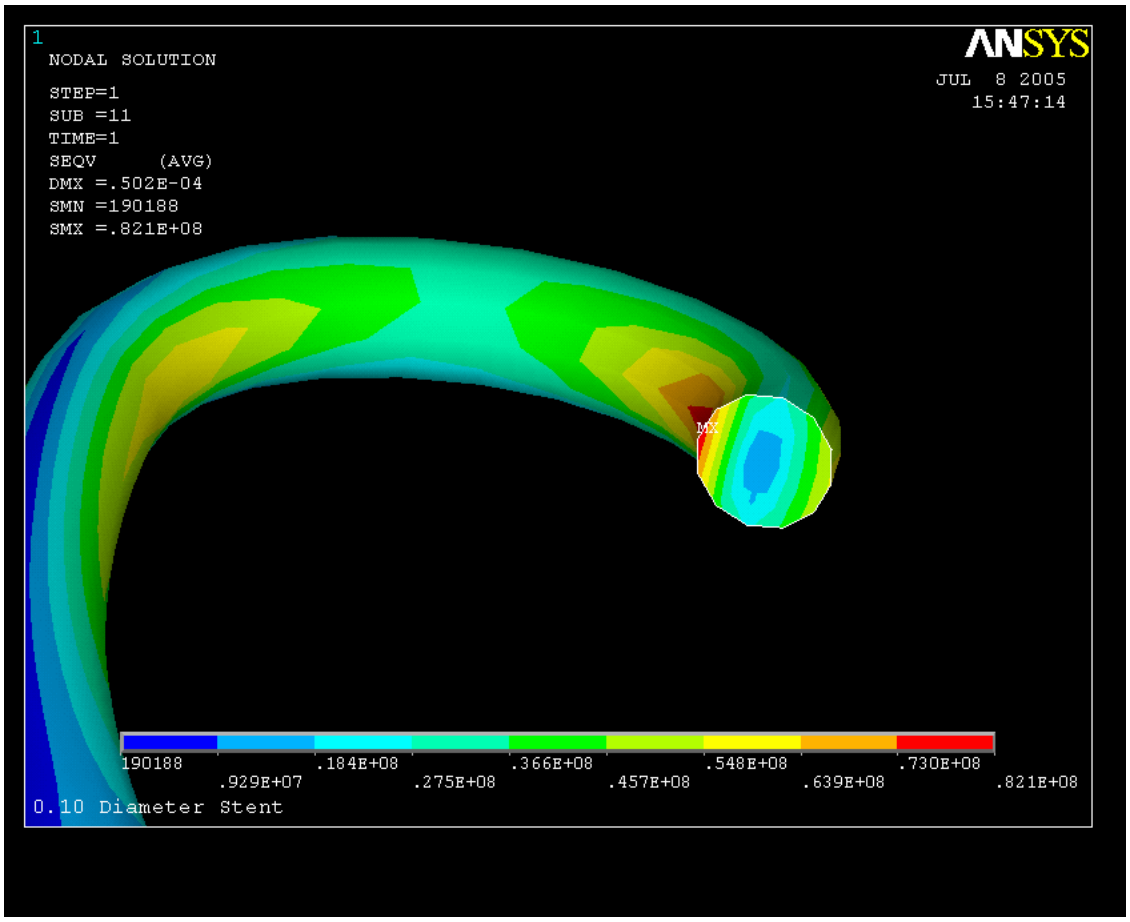

Fig. 3.46 Von Mises Stress Contour Plot at 0.35 Poisson's Ratio, 1(atm) of Cross Section PLLA Fiber

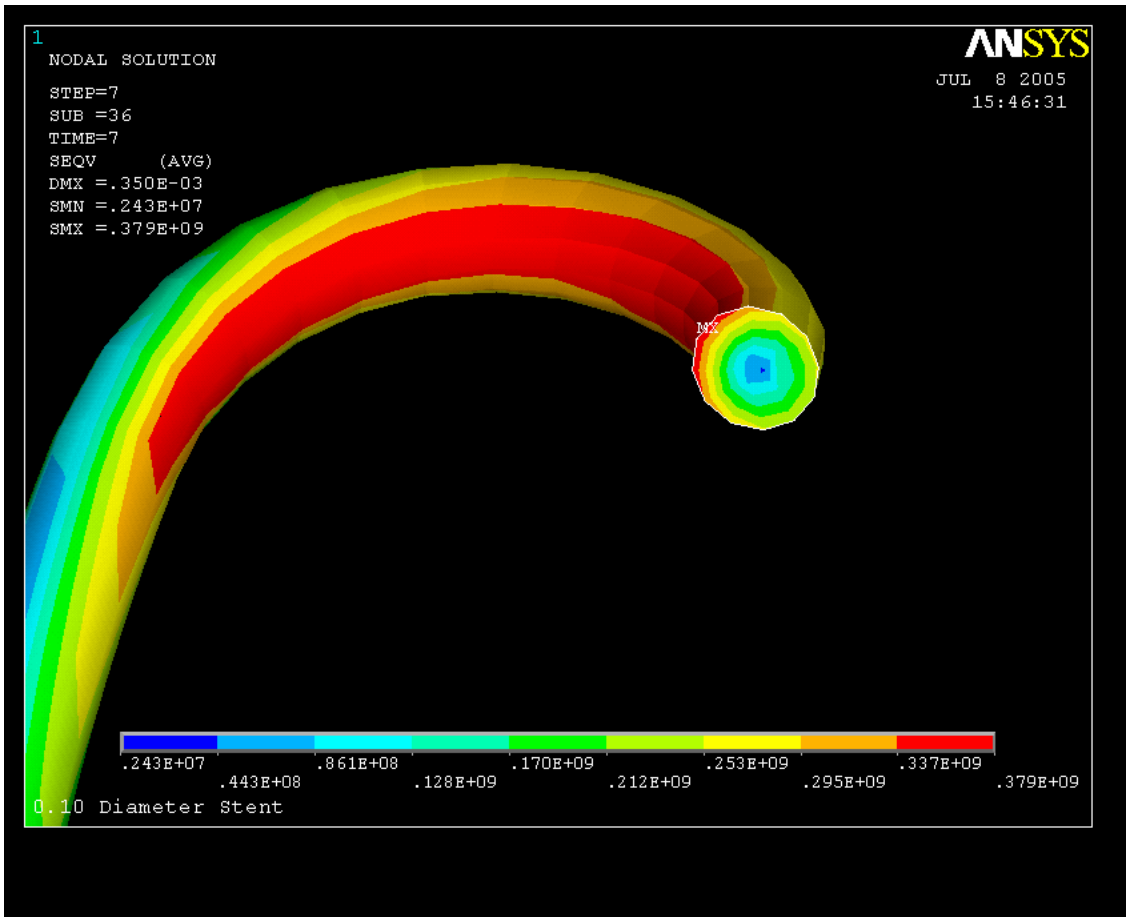

Fig. 3.47 Von Mises Stress Contour Plot at 0.35 Poisson's Ratio, 7(atm) of Cross Section PLLA Fiber

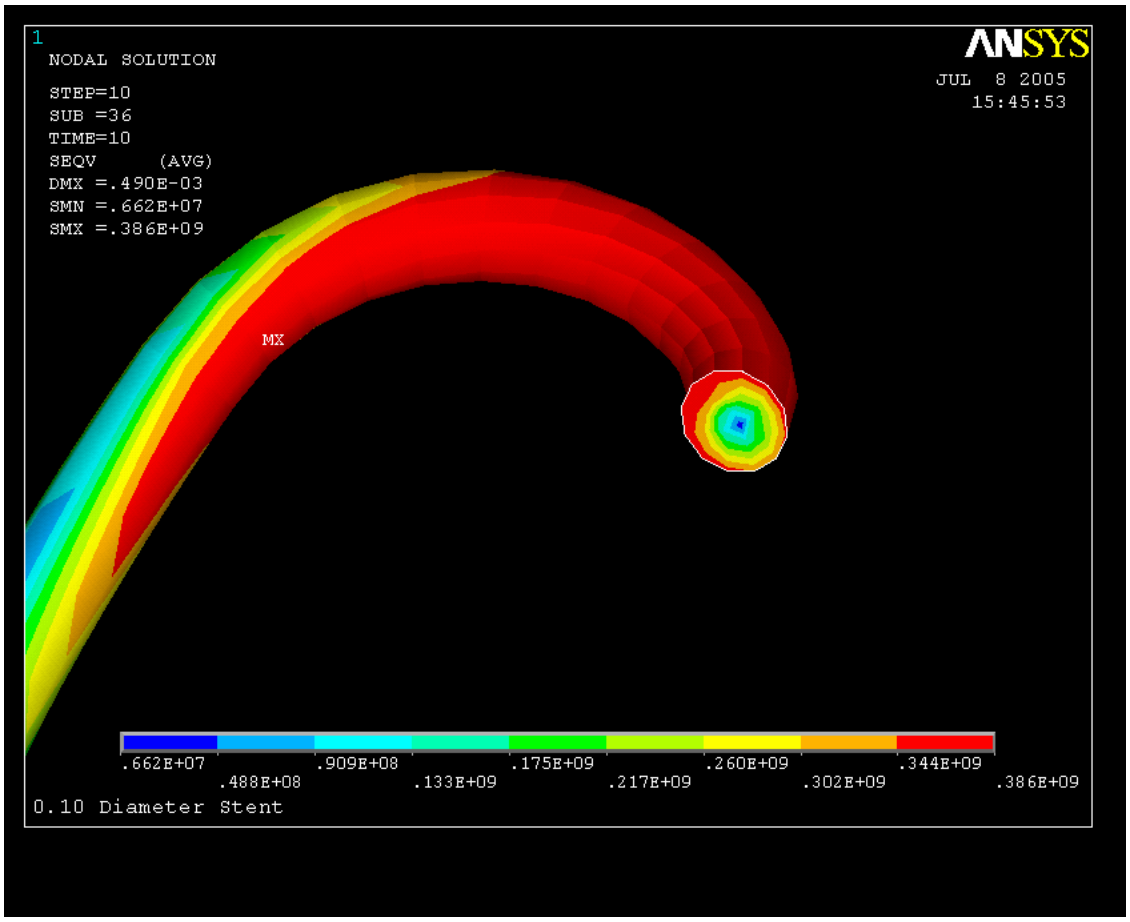

Fig. 3.48 Von Mises Stress Contour Plot at 0.35 Poisson's Ratio, 10(atm) of Cross Section PLLA Fiber

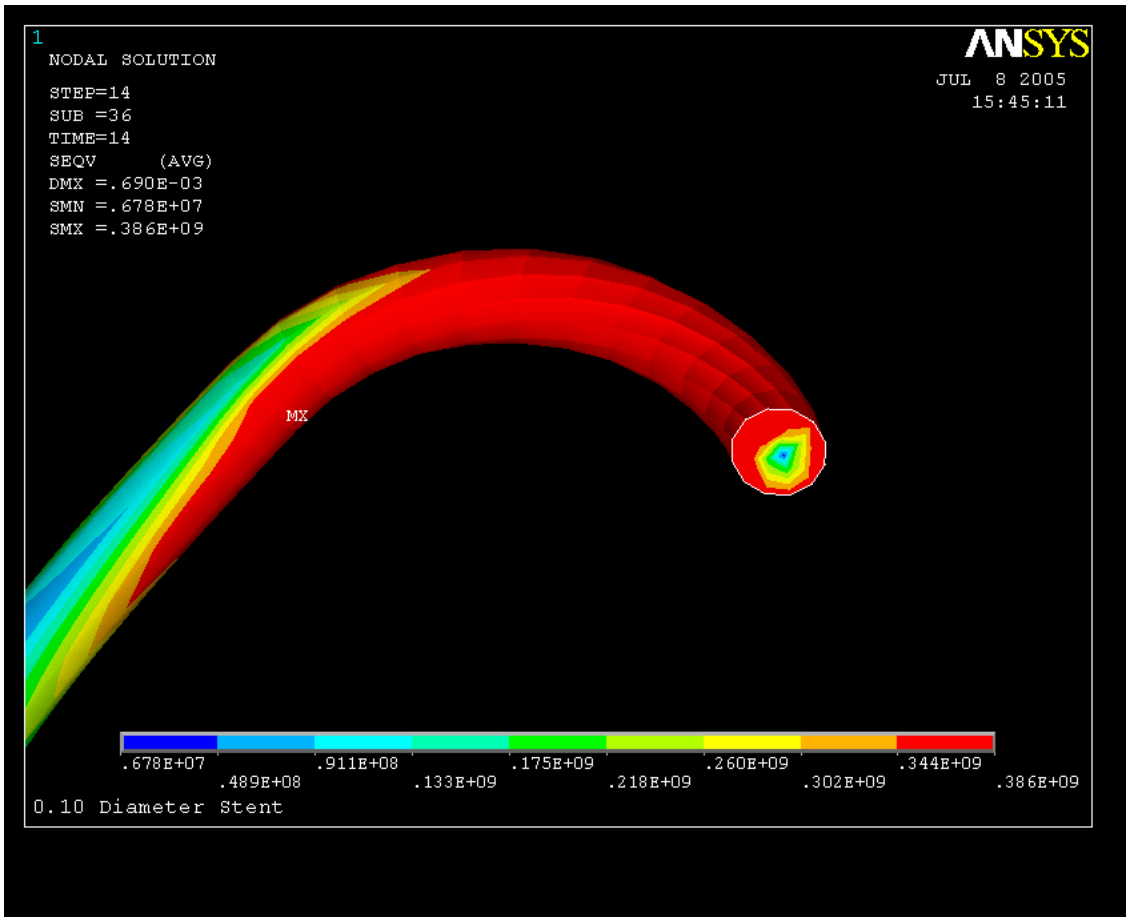

Fig. 3.49 Von Mises Stress Contour Plot at 0.35 Poisson's Ratio, 14(atm) of Cross Section PLLA Fiber

3.2.4 Effects of Poisson's Ratio

The effect of Poisson's Ratio determines the compressibility of the material. The four different Young's Moduli are analyzed at different Poisson's ratio values at 1x displacement. First, Poisson's ratio is set at a value of 0.4999. The principal stresses and principal strains are shown in Appendix B for the inside surface and the outside surface for the four different case studies. The strain plots are combined in Fig. 3.50 and Fig. 3.51.

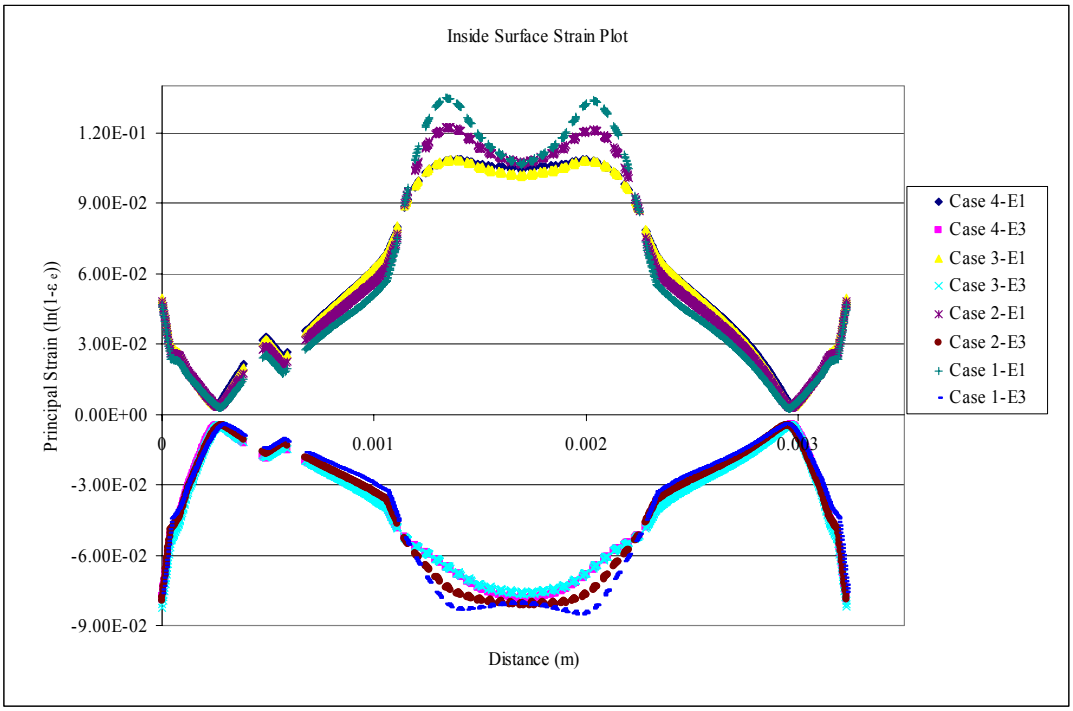

Fig. 3.50 Combined Young's Modulus Inside Surface Path Principal Strain E1, E3 Plot

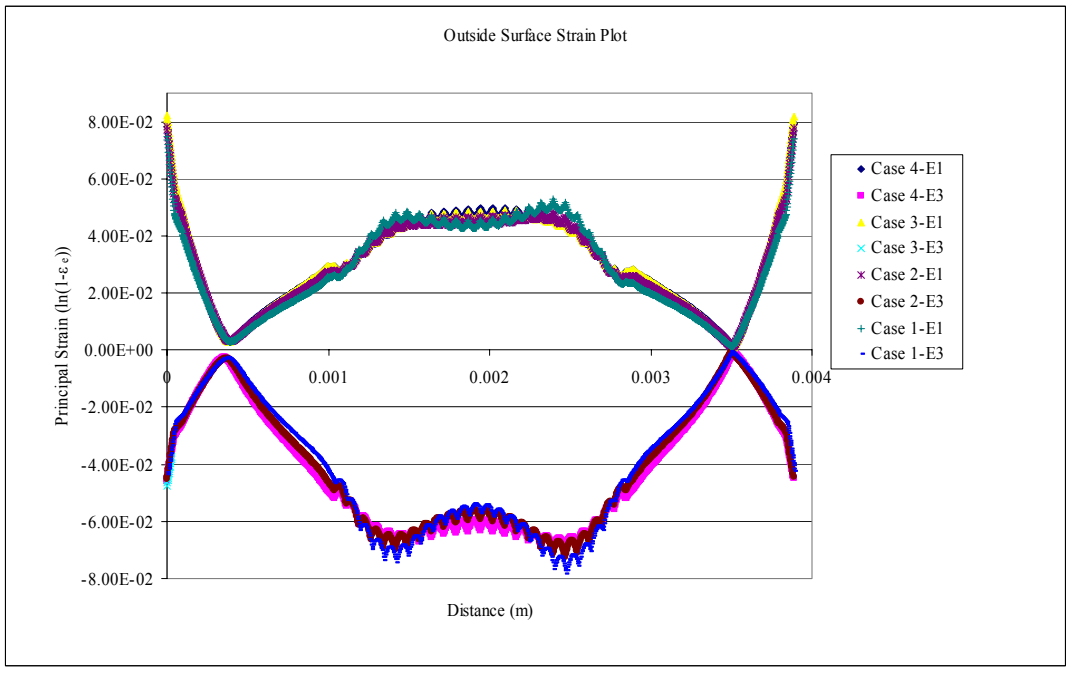

Fig. 3.51 Combined Young's Modulus Outside Surface Path Principal Strain E1, E3 Plot

The vector plots of the principal stresses, von Mises contour plots, and the plastic and elastic contour plots are shown in Appendix B.

3.2.5 Effects of Young's Modulus on Maximum Shear Stress

In the compressible state the displacement is used at 1x only and the outside surface and inside surface maximum shear stresses are calculated as shown Table 3.4 and in Fig. 3.52.

Table 3.4 Maximum Shear Stress at different Displacements with 0.35 Poisson's Ratio

Young's Modulus (MPa)	Inside Surface Maximum Shear Stress (MPa)	Outside Surface Maximum Shear Stress (MPa)
2266 (Case 4)	1.54E+02	1.02E+02
3189 (Case 3)	2.20E+02	1.42E+02
4701 (Case 2)	1.93E+02	1.91E+02
7043 (Case 1)	2.18E+02	2.17E+02

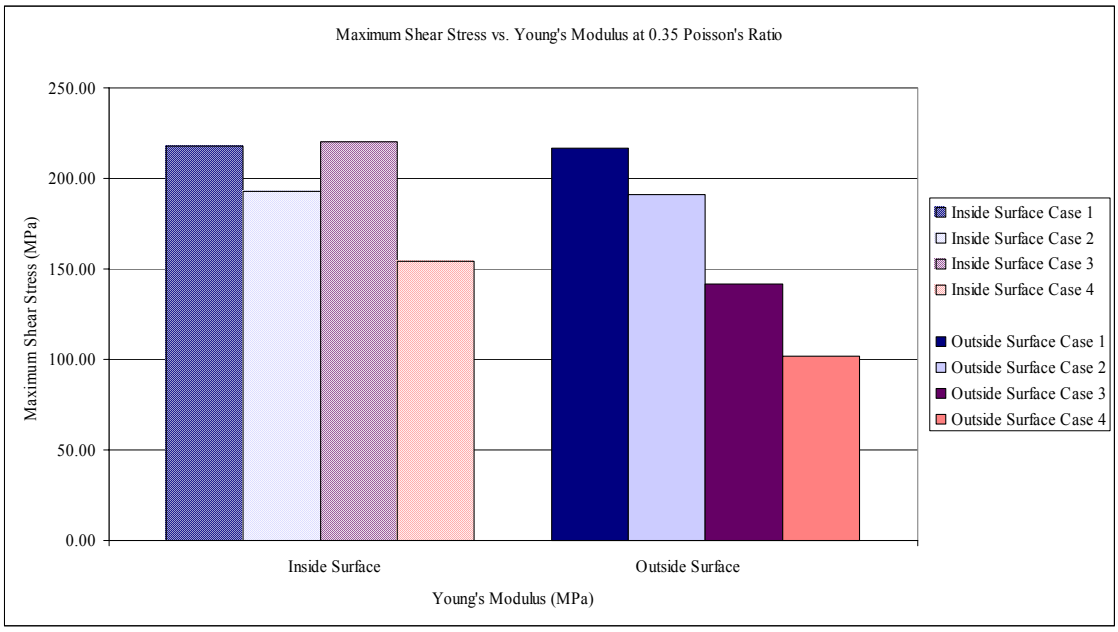

Fig. 3.52 Maximum Stress Bar Graph for Different Young's Modulus for 0.35 Poisson's Ratio

3.2.6 Effects of Axial Displacement

The different boundary conditions applied to the different Young's Moduli are simulated at 1x the axial displacement values taken from the verification data and then at 2x the axial displacement values and finally at 3x the axial displacement values for the incompressible state. The results are shown in Fig. 3.53 and Table 3.5.

Table 3.5 Maximum Shear Stress at different Displacements with 0.4999 Poisson's Ratio

Young's Modulus (MPa)	Inside Surface Maximum Shear Stress (MPa)			Outside Surface Maximum Shear Stress (MPa)		
	1x	2x	3x	1x	2x	3x
2166 (Case 4)	1.46E+02	1.46E+02	1.48E+02	9.94E+01	1.00E+02	1.01E+02
3189 (Case 3)	2.17E+02	2.16E+02	2.01E+02	1.39E+02	1.39E+02	1.40E+02
4701 (Case 2)	1.91E+02	1.91E+02	1.91E+02	1.89E+02	1.89E+02	1.89E+02
7043 (Case 1)	2.16E+02	2.16E+02	2.16E+02	2.16E+02	2.16E+02	2.16E+02

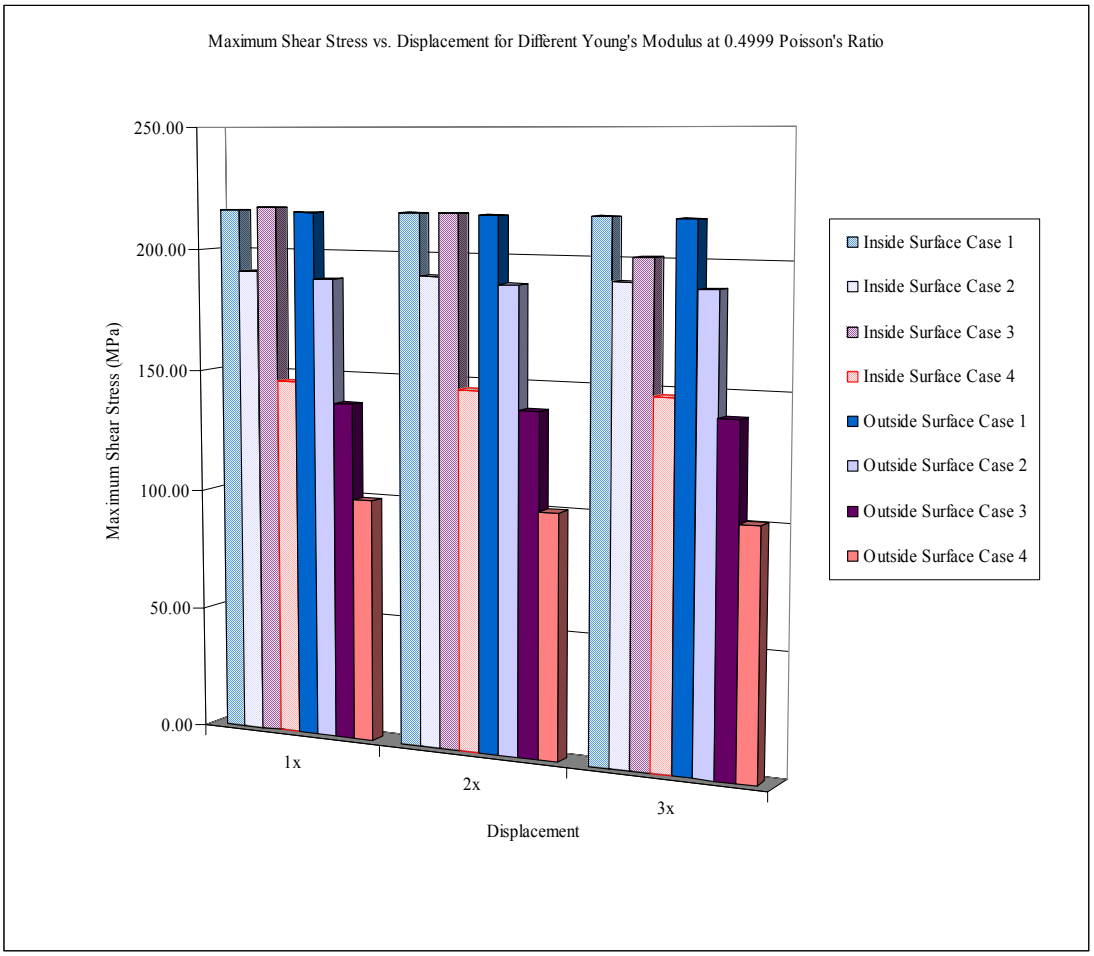

Fig. 3.53 Maximum Stress 3-D Bar Graph for Different Young's Modulus at different Displacements for 0.4999 Poisson's Ratio

CHAPTER 4

DISCUSSION

4.1 Model Validation

The experimental balloon expansion data and FEM simulation results for Poisson's ratio of 0.35 are shown in Fig. 4.1.

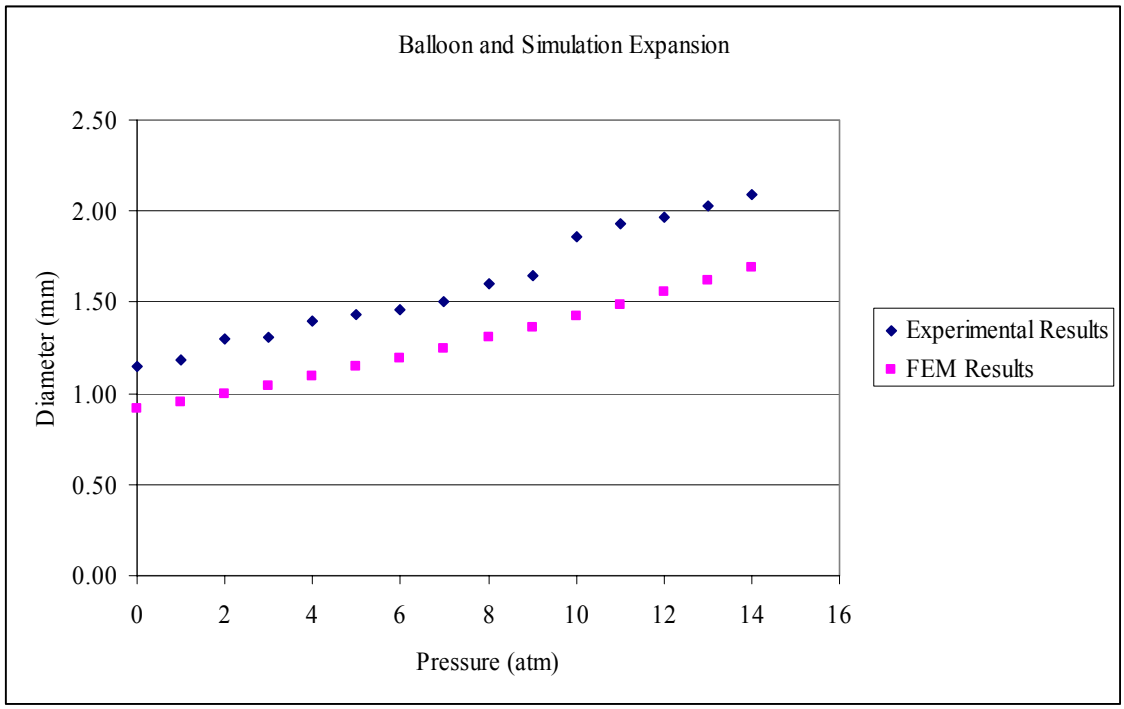

Fig. 4.1 Experimental Balloon and FEM Simulation Diameter Results

The diameter change due to the pressure change is compared to the experimental and FEM simulation results. The assumption for the simulation is the pressure acting on the stent begins at zero atmospheres. However, the pressure exerted by the expanding balloon on the stent is not zero when they first contact each other.

This initial pressure plus the incrementing pressure cause the deformation of the stent. The simulation results show the incrementing pressure only. The experimental simulation data shows a higher response than the FEM simulation in Fig. 4.1. This is due to the model being an ideal manufactured coil stent. Holding the dimensions for the diameter of the stent is extremely difficult for the manufacturing of the coils. Another cause for the difference in the simulation and experimental results is the assembling of the coil stent onto the catheter can cause the PLLA internal fiber coils to move axially along the balloon. This can cause the stent's internal coils to deform into a higher pitch resulting in the coil stent expanding more in the radial direction.

The data is normalized to understand the difference in the diameters at the increasing pressure load and the slope of the simulation results and the experimental results as shown in Fig. 4.2. The experimental and simulation responses are both close to being linear. Normalizing the data shows both plots overlapping onto each other at each pressure increment. This normalized data shows good agreement of the diameter change with the pressure increment in the balloon between the experimental and simulation results. This in effect shows the overall compliance of the stent diameter change with the pressure loading validating the simulation results.

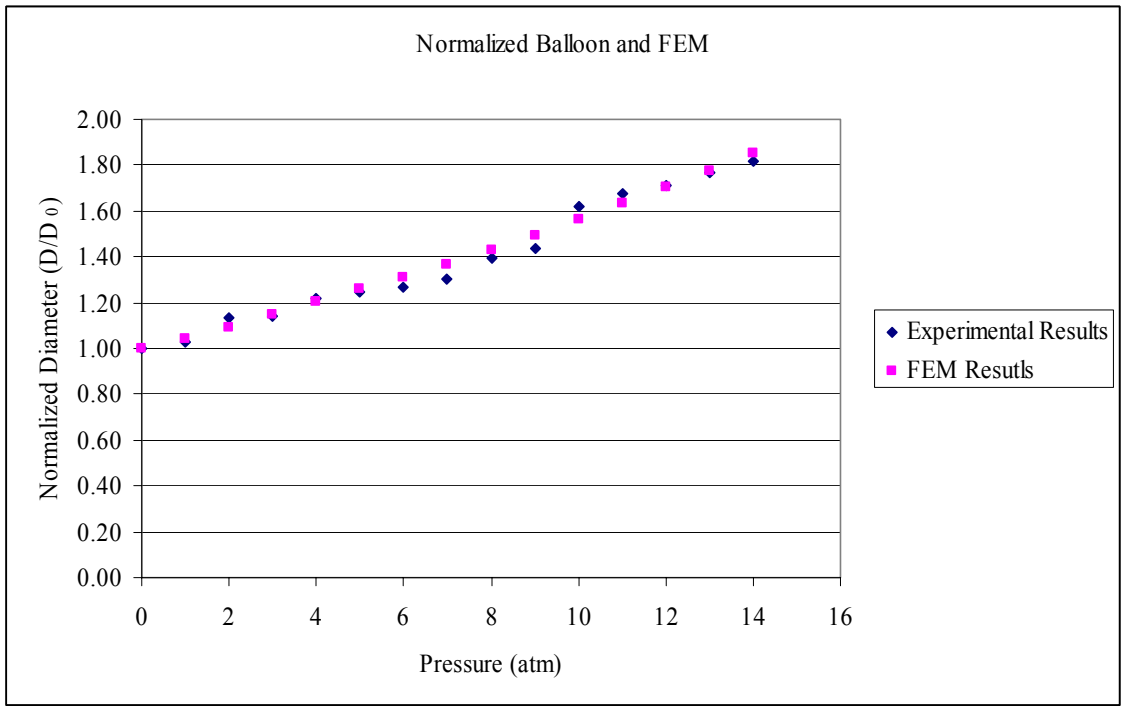

Fig. 4.2 Normalized Experimental and FEM Simulation Results

4.2 Post Deployment Stent Structural Behavior

The displacements in the stent fiber along the radial and axial directions lead to the determination of the structural behavior of the stent. These structural properties of the stent are determined by measuring the initial length of the stent, axial length of the stent and the diameter of the stent during deflation from 14(atm) to 0(atm). These measurements are shown in Table 4.1 for Stent 002 and Table 4.2 for Stent 003.

Table 4.1 Stent 002 Deflation Data

Deflation Pressure (atm)	Axial Length (mm)	Initial Length (mm)	Diameter (mm)
0	7.08	8.75	2.06
14.00	8.35		2.37

Table 4.2 Stent 003 Deflation Data

Deflation Pressure (atm)	Axial Length (mm)	Initial Length (mm)	Diameter (mm)
0	7.94	8.74	2.10
14.00	8.43		2.38

Table 4.3 Structural Behavior Properties

	Foreshortening (%)	Longitudinal Recoil (%)	Diameter Recoil (%)
Stent 002	4.57	6.59	13.08
Stent 003	3.55	5.81	11.76

Stent 002 has an initial length of 8.75(mm) before mounting onto the catheter. After being pushed onto the catheter, the length at 0(atm) is 7.08(mm) and the diameter is 2.06(mm). The length and diameter at 14(atm) is 8.35(mm) and 2.37(mm) respectively. Stent 003 has an initial length of 8.74(mm) before being mounted onto the catheter, and after being mounted onto the catheter, at 0(atm) a length of 7.94(mm) with a diameter of 2.10(mm). The length of the stent 003 at 14(atm) is 8.43(mm) with a diameter of 2.38(mm). These measurements are used to determine the stent's structural properties: foreshortening, longitudinal recoil and diameter recoil. These values are listed in Table 4.3. Foreshortening, longitudinal recoil, and diameter recoil are determined by the following formulas.

$$Foreshortening = \frac{L_i - L_{14}}{L_i}$$

$$Longitudinal\ Recoil = \frac{L_{14} - L_0}{L_{14}}$$

$$Diameter\ Recoil = \frac{D_{14} - D_0}{D_{14}}$$

The variable L_i is the initial length of the stent, L_0 is the length of the stent at 0(atm), and L_{14} is the length of the stent at 14(atm). The variable D_0 is the diameter of the stent at 0(atm) and D_{14} is the diameter of the stent at 14(atm). Stent 002 has a foreshortening value of 4.57% and Stent 003 has a foreshortening value of 3.55%. Stent 003 has more of an axial displacement at 14(atm) which leads to a lower foreshortening effect of the stent. The diameter recoil for Stent 002 is 13.08% and the longitudinal recoil is 6.59%. Stent 003 has lower values for the longitudinal recoil of 5.81% and lower diameter recoil of 11.76%. After expansion, Stent 003 has higher readings for the diameter and the axial length. The installation of the stent on the catheter may explain the difference in the results by Stent 003 being distributed more axially on the balloon. The results in each case have a difference from 0.77% to 1.32%.

4.3 Fiber Stress and Plastic Yielding During Stent Expansion

In the stent experiment, the balloon expansion data reveals the effects of the balloon expanding the stent to a plastically deformed shape. The stent is composed of seven coils and three reinforcement fibers as shown in Fig. 3.1. The balloon shows an almost linear relationship increasing with the 1(atm) pressure increments in Fig. 3.16. At higher applied pressure the stent diameter has a smaller range of diameter displacement than at lower applied pressures shown in Table 3.2 with the diameter difference between the three trials varying from 0.6(mm) at 0(atm) to 0.12(mm) at 14(atm). Also, the increasing diameter of the balloon contacts the internal coils of the stent and pushes the internal coils of the stent to an expanded shape to a diameter of 2.38(mm)-2.50(mm) as shown in Table 3.2. The balloon without a stent expands to a

larger diameter because it does not have any resistance from a stent mounted onto it. The balloon expansion causes the stent material to deform through the elastic region and into the plastic region of the stent surpassing the yield strength of the PLLA material. Since the material plastically yields, the stent does not return to its original shape. The balloon expansion and deflation presents permanent plastic deformation into the stent.

The radial expansion of the stent is shown in Table 3.2. This data is important in understanding the expansion of the outer diameter of the stent in the simulation of the FEM. The overall outer coil diameter displacement in the stent radius is 0.69(mm). The average radial coil incremental change per pressure is 0.049(mm).

The data from Table 3.3 is used to determine the axial displacement in the stent from 0(atm) to 14(atm). The percent elongation for expansion is 7.86% that is determined by the following equation with L_{14} being the length of the stent at 14(atm) and L_0 denoting the length of the stent at 0(atm).

$$PercentElongation = \frac{L_{14} - L_0}{L_0} * 100$$

Due to pressure loading on the base of the internal coil, as shown in Fig. 2.11, the stent expands axially and radially. The 120° stent modeled is not perfectly symmetric and the response of the different cases shows these results. The stent analysis needs to account for the plastic deformation of the model from 1(atm) to 14(atm). Material nonlinear plasticity is used with multilinear data input for the stress-strain relationship. However, for large strain deformations the stress-strain data must be

in terms of Cauchy stress and finite strain. The different case studies are presented in Fig. 2.9 and the data is shown in Table 2.1, Table 2.2, Table 2.3 and Table 2.4.

4.3.1 Poisson's Ratio of the PLLA Material

The Poisson's ratio needs to be accounted for the polymer material for the simulation. A Poisson's ratio of 0.35 is used for all four cases to test the sensitivity to Young's modulus. To understand the effect of Poisson's ratio, a value of 0.4999 is used to account for the incompressibility of the stent fiber material.

Poisson's ratio is the ratio between the lateral and longitudinal strain. The range for Poisson's ratio for polymer materials is between 0.4999 and 0.3 (Seymour, 1993). The yield stress for the different test cases of different material properties is shown in Table 4.4.

Table 4.4 PLLA Fiber Properties for four different Material Cases

Cases	Fiber Type	Young's Modulus (MPa)	Yield Stress (MPa)
Case 1 (baseline)	PLLA (1:5)	7043	359
Case 2	C-PLLA (1:5)	4701	316
Case 3	Commercial Fiber	3189	346
Case 4	PLLA (1:4)	2631	244

4.3.2 Direction of Principal Stress on the Fiber Surface

For the Poisson's ratio of 0.35 at 1x displacement is the standard for the simulation analysis. This study shows the response of the principal stresses S1 and S3 and the principal strain E1 and E3. Fig. 3.23 shows the vector plot of principal stresses during loading at 1(atm). The stent is divided into three sections for this discussion. Section 1 of the stent begins at the left side of the fiber to the beginning of the internal

coil colored as bronze in Fig. 4.3. Section 2 is the 360° internal coil colored in dark blue, and Section 3 is the remaining part of the fiber colored in dark red.

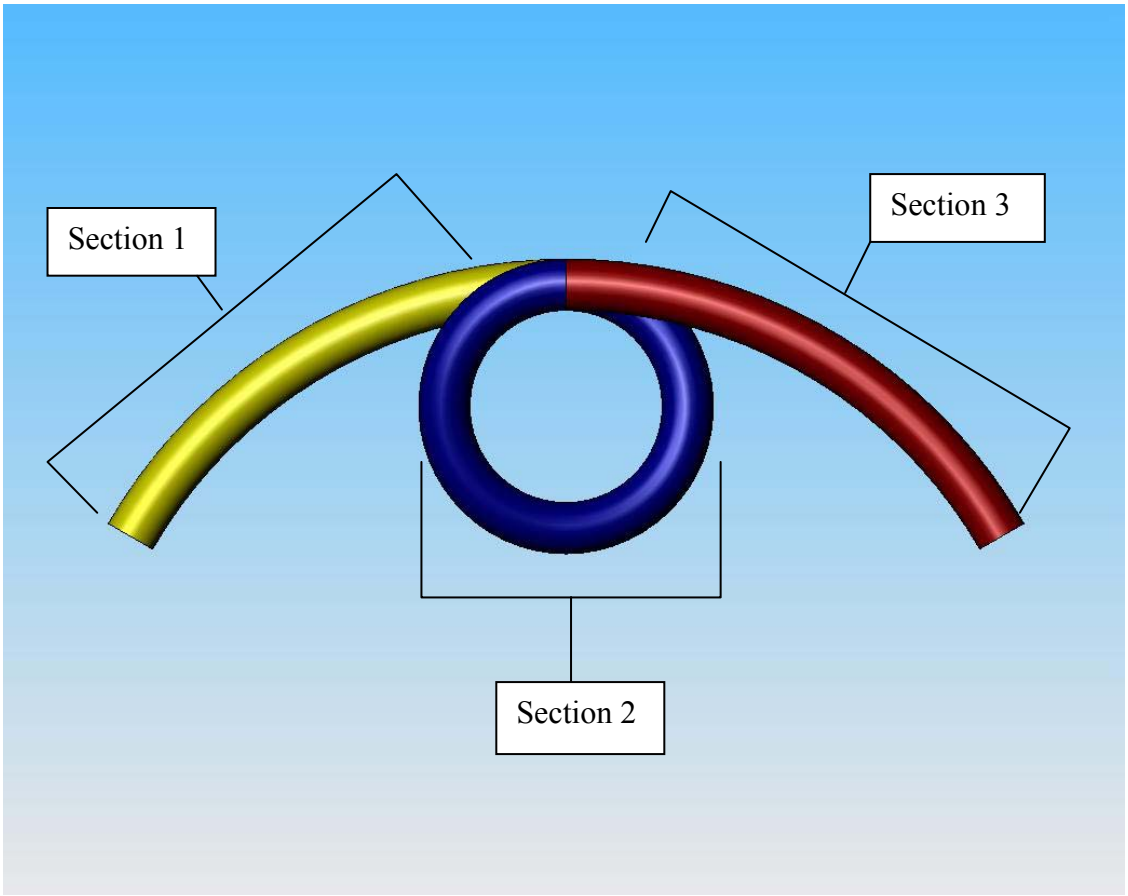

Fig. 4.3 Stent Section 1, Section 2, Section 3 Regions

Starting from the Section 1 in Fig. 4.3, tension stress appear near the boundary conditions applied to the end of the PLLA fiber and then these stresses rotate to the inside surface of the fiber and then back to the outside of the fiber near the internal coil. Then the S1 stress rotates back to the inside surface of the fiber approaching the top of the internal coil and finally rotates to the outside surface approaching the right end of the fiber. This rotation is due to the radial expansion of the fiber along with the axial

displacement of the fiber ends along with the applied pressure load forcing the internal coil to twist into a deformed shape as shown in Fig. 3.39. Also, the loading causes high compressive stresses, S3, to appear on the outside surface of the fiber and being rotated to the inside of the small coil and then rotating to the outside surface and back to the inside surface near the right end of the PLLA fiber. Approaching 14(atm) the S1 stresses are more dominant on the inside surface and outside surface of the internal coil of the PLLA fiber. At 14(atm) the PLLA fiber is deformed and twisted and the pressure loading causes higher S1 stresses in the coil region, and the S3 stresses are more dominant on the outside surface of the PLLA fiber as shown in Fig. 3.22 and Fig. 3.20.

4.3.3 Inside and Outside Surface Principal Stress and Strain

The inside surface principal strain in Fig. 3.19 displays the material yielding occurring at 1.00(mm) to 2.40(mm) for E1. This is in the internal coil region for the stent. The yielding strain occurs at 0.051 in tension and compression. Yielding for E3 strain occurs from 1.25(mm) to 2.16(mm). The outside surface in Fig. 3.21 shows the yielding occurring for E3 strain and not E1 strain. Yielding for E3 occurs in Section 2 from 1.10(mm) to 2.79(mm).

The inside surface principal stresses display the yielding of the fiber from 1.10(mm)-1.15(mm) and 2.25(mm)-2.30(mm) for the S1 stress. The S3 stress does not reach yielding the yielding stress in compression. The maximum shear stress also increases in section 2 to a value of 200(MPa). The outside surface does show yielding occurring in S3 from 1.12(mm)-1.20(mm) and 2.70(mm)-2.77(mm). The maximum shear stress also increases to 200(MPa) the same as the inside surface.

4.3.4 von Mises Yielding Criteria and Yielding Strain

The applied pressure, twisting motion in the radial and axial direction, and the displacement in the radial and axial direction result in the PLLA fiber to overcome its yield stress of 377(MPa). Surpassing the material's yield stress causes its strain energy to move out of the elastic strain region and into the plastic region. Plastic deformation results in the material maintaining its structural uncoiled shape as shown in Fig. 3.45. The distortion energy gives a measure of shear stress present in the PLLA fiber. The yielding criterion is given in the following equation (Norton, 1996).

$$S_y = \sqrt{\sigma_1^2 + \sigma_2^2 + \sigma_3^2 - \sigma_1\sigma_2 - \sigma_2\sigma_3 - \sigma_1\sigma_3}$$

In three dimensions, the distortion energy describes a circular cylinder that defines the region of combined stresses σ_1, σ_2, and σ_3 safe against yielding under static loading. Fig. 3.20 shows the principal stresses σ_1, σ_3, and τ_{max} in the PLLA fiber on the inside surface. The yielding stress is 377(MPa) and Fig. 3.20 shows this yielding occurring at approximately 1(mm) or in Section 2 from Fig. 4.1. The corresponding yielding strain is at 5.1%. Fig. 3.19 also shows the yielding of the material on the inside surface increasing above the yield strain at approximately 1(mm) or in Section 2. Fig. 3.42 shows the cross sectional view of the PLLA fiber total principal strain E1. This shows the outside surface yielding and the inside core of the fiber remaining in the elastic region of the stress-strain curve and Fig. 3.39 shows the plastic yielding of the fiber on the surface in Section 2.

The effective von Mises stress at 14(atm) is calculated from 344(MPa) to 386(MPa) as shown in Fig. 3.49. The stresses are beyond the edge of the failure stress cylinder zone in shear with a maximum stress of 218(MPa) on the outside surface. The von Mises stresses at 1(atm) show a maximum stress of 73-82(MPa) in Fig. 3.43. These are the initial stresses the PLLA fiber experiences during the balloon inflation process. The plastic yielding occurs at 7(atm) with the von Mises stresses shown in Fig. 3.44. These stress values are at a maximum value of 337-379(MPa) in Section 2 of the PLLA fiber. At 14(atm) in Fig. 3.45 the von Mises stresses increase through Section 2 of the PLLA fiber. A cross sectional view of the von Mises stresses forming inside the stent are shown in Fig. 3.46 to Fig. 3.49 ranging from 1(atm) to 14(atm). The von Mises stresses increase throughout most of the cross section of the PLLA fiber except in the central coil which can explain the plasticity of the PLLA fiber.

The maximum shear-stress theory also predicts the yield strength of a ductile material to be one half of the materials yield strength. The maximum shear stress for failure is at 179.5(MPa) and the maximum shear stress is 218(MPa) for the inside surface and 217(MPa) for the outside surface. The maximum shear stress is higher than the maximum stress for failure. This results in the material being stressed beyond its safety zone.

4.4 Principal Stress and Strain for Different Cases

The behavior of the stent stresses and strains can be compared to different Young's Moduli. Fig. 3.37 demonstrates the strain behavior of the PLLA fiber from a Case 4 to Case 1 on the inside surface. The principal strains E1 and E3 increase from

Case 4 to Case 1. Also, the area between the curves narrows and the response is symmetric from E1 and E3. This results in the yielding of the PLLA fiber to occur closer to Section 2 in Case 1. Fig. 3.38 demonstrates the outside surface of the PLLA fiber yielding for Case 1 to Case 4. Case 1 results in a more dominant effect of the principal strains in Section 2. The inside and outside surface principal stresses S1, S3, and Tmax are higher for the Case 1. The principal stress plots are also symmetric from S1 to S3.

Under the material incompressibility assumption with the Poisson's ratio set to be 0.4999, the stress responses are not symmetrical for the inside surface as shown in Appendix B. The simulation demonstrates the structural behavior of a coil stent that does not change its volume when experiencing large deformations. The increasing strain values do increase from Case 4 to Case 1 and appear to be symmetric from E1 and E3. The principal stress vector plot shows the increasing second principal stress in Section 3 possibly due to the extreme bending of the fiber accompanied by the model trying to maintain the same volume through large deformations keeping its rigidity. The plastic deformation regions in Section 2 and the von Mises stresses in the fiber and along the outer surface of the fiber are similar to the analysis with a Poisson's ratio of 0.35.

4.5 Effects of Young's Modulus

4.5.1 Maximum Shear Stress for Poisson's Ratio of 0.35

The baseline study also compares the amount of maximum shear stress for different Young's moduli as shown in Fig. 3.53. The results are similar to the

incompressible state showing the maximum amount of shear stress remaining the same on the outside and inside surface of the PLLA fiber with Case 1 and Case 2. The maximum shear stresses for Case 3 and Case 4 decreased on the outside surface.

4.5.2 Axial Displacement Comparison for Poisson's Ratio of 0.4999

The Young's Moduli are used to compare the amount of displacement and the amount of maximum shear stress in for the incompressible state. The maximum shear stress is consistently the same from 1x displacement to 3x displacement on the inside surface. Comparing the inside and outside surface, the maximum shear stress remains constant in Case 1 and Case 2 on the both the inside and outside surface from 1x displacement to 3x displacement, and the maximum shear decreases with the Case 3 and Case 4 on the outside surface. The maximum shear stress on the inside surface resulted in no change with axial displacement and the maximum shear stress on the outside surface has no change with axial displacement due to the displacement not being large enough to cause a large change in maximum shear stress.

CHAPTER 5

CONCLUSION

The coil stent design is modeled with SolidWorks and used to create a finite element model with ANSYS. The baseline for the experiment is using a Poisson's ratio of 0.35 and a Young's modulus of 7043(MPa) for isotropic material. The input of the material is in terms of Cauchy stress and finite logarithm strain using multilinear plastic material. The compressibility of the PLLA fiber is essential in understanding the effects of the applied pressure loads. The tension and compressive stresses play an interactive role in the plastic deformation of the PLLA fiber. The boundary conditions also cause the uncoiling of the fiber by the expansion of the balloon in the radial direction and the axial direction. The more compressible PLLA fiber experiences a stress response of tension and compressive being similar on the outside surface but not the inside surface. The principal strain responses E1 and E3 on the inside surface is not similar and the principal strain responses on the outside surface is similar. This is due to the asymmetry of the model with a coil design. The asymmetry of the coil design is a helical geometry with a pitch and diameter associated with its axial and radial displacement.

The compressible state also permits the volume of the fiber to change and not behave as a rigid structure. The volume change of the fiber shows the twisting and uncoiling effect of the PLLA fiber and the increasing of stresses near the Section 2.

The maximum shear stress is constant on the inside surface than on the outside surface of the PLLA fiber. This accounts for the plastic yielding of the material due to the twisting motion and the axial displacement of the PLLA fiber during loading. The von Mises stresses in the compressible and incompressible state show similar values and behavior response. The von Mises stresses increase in the area of Section 2. This is expected due to this region experiencing the most deformation and applied pressure loading. The von Mises stresses are higher on the outside surface of the fiber during inflation except for a small internal region. This is the same region that remains in the elastic state after the inflation process. The conformity of plastic yielding throughout the entire cross section of the PLLA fiber is an ideal case that maybe performed by altering the loading and boundary conditions for the PLLA fiber.

Altering the Young's Modulus for the case of Poisson's ratio of 0.4999 at different displacements only show the maximum shear stress remaining constant at the different displacements on the inside and outside surface at the higher Young's Moduli. The outside surface experiences lower shear stresses than the inside surface during the inflation process and yielding of the PLLA fiber occurs on the surface of the fiber and not through the entire fiber. The simulation results are also validated by comparing the experimental data of the balloon inflation with the normalized plots.

Some limitations for the simulation may lead to different results. Some of the mechanical material specifications for PLLA fiber are not published. Understanding the mechanical behavior of PLLA fiber under torsional testing, will help the development of future simulations. The torsional yield stress and the angles applied to testing for

torsional yielding of PLLA are not published. Accurate stress strain data for PLLA fiber needs to be accounted for in the simulation. An assumption of the yield stress is in linear relation with the Young's modulus is used in the simulation. Another assumption is the tensile and compressive yield stress is assumed to be the same value. The behavior of PLLA fiber may show different yield stresses for compression, tension, and torsion loading. Therefore, for future case study simulations the PLLA fiber needs to be better documented for analysis.

In summary, the coil stent simulation has provided the following:

- The internal loop coil has high shear stresses that exceed von Mises yielding stresses.
- There is high plastic deformation on the surface of the PLLA fiber, where as the inner core of the PLLA fiber remains elastic.
- Shear stresses on outside surface path are lower than inside surface path.
- Axial displacement of the fiber didn't seem to affect the shear stresses in the fiber up to 3X (recorded value at 14(atm)).

The coil stent design can be modeled and analyzed for stress interactions upon deployment. The use of FEM simulation can be used for other coil stent applications tailored for different diameters and lengths for patients.

CHAPTER 6

FUTURE STUDIES

Future studies for the stent analysis need to have material characterization for PLLA fiber. This will include testing for the different mechanical properties such as shear modulus, Poisson's ratio, tensile strength and torsional shear strength. After characterizing a complete stress-strain response including plastic yielding behavior of the material, new 3-D models need to be created with more coils to account for the interaction between the reinforcement rods and the outer coils and the interaction between the coils with each other during stent expansion. Another recommendation for the simulation is simulating the balloon expansion within the stent using contact elements and interaction with an arterial vessel. This will help us to capture the full range of the mechanical stress interaction with the arterial vessel during stent deployment.

Investigating the effects of pulsatile flow of blood causing cyclic loading on the stent and formation of eddies in various regions of the stent will also be useful in the stent analysis. The amount of stress formation on and in the stent from pulsatile flow and stent deployment will aid in the geometric design and material parameter formulation for the PLLA polymer. More validation testing is needed for the parameters of the stent expansion and deflation. Finally, after simulation and validation

testing of a new design, animal test trials are needed for verification testing of the stent biocompatibility and inflammation response with the test subject.

APPENDIX A

COIL STENT DRAWING

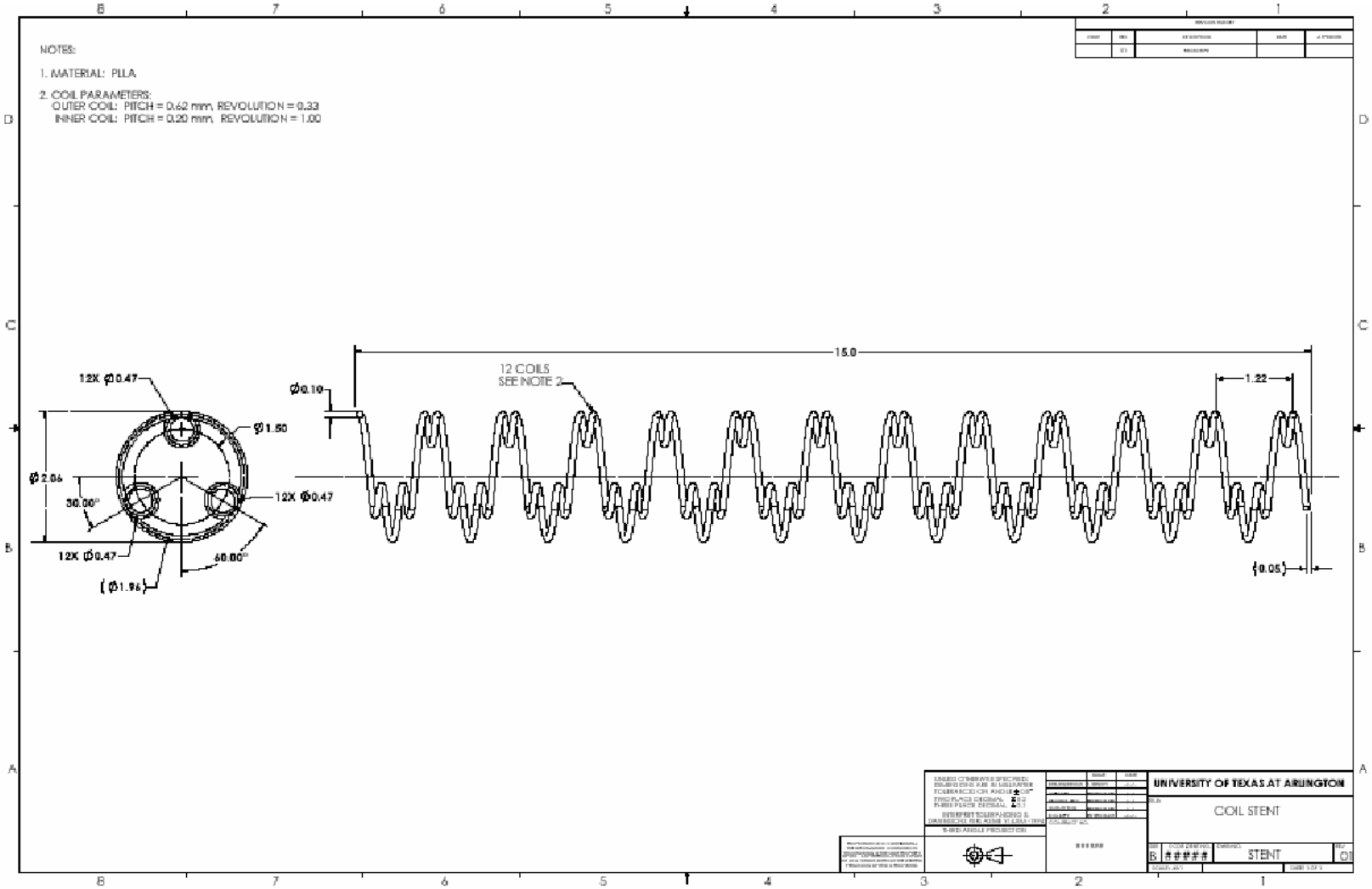

Fig. A.1 Coil Stent Drawing

APPENDIX B

INCOMPRESSIBLE STATE FIGURES

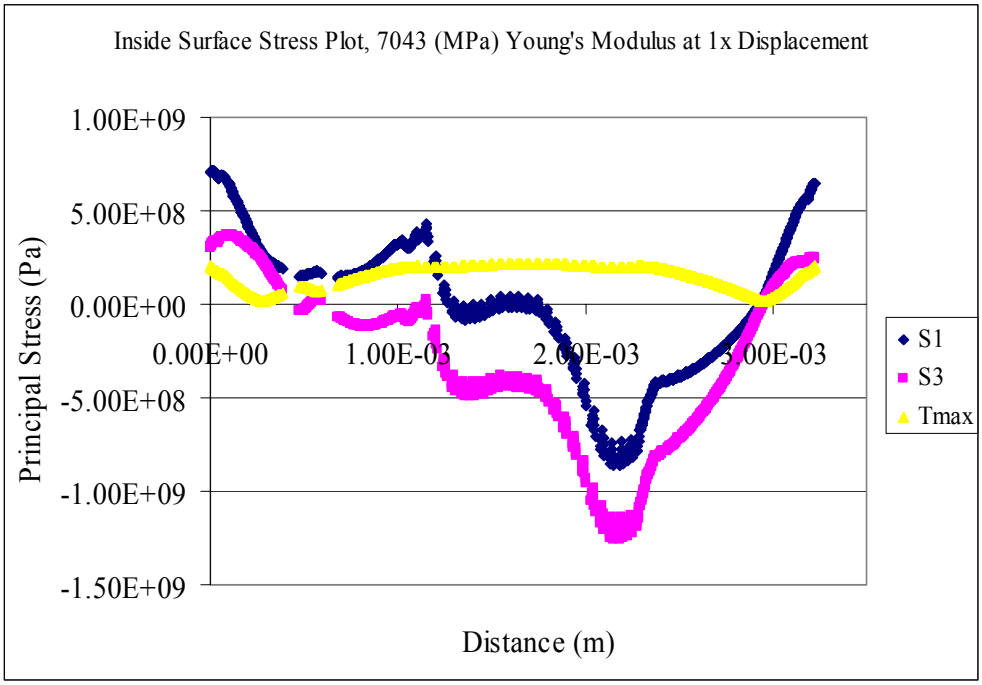

Fig. B.1 Inside Surface Principal Stress S1, S3, and Tmax for 7043(MPa)

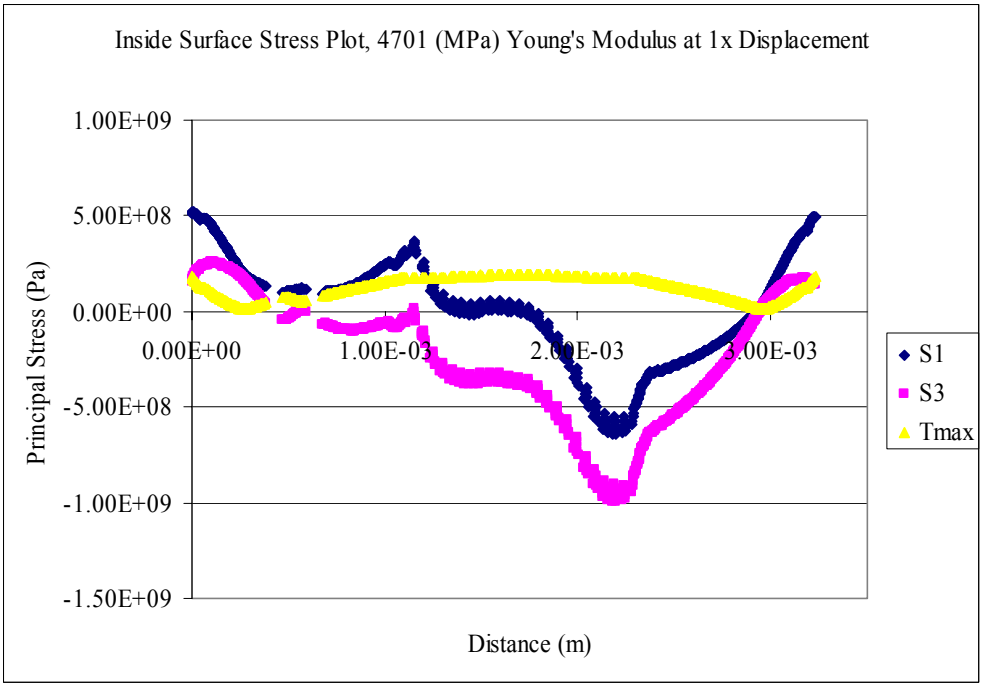

Fig. B.2 Inside Surface Principal Stress S1, S3, and Tmax for 4701(MPa)

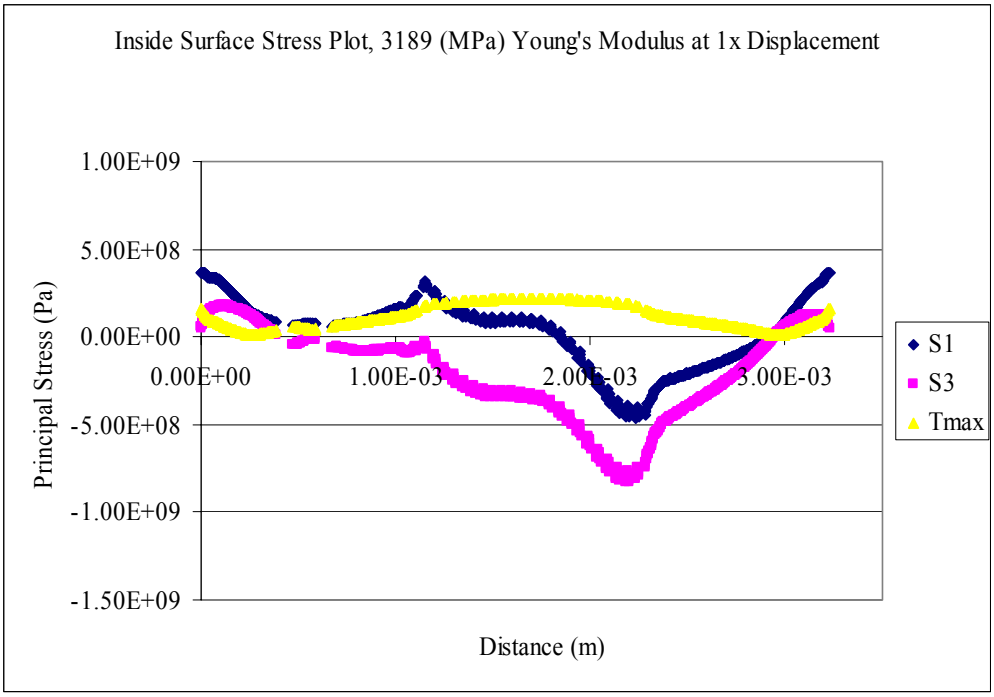

Fig. B.3 Inside Surface Principal Stress S1, S3, and Tmax for 3189(MPa)

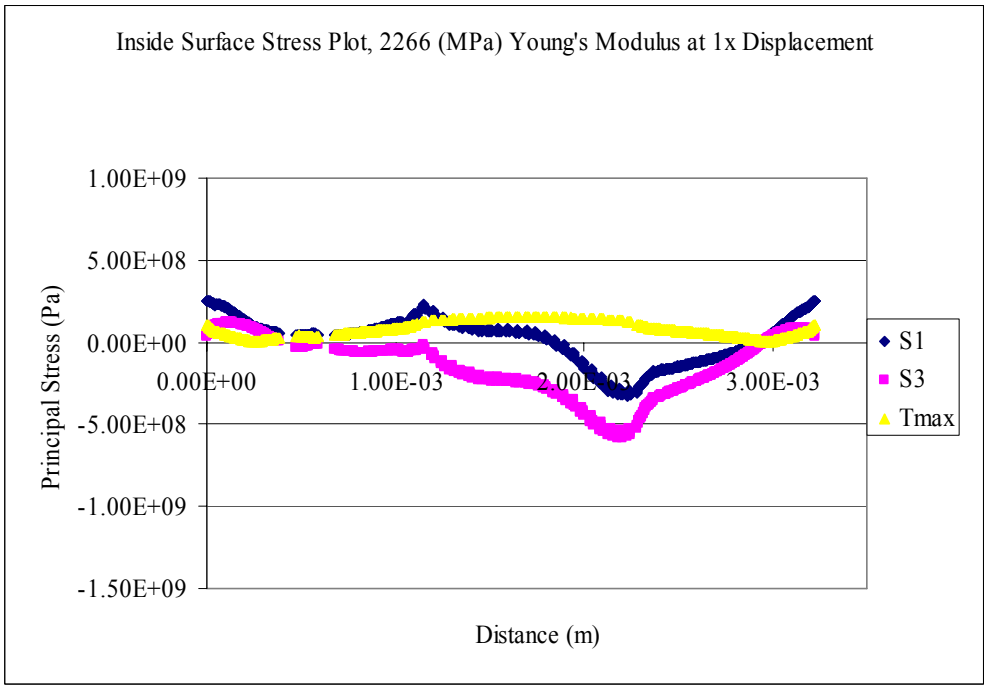

Fig. B.4 Inside Surface Principal Stress S1, S3, and Tmax for 2266(MPa)

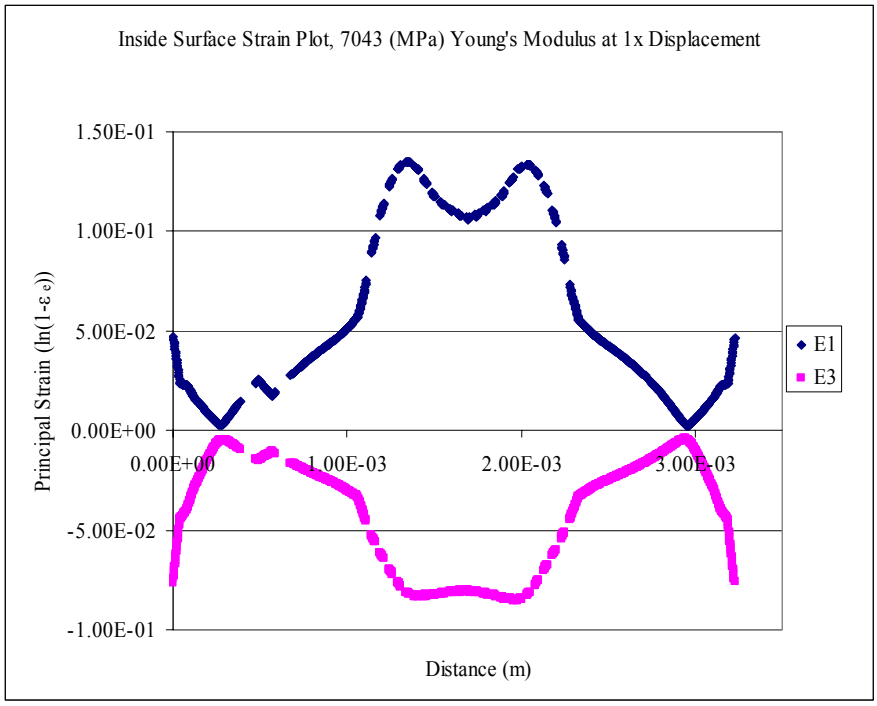

Fig. B.5 Inside Surface Principal Strain E1, E3 for 7043(MPa)

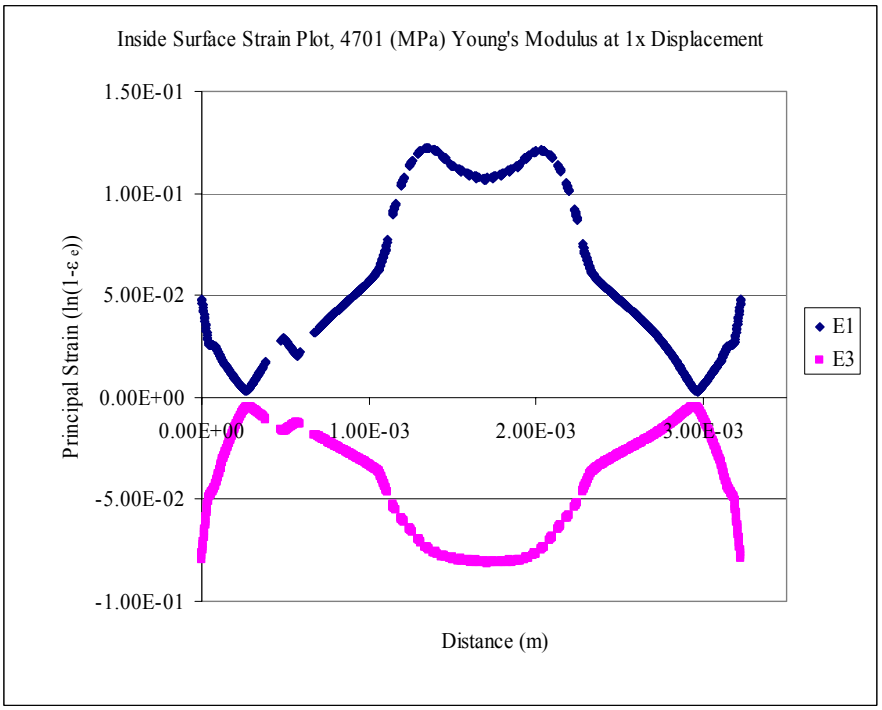

Fig. B.6 Inside Surface Principal Strain E1, E3 for 4701(MPa)

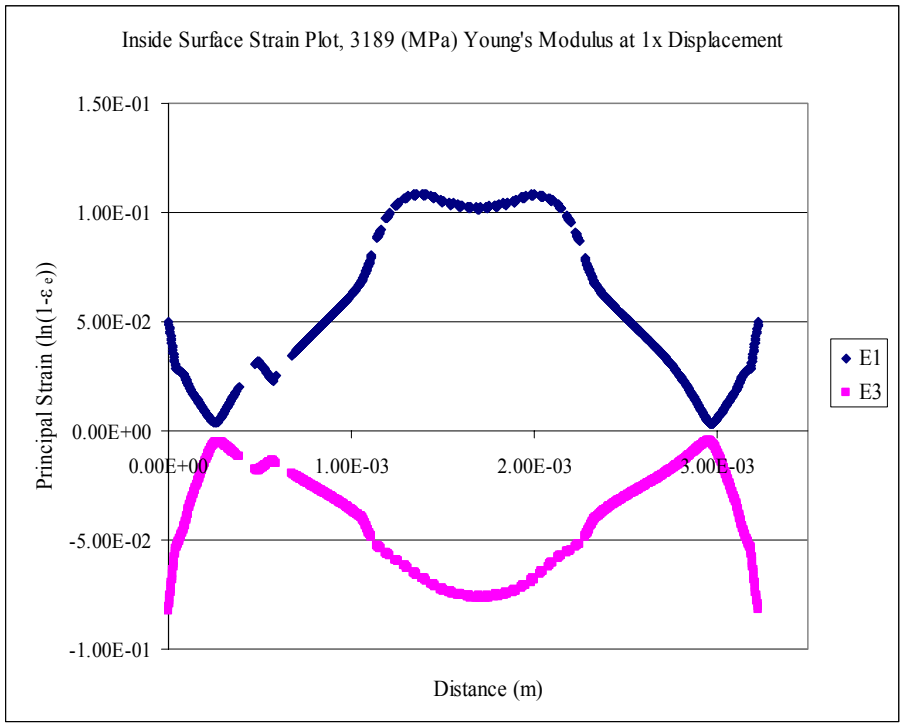

Fig. B.7 Inside Surface Principal Strain E1, E3 for 3189(MPa)

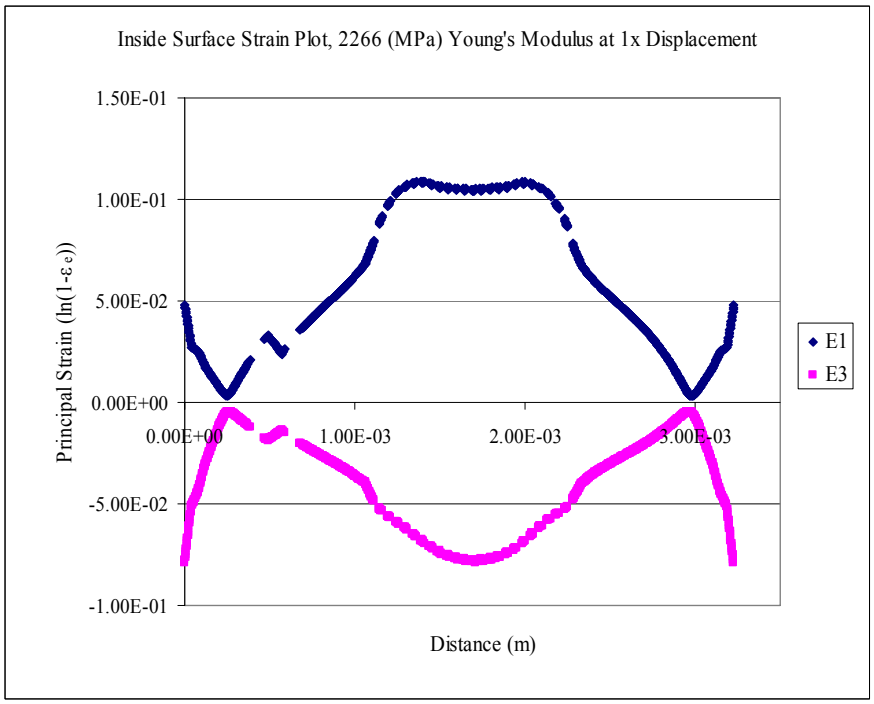

Fig. B.8 Inside Surface Principal Strain E1, E3 for 2266(MPa)

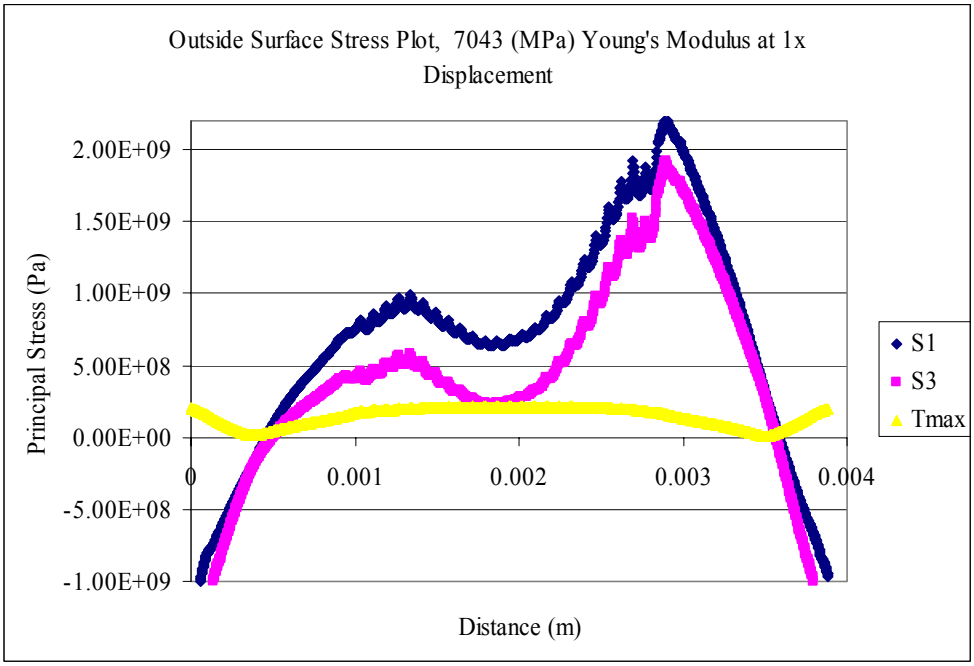

Fig. B.9 Outside Surface Principal Stress S1, S3, and Tmax for 7043(MPa)

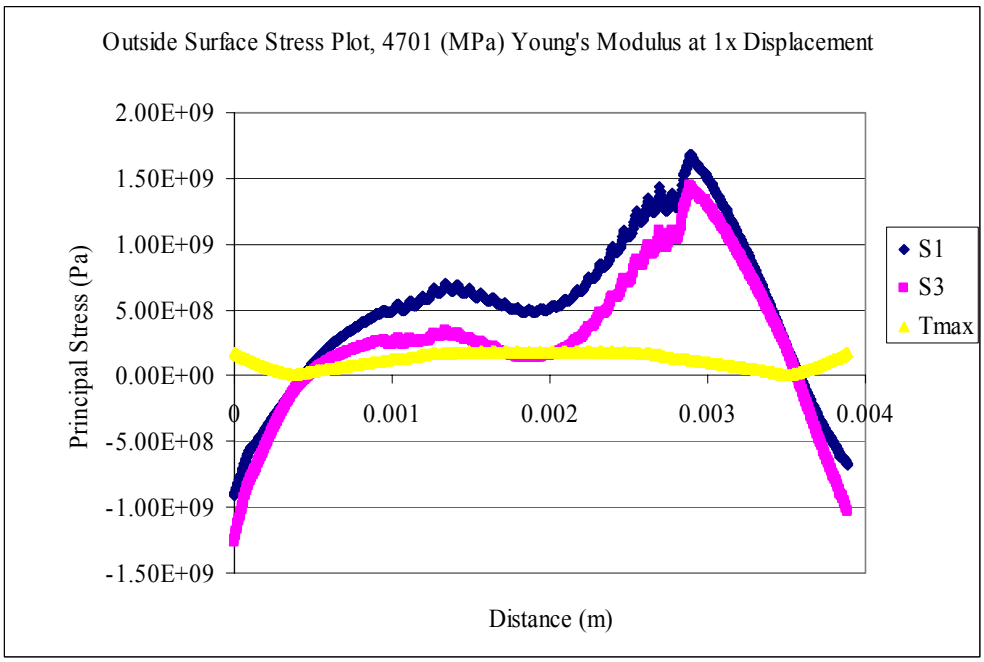

Fig. B.10 Outside Surface Principal Stress S1, S3, and Tmax for 4701(MPa)

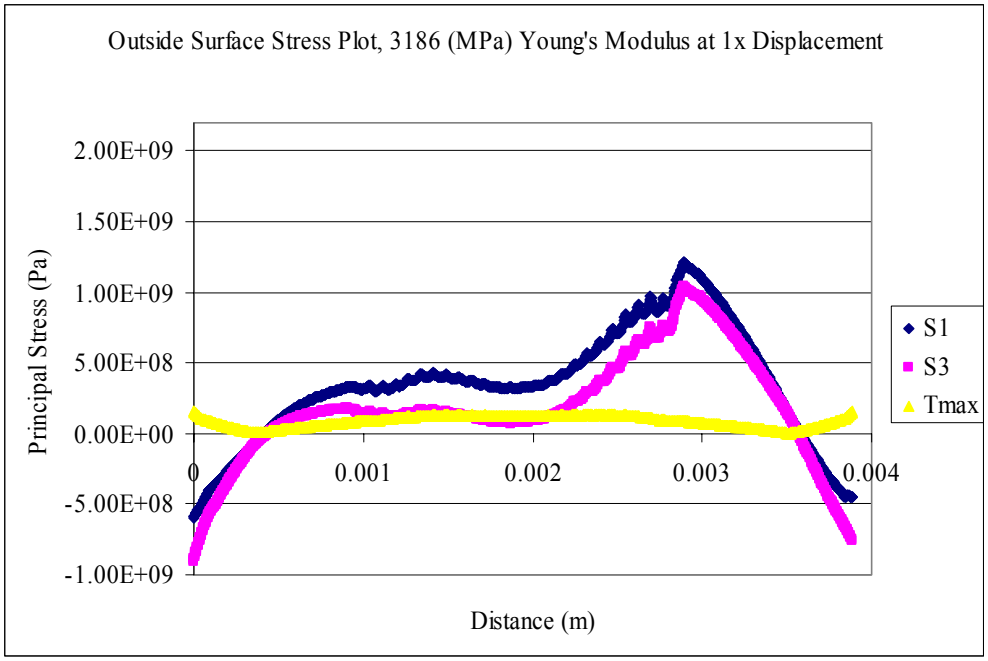

Fig. B.11 Outside Surface Principal Stress S1, S3, and Tmax for 3186(MPa)

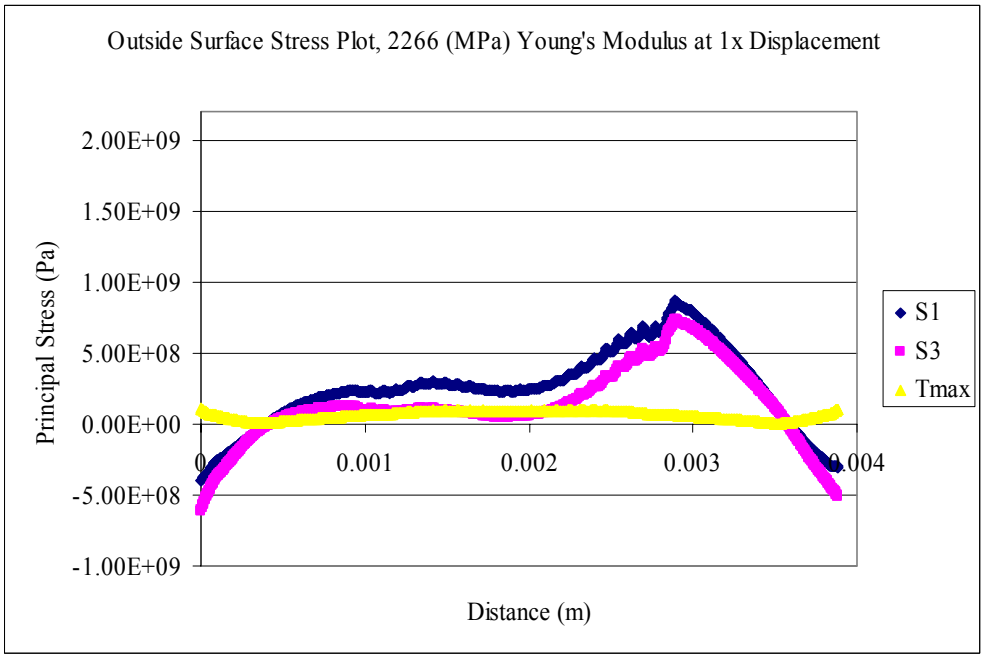

Fig. B.12 Outside Surface Principal Stress S1, S3, and Tmax for 2266(MPa)

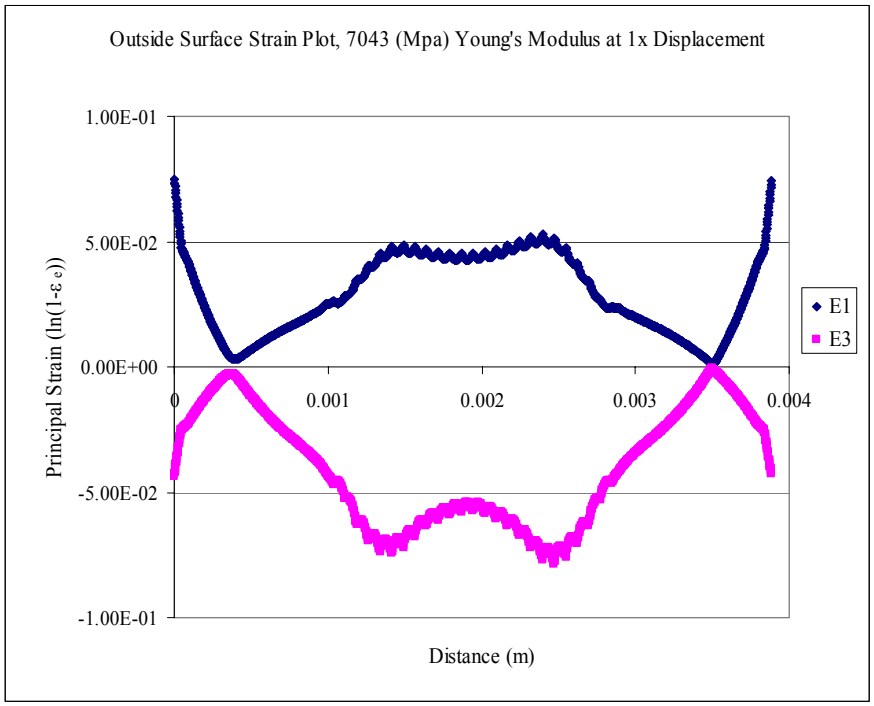

Fig. B.13 Outside Surface Principal Strain E1, E3 for 7043(MPa)

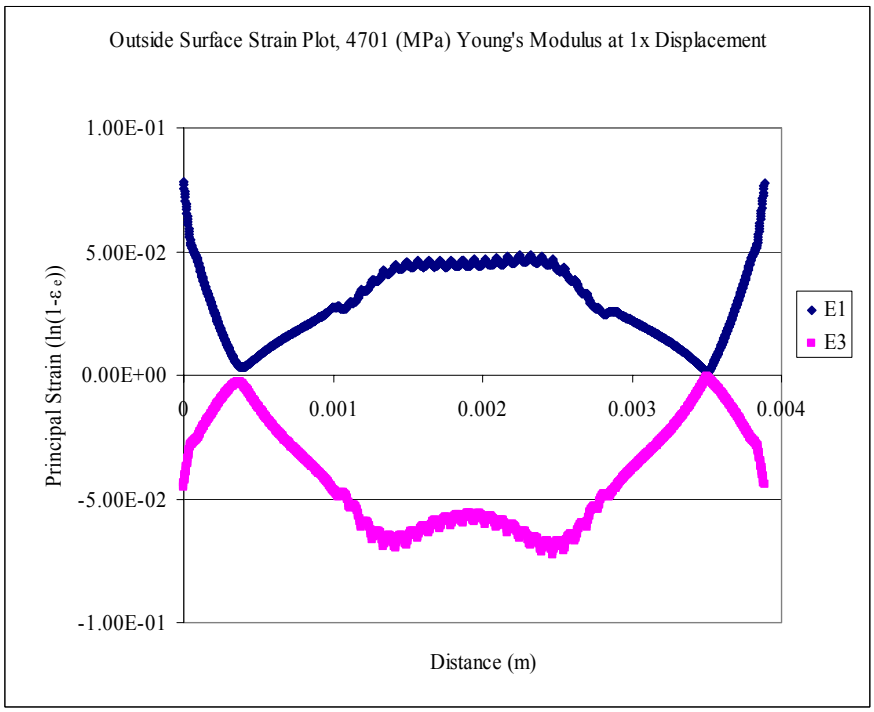

Fig. B.14 Outside Surface Principal Strain E1, E3 for 4701(MPa)

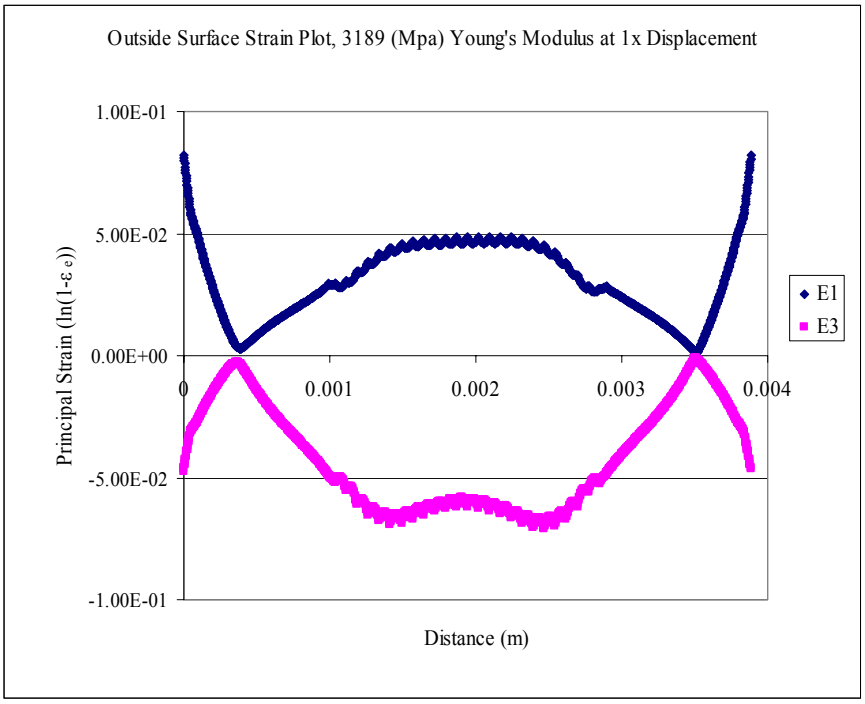

Fig. B.15 Outside Surface Principal Strain E1, E3 for 3189(MPa)

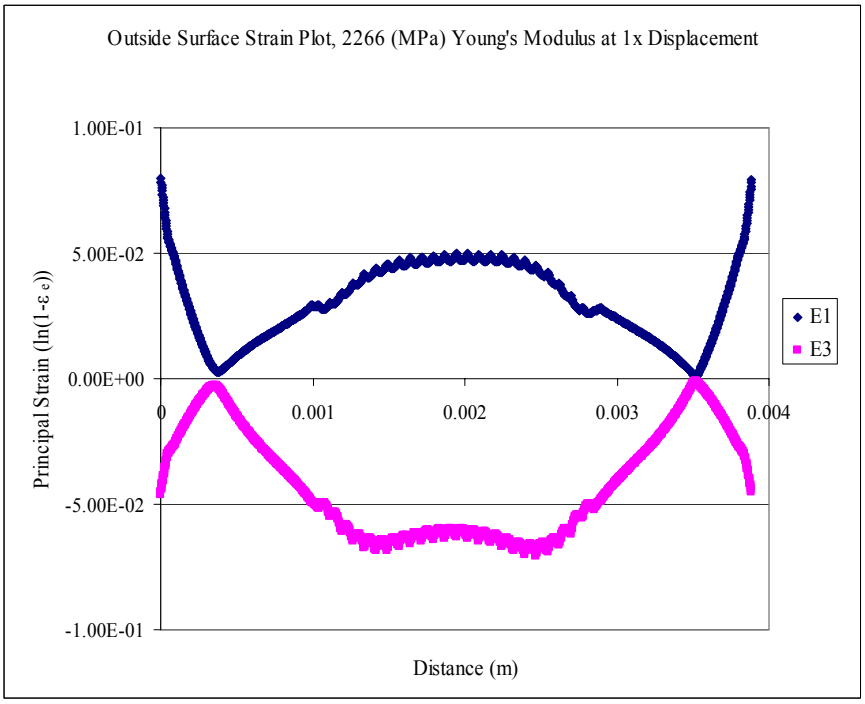

Fig. B.16 Outside Surface Principal Strain E1, E3 for 2266(MPa)

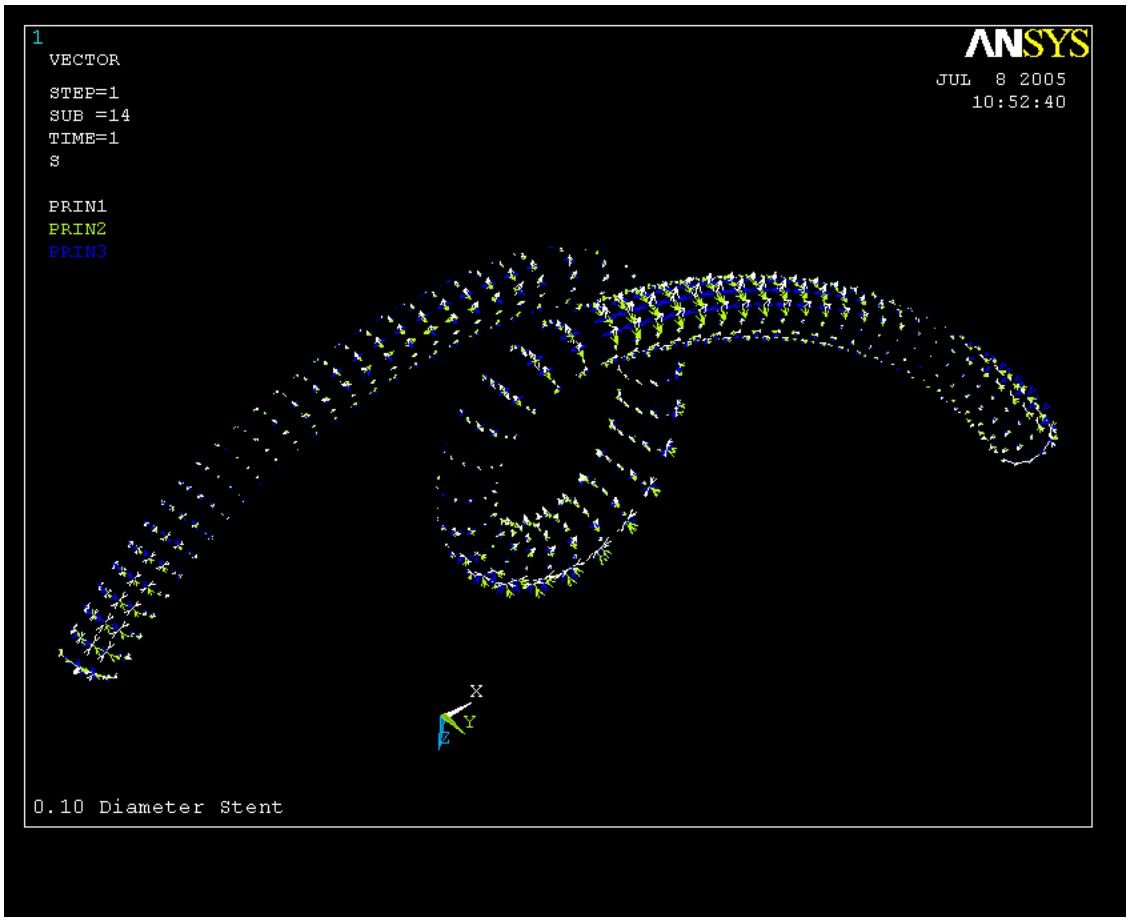

Fig. B.17 Principal Stress Vector Plot Deformed Position at 1(atm)

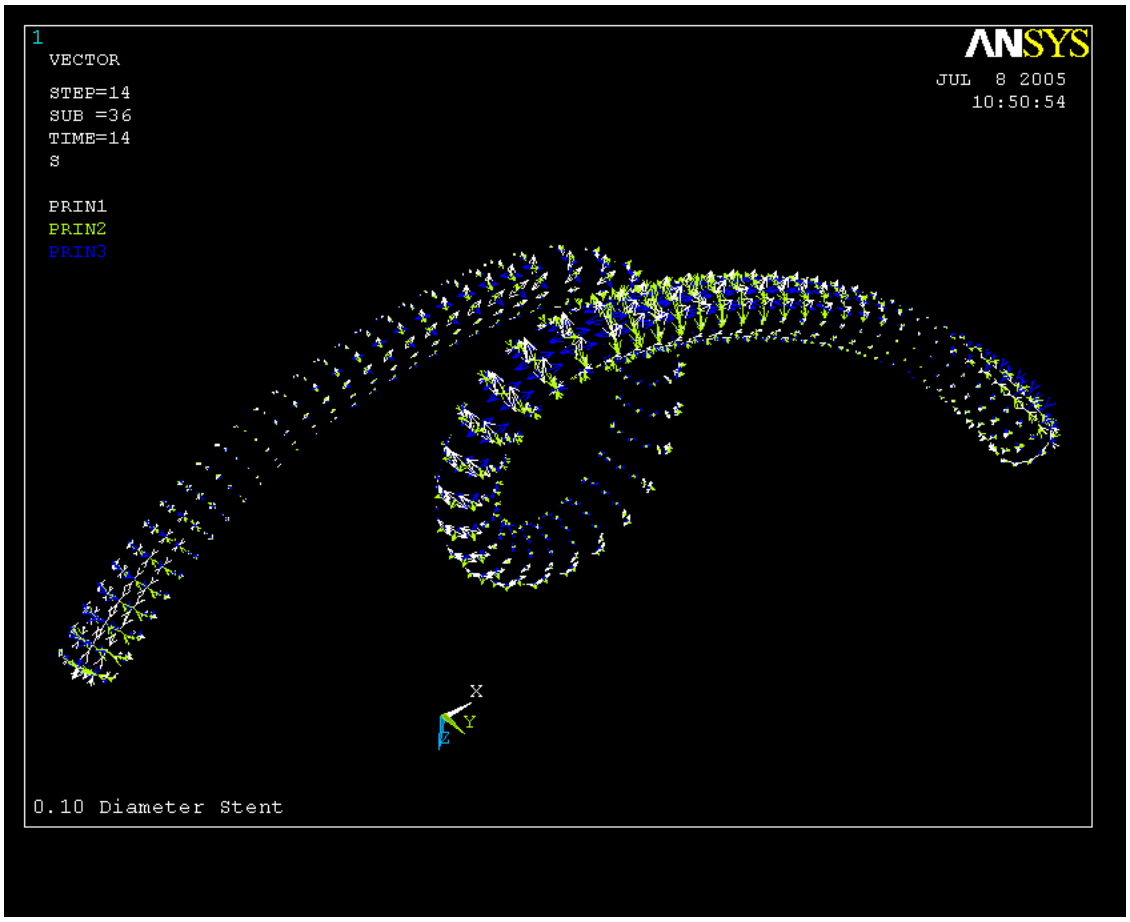

Fig. B.18 Principal Stress Vector Plot Underformed Position at 14(atm)

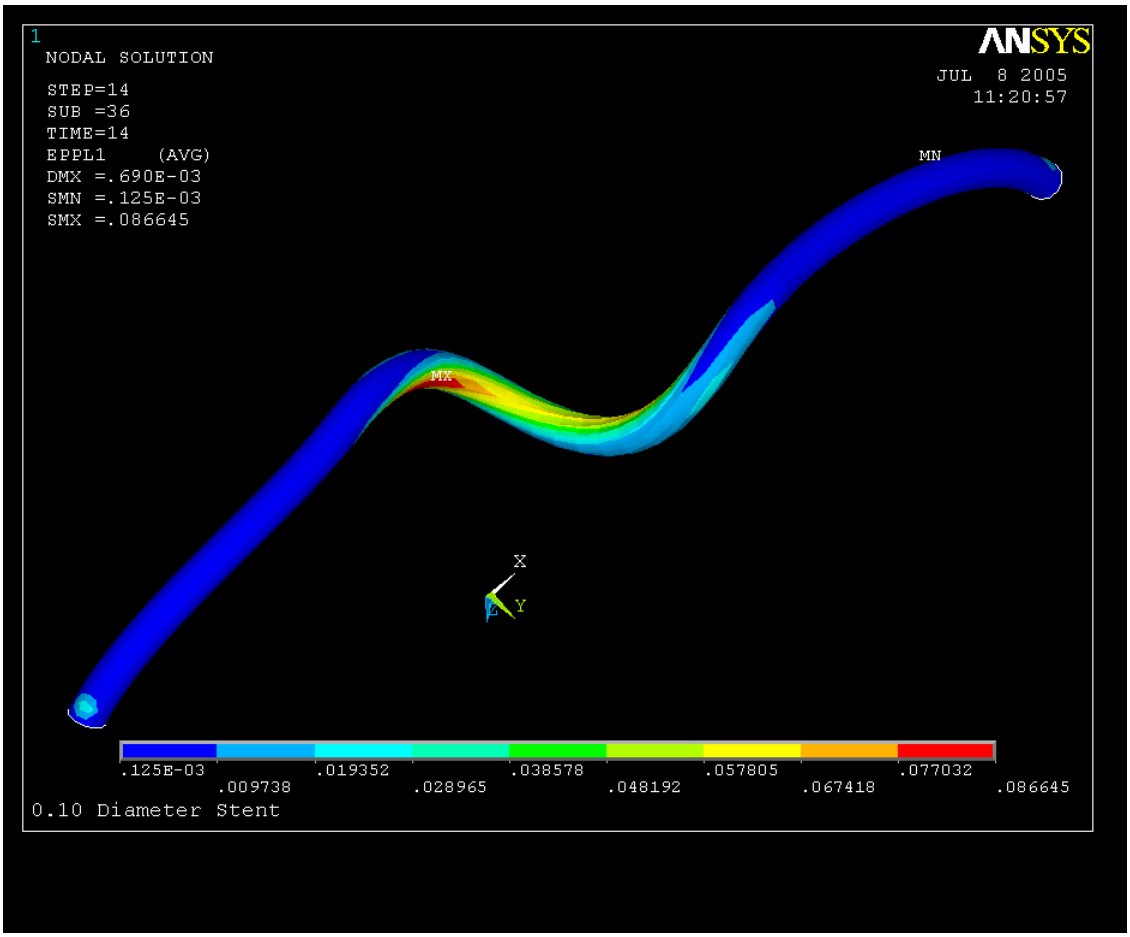

Fig. B.19 Plastic Strain Contour Plot E1 at 14(atm)

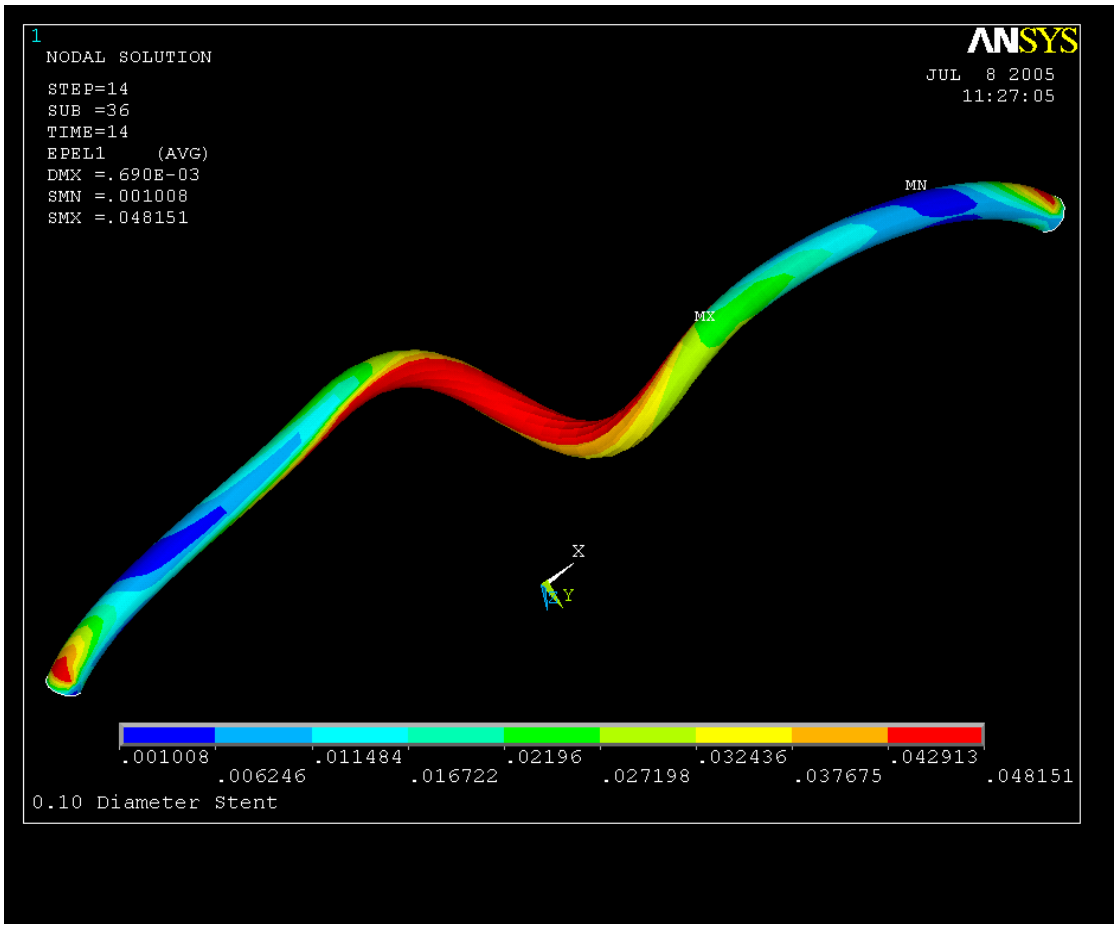

Fig. B.20 Elastic Strain Contour Plot E1 at 14(atm)

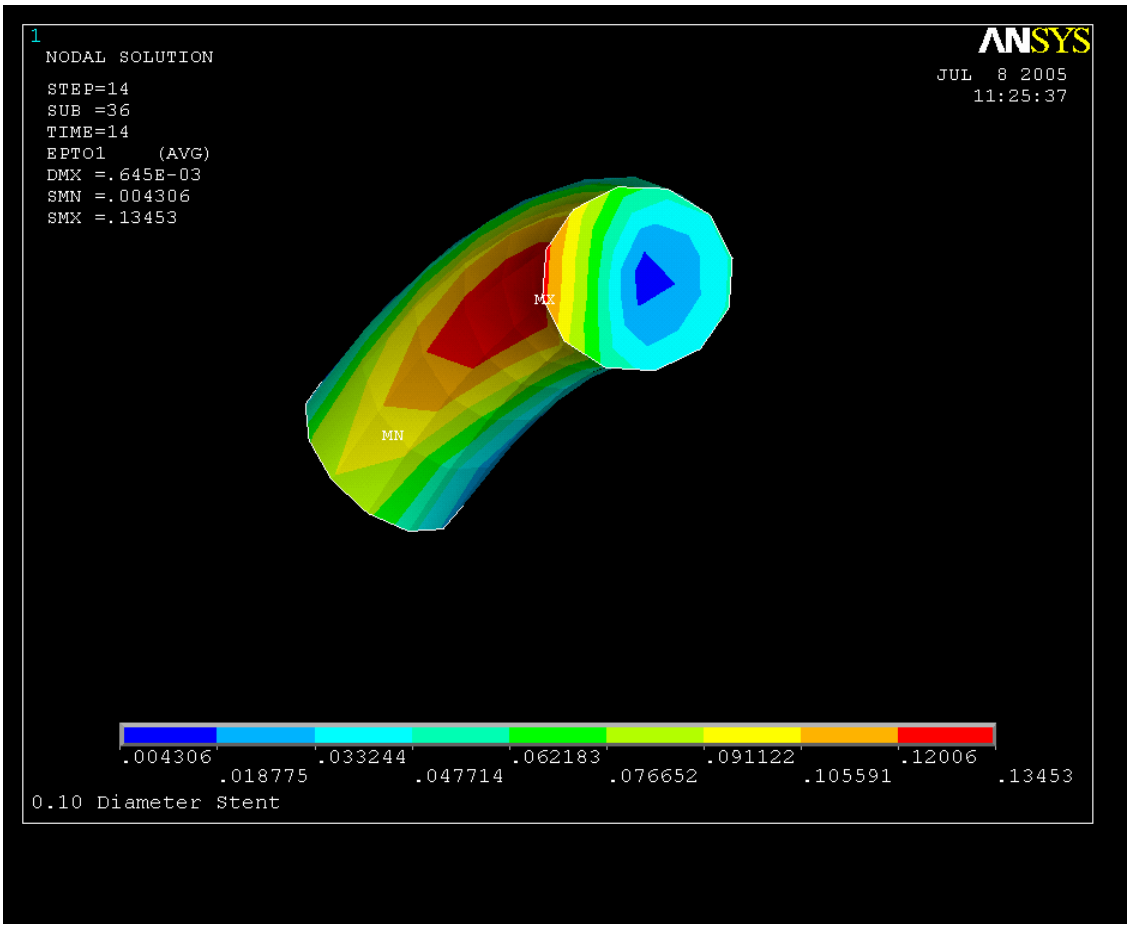

Fig. B.21 Total Principal Strain E1 Contour Plot for Cross Section of PLLA Fiber at 14(atm)

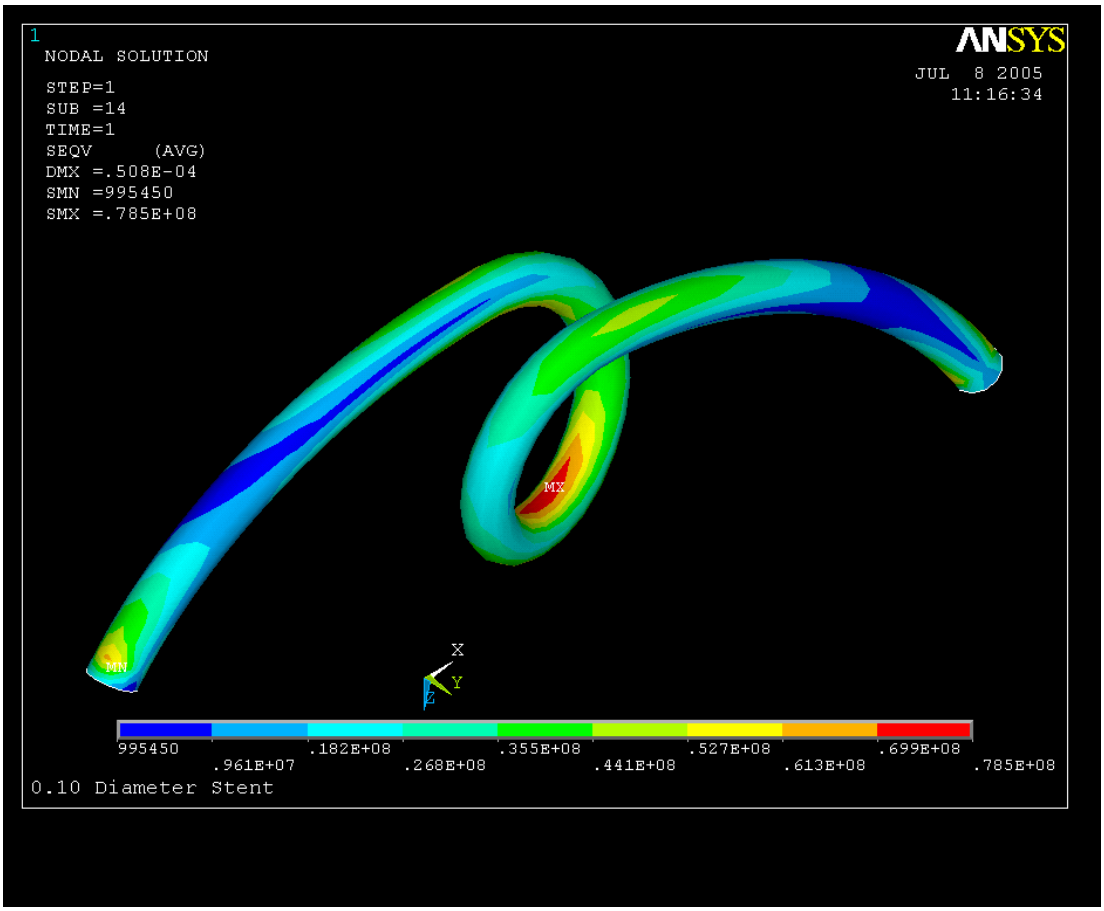

Fig. B.22 Von Mises Stress Contour Plot at 1(atm)

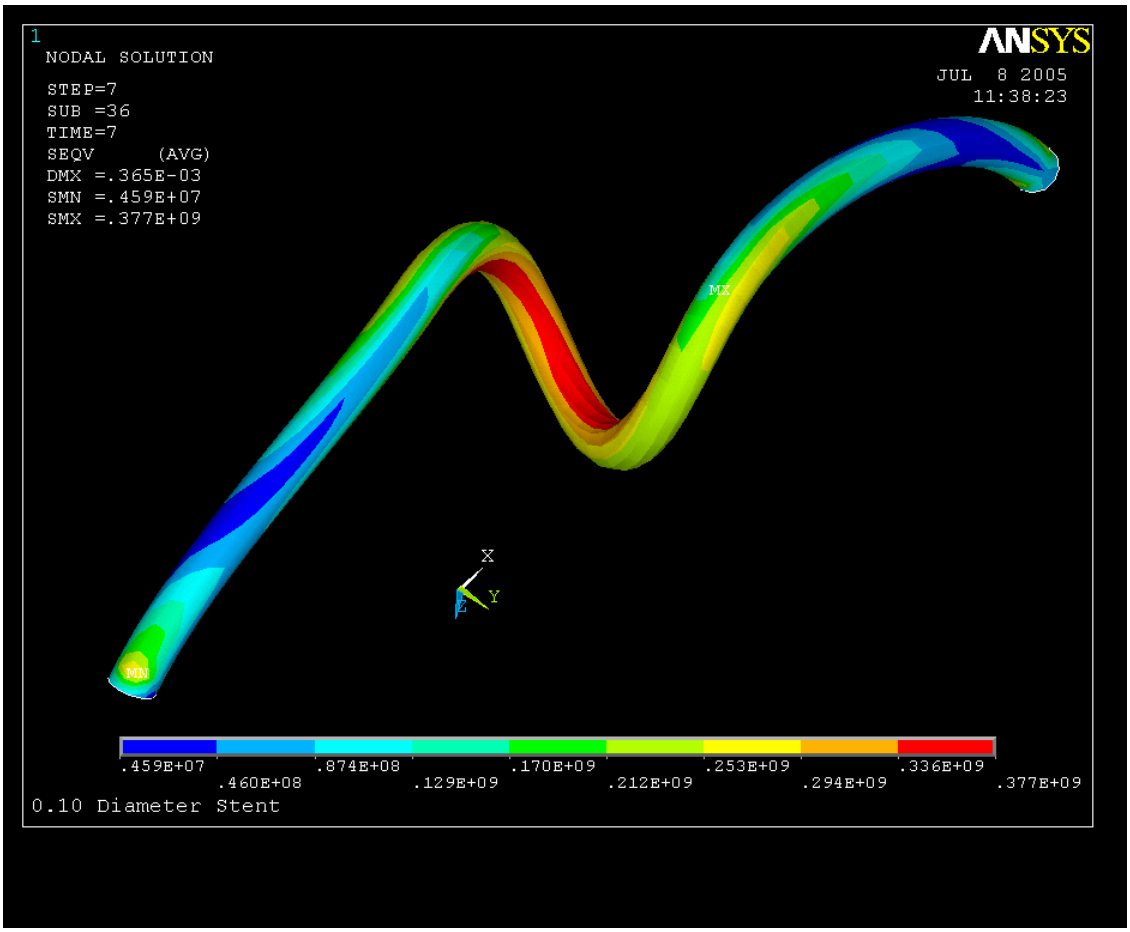

Fig. B.23 Von Mises Stress Contour Plot at 7(atm)

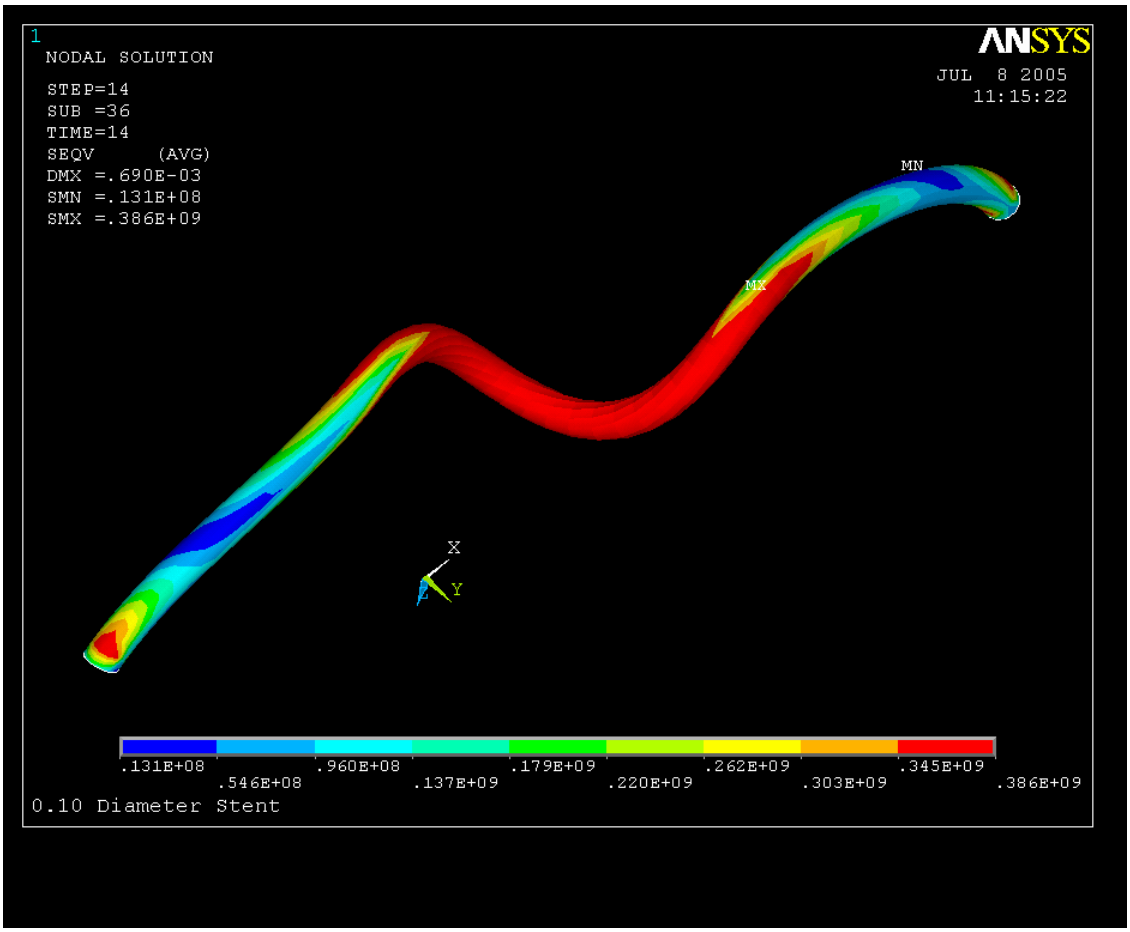

Fig. B.24 Von Mises Stress Contour Plot at 14(atm)

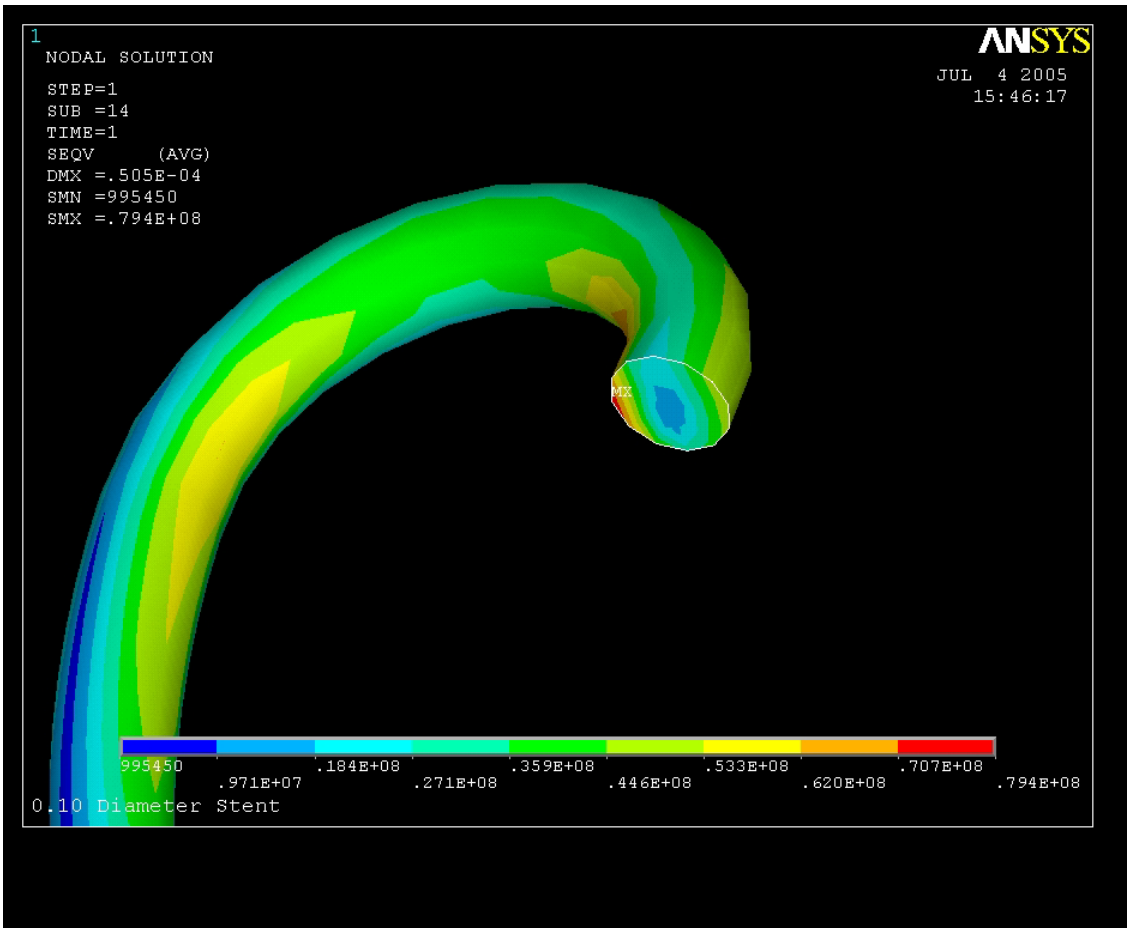

Fig. B.25 Von Mises Stress Contour Plot at 1(atm) of Cross Section PLLA Fiber

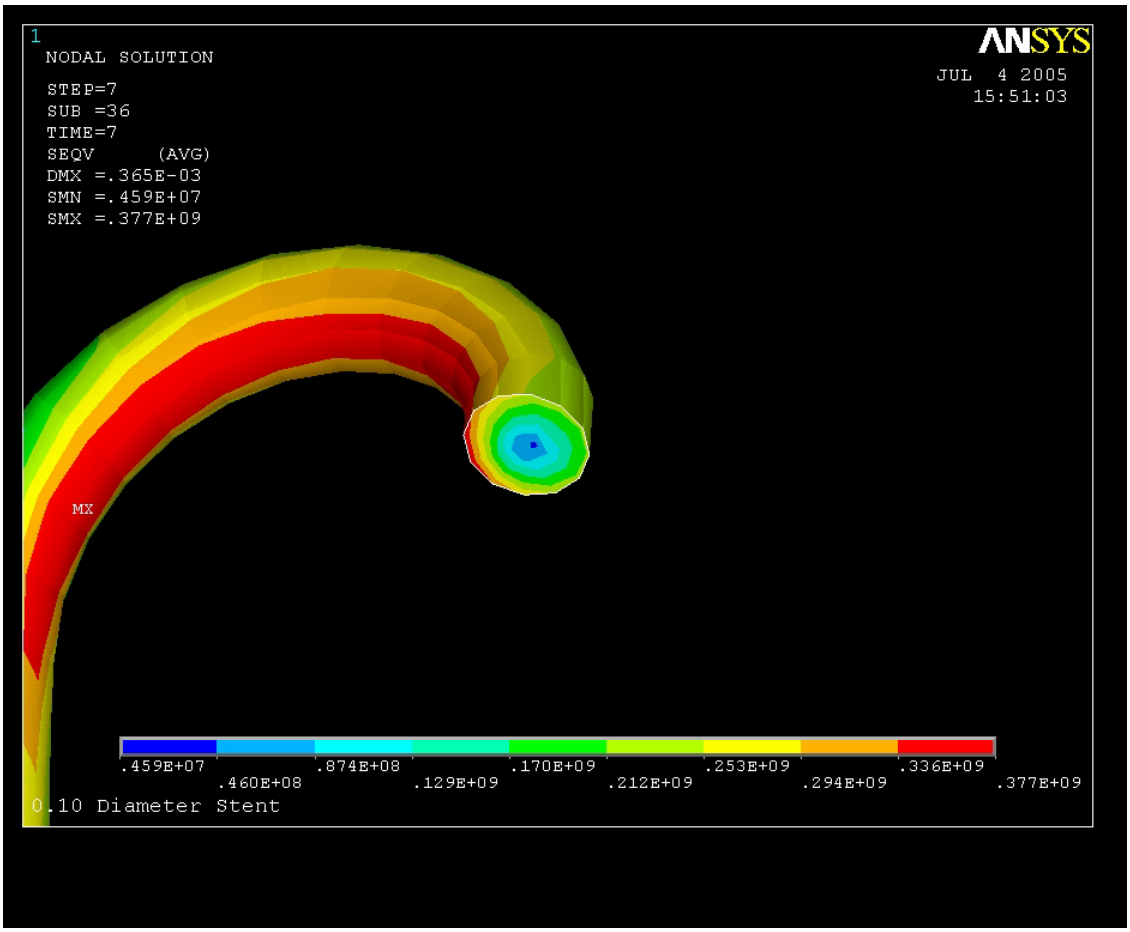

Fig. B.26 Von Mises Stress Contour Plot at 7(atm) of Cross Section PLLA Fiber

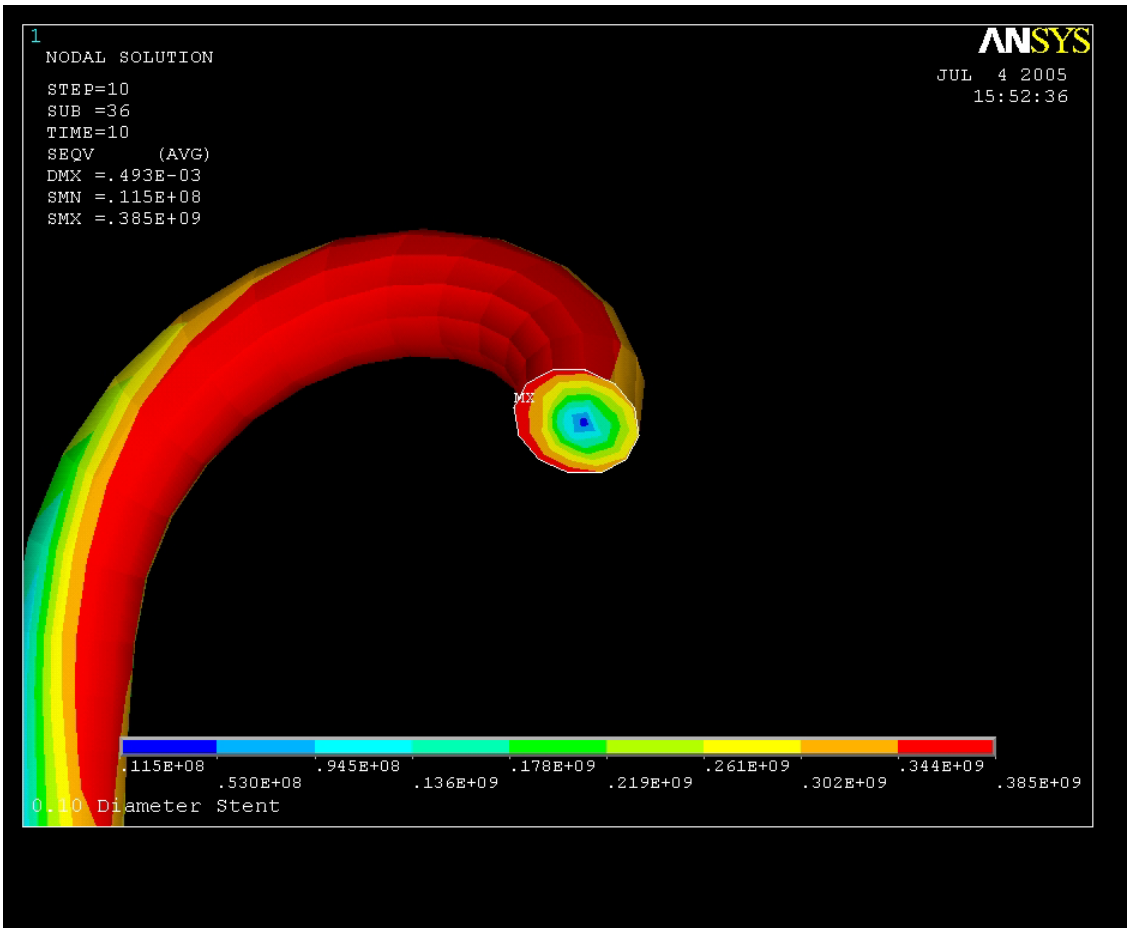

Fig. B.27 Von Mises Stress Contour Plot at 10(atm) of Cross Section PLLA Fiber

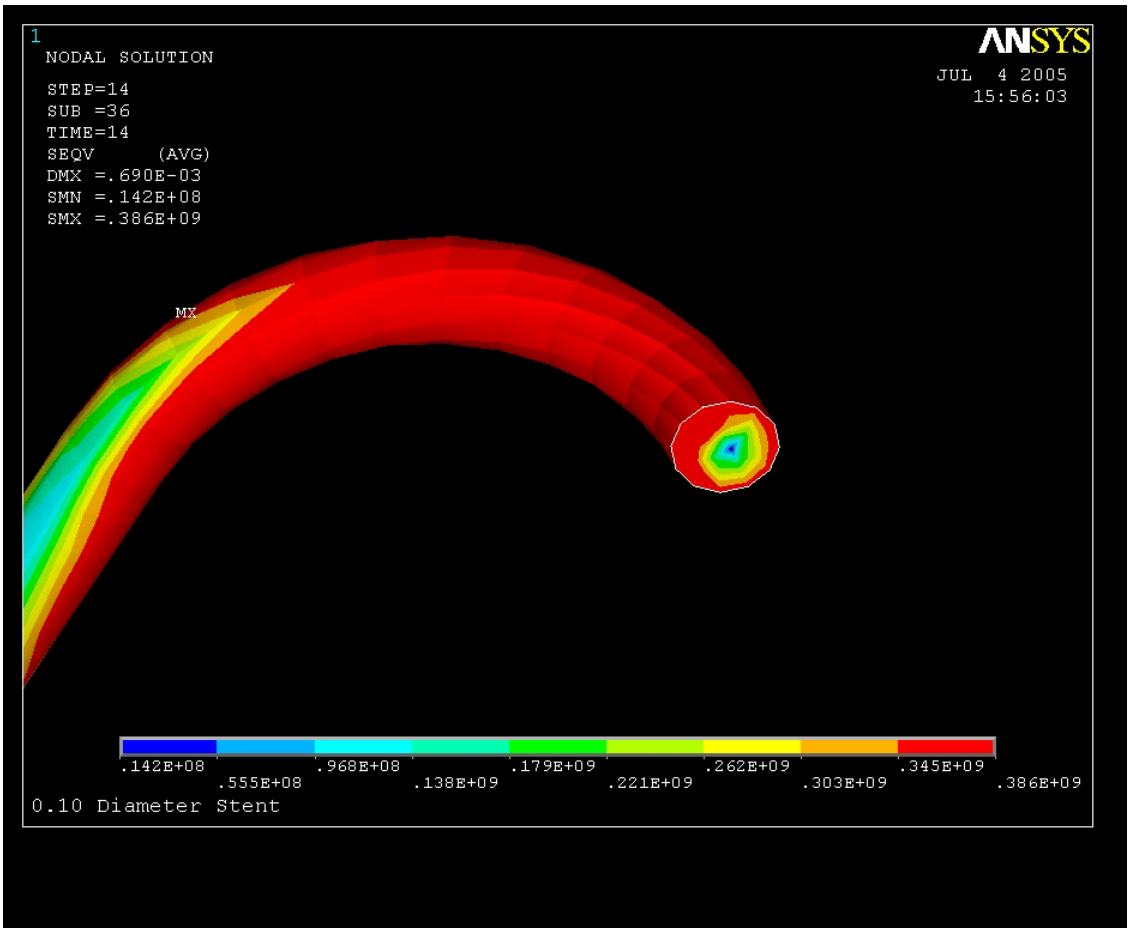

Fig. B.28 Von Mises Stress Contour Plot at 14(atm) of Cross Section PLLA Fiber

REFERENCES

Bathe, K. J. (1996). Finite Element Procedures. New Jersey: Prentice-Hall, Inc.

Bennett, M. R., O'Sullivan, M. (2001). Mechanisms of angioplasty and stent restenosis: implications for design of rational therapy. Pharmacology and Therapeutics, 91, 149-166.

Callister, W.D. Jr. (1994). Material Science and Engineering: An Introduction (3rd ed.). New York: John Wiley & Sons, Inc.

Chua, D. S. N., MacDonald, B. J., Hashmi, M. S. J. (2004). Effects of varying slotted tube (stent) geometry on its expansion behavior using finite element method. Journal of Materials Processing Technology. 155-156, 1764-1771.

Etave, F., Finet, G., Boivin, M., Boyer, J.C., Rioufol, G., Thollet, G. (2001). Mechancial properties of coronary stents determined by using finite element analysis. Journal of Biomechanics, 34, 1065-1075.

Fox, S.I. (2002). Human Physiology (7th ed.). New York: McGraw-Hill Higher Education.

Lally, C., Dolan, F., Prendergast, P. J. (2005). Cardiovascular stent design and vessel stresses: a finite element analysis. Journal of Biomechanics, 38, 1574-1581.

Migliavacca, F., Petrini, L., Montanari, V., Quagliana, I., Auricchio, F., Dubini, G.(2005). A predicative study of the mechanical behavior of coronary stents by computer modeling. Medical Engineering & Physics, 27, 13-18.

Norton, R. L. (1996). Machine Design: An Integrated Approach. New Jersey: Prentice-Hall Inc.

Osterle, S. N., Whitbourn, R., Fitzgerald, P. J., Yeung, A.C., Stertzer, S. H., Dake, M. D., Yock, P. G., Virmani, R. (1998). The stent decade: 1987 to 1997. American Heart Journal, 136, 579-599.

ProAct Technologies Corp. (n.d.) Coronary Heart Disease. Retrieved July 18, 2005, from www.thehealthpages.com/ articles/ar-heart.html.

Ratner, B.D., Hoffman, A.S., Schoen, F. J., Lemons, J. E. (Eds.). (2004). Biomaterials Science. San Diego: Elsevier Inc.

Seymour, R.B.& Carraher, C.E. Jr. (1992). Polymer Chemistry: An Introduction (3rd ed.). New York: Marcel Dekker, Inc.

Sullivan, T. M., Ainsworth, S. D., Langan, E. M., Taylor, S., Snyder, B., Cull, D., Youkey, J., Laberge, M. (2002). Effect of endovascular stent strut geometry on vascular injury, myointimal hyperplasia, and restenosis. Journal of Vascular Surgery, 36, 143-149.

Su, S. (2000). New expandable biodegradable polymeric endovascular stent designs (Doctoral dissertation, University of Texas at Arlington, 2000).

Tuzcu, E. M., Schoenhagen, P. (2003). Acute Coronary Syndromes, Plaque Vulnerability, and Carotid Artery Disease. Journal of the American College of Cardiology, 42, 1033-1036.

Walke, W., Paszenda, Z., Filipiak, J. (2005). Experimental and numerical biomechanical analysis of vascular stent. Journal of Materials Processing Technology, 164-165, 1263-1268.

Wang, W. Q., Liang, D. K., Yang, D. Z., Qi, M. (2004). Analysis of the transient expansion behavior and design optimization of coronary stents by finite element method. Journal of Biomechanics. Retrieved February 20, 2005, from http://www.sciencedirect.com/

Warkentin, D. L. (n.d.). Coronary Artery Stents. Retrieved May 15, 2005, from http://www.medformation.com/ac/ crsca.nsf/ca/ca_carstent_car.htm.

BIOGRAPHICAL INFORMATION

Tre Welch completed his Bachelor of Science Degree in Mechanical Engineering and Bachelor of Arts in Chemistry at the University of Texas at Arlington on December of 1998 with high interest in electronics and motor controls. His career as an engineer began at Harris Corporation as a Mechanical Engineer. For two years he worked on proprietary process and product development for defense contracts. He excelled at characterizing materials and electronics packaging design. His next job was working as a Mechanical Engineer for Chorum Technologies. There he utilized his design skills to develop new optical component equipment for the telecommunications industry and designed material testing equipment. After working at Chorum for 1.5 years, he entered into the graduate program at the University of Texas at Arlington pursing his Masters of Science in Biomedical Engineering wanting to work on stent analysis. His future goals are to stay at the University of Texas at Arlington to complete a Doctorate of Philosophy in Biomedical Engineering expanding the topic of stent development and analysis.